INVESTIGATION OF PERFORMANCE ENHANCING DEVICES FOR THE RAIN ZONES OF WET-COOLING TOWERS

by

Riaan Terblanche

Thesis presented in fulfilment of the requirements for the degree M.Sc. Engineering at the University of Stellenbosch

Supervisor: H.C.R. Reuter

Department of Mechanical Engineering
University of Stellenbosch
Stellenbosch, South Africa

March 2008

DECLARATION

I, the undersigned, hereby declare that the work contained in this thesis is my own original work and that I have not previously in its entirety or in part submitted it at any university for a degree.

Signature:…….

Date:…….

SUMMARY

The performance of a natural draught wet-cooling tower can be improved by reducing the average drop size in the rain zone. In this thesis, the effect of installing different horizontal grids below the fill on drop size in the rain zone is investigated experimentally and theoretically. A specially designed horizontal grid consisting of evenly spaced slats and a grid made from expanded metal sheeting are tested. Drop size distribution measurements are taken below different cooling tower fills to determine the respective Sauter mean drop sizes and also below different configurations of splash grids to determine the reduction in drop size. Drop break-up through a grid of horizontally placed slats is modelled and compared to measured data to determine the optimum configuration in terms of spacing between the grid and fill, slat width and slat spacing. A cross flow rain zone is modelled under different air and water flow combinations with CFD for two distributions that represent the rain with and without splash grids and the results are compared. The Merkel transfer characteristic for all the flow conditions using both distributions are determined using a Lagrangian, Merkel, Poppe and e-NTU method in order to quantify the increase in rain zone Merkel number. Pressure drop over the cross flow rain zone is also determined and compared for the two distributions under considerations.

OPSOMMING

Die verkoelingsvermoë van ‘n reënsone van ‘n natuurlike trek nat koeltoring kan verbeter word deur die verkleining van die gemiddelde druppelgrootte. In hierdie tesis word die effek wat horisontale roosters op die druppelgrootte het, wanneer dit onder die pakking geïnstalleer is, eksperimenteel en teoreties ondersoek. ‘n Spesiaal ontwerpte rooster bestaande uit horisontaal gepakte latte en ‘n gerolde metaal rooster word onderskeidelik vir hierdie doel gebruik. Druppelgrootte metings word geneem onder verskillende koeltoring pakkingsmateriaal om die Sauter gemiddelde diameter te bepaal, asook onder die verskillende rooster opstellings om die verkleinde druppelgrootte te bepaal wat die rooster veroorsaak. Druppelopbreking deur ‘n laag horisontaal gepakte latte word gemodelleer en vergelyk met gemete data om sodoende die beste kombinasie tussen die afstand onder die pakkingsmateriaal, latwydte en latspasiëring te bepaal. ‘n Kruisvloei reënsone word gemodelleer met CFD onder verkillende lug- en watervoeikombinasies vir twee druppelverdelings wat die reënsone met en sonder roosters verteenwoordig. Die Merkel oordragskoëffisiënt vir die twee verdelings word bereken en vergelyk deur van ‘n Lagrange- , Merkel- , Poppe- en e-NTU metode gebruik te maak om sodoende die verbetering in reënsone Merkelgetal te kwantifiseer. Drukvalle oor die reënsone word ook bereken en vergelyk vir die twee verdelings wat beskou is.

Dedicated to the God who makes me strong and to my parents who still pray for me

ACKNOWLEDGEMENTS

I would like to thank the following people for their help and support:

Thank you, Mr. Reuter, for giving me a chance to prove myself. Thank you for pushing me to always do more and better and also for your patience and an open door.

Thank you to all the personnel at SMD, especially Mr. Cobus Zietsman for his advice and also Calvin Hammerse for all the work he did for me.

Thank you to my parents who supported me and encouraged me through the whole of the project. Thank you for inspiring me to always aim high and for showing me how to make the best of any situation.

Thank you to Heinrich Störm for his help with setting up my experimental apparatus. It is much appreciated.

Thank you to my girlfriend, Anneke, for her support and keeping up with me when I sometimes got irritated. I appreciate and love you very much.

TABLE OF CONTENTS

DECLARATION i

SUMMARY ii

OPSOMMING iii

ACKNOWLEDGEMENTS v

TABLE OF CONTENTS vi

NOMENCLATURE xi

LIST OF FIGURES xv

LIST OF TABLES xix

1. INTRODUCTION 1

1.1 General background 1

1.2 Literature study 3

1.3 Objectives 5

1.4 Motivation 6

1.5 Scope of work 6

1.6 Thesis summary 7

2. MEASUREMENT OF DROP SIZE DISTRIBUTION 9

2.1 Introduction 9

2.2 Description of experimental equipment 10

2.2.1 Indoor counter flow cooling tower test facility 10

2.2.2 Grid consisting of evenly spaced slats 12

2.2.3 Expanded metal grid 13

2.2.4 Water drop size measurement equipment 13

2.3 Measurement techniques *15*
2.3.1 Drop size measurement 15
2.3.2 Water flow rate measurement 19
2.3.3 Air flow rate measurement 20
2.4 Test procedure *20*
2.4.1 Taking digital images 20
2.4.2 Image processing and data extraction from images 21
2.5 Results *21*
2.5.1 Characteristic drop distribution under different fill types 22
2.5.2 Drop break-up characteristics of a specifically designed slat grid 33
2.5.3 Drop break-up characteristics of expanded metal grid 36
2.6 Discussion of results *36*
2.7 Conclusion and recommendations *37*
3. MODELLING OF MOTION AND COOLING OF SINGLE DROPS FALLING THROUGH AIR **39**
3.1 Introduction *39*
3.2 Background *39*
3.2 Governing differential equations and numerical methods *40*
3.2.1 Governing equations for drop velocity 40
3.2.2 Governing equations for temperature change 44
3.3 Results *48*
4. MODELLING OF DROP SIZE REDUCTION BY MEANS OF SLATS **51**
4.1 Introduction *51*
4.2 Theory *51*
4.2.1 Splashing 51
4.2.2 Cutting 54
4.2.3 Dripping 57
4.3 Solution procedure *61*
4.3.1 Initial drop distribution 61

4.3.2 Drop drag models 61
4.3.3 Drop-drop collisions 62
4.3.4 Film thickness on the slats 62
4.3.5 Drop break-up 62
4.3.6 Splash model 63
4.3.7 Cutting model 63
4.3.8 Dripping model 63
4.3.9 Upward flowing drops 63
4.3.10 Modelling drops in parcels 63

4.4 Results *64*

4.5 Discussion and recommendations *68*

5. MODELLING OF CROSS FLOW RAIN ZONE PERFORMANCE **70**

5.1 Introduction *70*

5.2 Theoretical methods of analysis *72*
5.2.1 Poppe 72
5.2.2 Merkel 74
5.2.3 e-NTU 74
5.2.4 Pressure drop 77

5.3 CFD *77*

5.4 Results *79*

5.5 Discussion and recommendations *85*

6. CONCLUSION **88**

6.1 Conclusions *88*

A. THERMOPHYSICAL PROPERTIES **94**

B. DEVELOPMENT OF DROP SIZE MEASUREMENT EQUIPMENT AND SOFTWARE **98**

B.1 Introduction *98*

B.2 Equipment design criteria *98*
B.2.1 Camera housing 98
B.2.2 Drop images 99
B.2.3 Software program 99
B.3 Description of photographic equipment *99*
B.3.1 Camera housing 99
B.3.2 Camera 100
B.3.3 Software program 101

C. DROP SIZE REDUCTION GRID DESIGN **103**
C.1 Design criteria *103*
C.2 Description of the reduction grid design *103*

D. EXPERIMENTAL APPARATUS FOR DRIPPING EXPERIMENTS **105**

E. CALIBRATION DATA **106**
E.1 Water flow pressure transducer calibration *106*
E.2 Water flow venturi calibration *106*
E.3 Air flow venturi calibration *109*
E.4 Calibration of drop size measurement system *110*

F. USER MANUAL AND INSTRUCTIONS **113**
F.1 Opening screen of the software program *113*
F.2 Load an image into the program *114*
F.3 Setting the image processing parameters *114*
F.4 Run the program *116*
F.5 View the results *117*
F.6 Export data to Excel *118*

G. MEASURED DATA **119**

H. SINGLE DROP SAMPLE CALCULATION **125**

I. SAMPLE CALCULATION FOR PREDICTING THE DROP DISTRIBUTION BELOW A GRID OF HORIZONTAL SLATS **129**

J. SAMPLE CALCULATION FOR *e*-NTU METHOD IN DETERMINING THE MERKEL NUMBER FOR A CROSS FLOW RAIN ZONE **134**

K. SAMPLE CALCULATION FOR THE PREDICTION OF CROSS FLOW PERFORMANCE **137**

L. CFD SOLVER MODELS AND INFORMATION **140**

NOMENCLATURE

List of symbols

A	Area, m^2
C	Non-dimensional drop size,- or capacity rate,-
C_D	Drag coefficient, -
c	Species or constituent concentration
c_F	Friction factor
c_p	Specific heat at constant pressure, J/kgK
c_v	Specific heat at constant volume, J/kgK
D	Diffusion coefficient, m^2/s
d	Diameter, mm
$\bar{d}$	Mean diameter, mm
E	Drop deformation ratio, -
e	Effectiveness, -
F	Force, N
f	Fraction, -
G	Mass velocity, kg/m^2s
g	Gravitational acceleration, m/s^2
g_{YS}	Correction factor, -
H	Height, m
h	Heat transfer coefficient, W/m^2K
h_D	Mass transfer coefficient, m/s
h_d	Mass transfer coefficient, kg/m^2s
i	Enthalpy, J/kg
K	Pressure loss coefficient
KE	Kinetic energy, J
k	Thermal conductivity, W/mK
M	Mass, kg
m	Mass flow rate, kg/s
NTU	Number of transfer units
n	Number of drops
n_{RR}	Spread diameter, mm

p	Pressure, Pa
Q	Heat transfer rate, W
R	Gas constant, J/kgK, Cumulative mass fraction
S	Shape factor, -, or slat spacing, mm
T	Temperature, K
t	Time, s
U	Total internal energy, J
V	Volt,V, or Volume, m^3
$\dot{V}$	Volumetric flow rate, l/s
v	Velocity, m/s
w	Humidity ratio, kg/kg dry air
W	Slat width, mm
z	Height, m

List of Greek symbols

Δ	Differential
θ	Angle, $^\circ$
ψ	Angle, $^\circ$
ϕ	Angle, $^\circ$
λ	Correction factor, J/kg
μ	Dynamic viscosity, kg/ms
ρ	Density, kg/m^3
σ	Surface tension, N/m
δ	Water film thickness on slat, mm

List of subscripts

a	Air
B	Buoyancy
b	Break
c	Convection or cut
D	Drag,
d	Drop, dripping, diameter
e	Escape or evaporate

f	Fluid
fg	Fill-grid
fr	Frontal
g	Gas
i	Inlet
m	Mean
n	New
o	Outlet, original
p	Primary or primary particle
pr	Projected
R	Resultant
RR	Rosin Rammler
rz	Rain zone
s	Saturation , surface or splash
T	Terminal velocity
t	Throat
v	Vapour or venturi
w	Water
wb	Wet bulb

Dimensionless groups

Eo	Eotvos number,	$\frac{gd^2(\rho_p - \rho_f)}{\sigma}$
Le_f	Lewis factor,	$\frac{h_c}{h_d c_p}$
Nu	Nusselt number,	$\frac{h_c d}{k} = f(Re, Pr)$
Pr	Prandtl number,	$\frac{c_p \mu}{k}$
Re	Reynolds number,	$\frac{\rho v d}{\mu}$
Sc	Schmidt number,	$\frac{\mu}{\rho D}$

Sh	Sherwood number,	$\frac{h_D d}{D} = f(Re, Sc)$
We	Weber number,	$\frac{\rho v^2 d}{\sigma}$

Abbreviations

CFD	Computational fluid dynamics
STP	Standard temperature and pressure, 20°C and 101.325 Pa

LIST OF FIGURES

Figure 1.1 : Counter flow natural draught wet cooling tower 2

Figure 2.1 : Schematic representation of the counter flow cooling tower test facility 11

Figure 2.2: Photograph of the counter flow cooling tower test facility 12

Figure 2.3 : Layout of the slat grid 13

Figure 2.4 : Photograph of the slat grid 13

Figure 2.5 : Expanded metal grid dimensions 13

Figure 2.6 : Expanded metal grid photograph 13

Figure 2.7 : Setup of drop measurement equipment in a rain zone 14

Figure 2.8 : Photograph of drop size measurement camera housing 14

Figure 2.9 : Original image 17

Figure 2.10 : Processed image showing blobs 17

Figure 2.11 : User interface screen for the image processing software program 18

Figure 2.12 : Film fill 22

Figure 2.13 : Cumulative mass distribution directly under film packing, G_a = 1.22 kg/m^{2}s 22

Figure 2.14 : Cumulative mass distribution directly under film packing, G_a = 1.71 kg/m^{2}s 23

Figure 2.15 : Cumulative mass distribution directly under film packing, G_a = 2.28 kg/m^{2}s 23

Figure 2.16 : Cumulative mass distribution directly under film packing, G_a = 2.85 kg/m^{2}s 24

Figure 2.17 : Sauter mean diameters directly under film packing 24

Figure 2.18 : Trickle fill 25

Figure 2.19 : Cumulative mass distribution directly under trickle fill, G_a = 1.22 kg/m^{2}s 26

Figure 2.20 : Cumulative mass distribution directly under trickle fill, G_a = 1.71 kg/m^{2}s 26

Figure 2.21 : Cumulative mass distribution directly under trickle fill, G_a = 2.28 kg/m^{2}s 27

Figure 2.22 : Cumulative mass distribution directly under trickle fill, G_a = 2.85 kg/m^{2}s 27

Figure 2.23 : Sauter mean diameter directly under trickle fill 28

Figure 2.24 : Fill installation 29

Figure 2.25 : Fibre cement fill 29

Figure 2.26 : Cumulative mass distribution directly under fibre cement fill, G_a = 1.22 kg/m^{2}s 30

Figure 2.27 : Cumulative mass distributions directly under fibre cement fill, G_a = 1.71 kg/m^{2}s 30

Figure 2.28 : Cumulative mass distribution directly under fibre cement fill, G_a = 2.28 kg/m^{2}s 31

Figure 2.29 : Cumulative mass distribution directly under fibre cement fill, G_a = 2.85 kg/m^{2}s 31
Figure 2.30 : Sauter mean diameter immediately below the fibre cement fill 32
Figure 2.31 : Sauter mean diameter directly below different slat grid arrangements, G_w = 2.84 kg/m^{2}s 33
Figure 2.32 : Test setup for grid spacing and air tests 34
Figure 2.33 : Sauter mean diameters immediately below equivalent slat grid setups, G_w = 2.84 kg/m^{2}s 35
Figure 2.34 : Sauter means measured immediately below expanded metal grids, G_w = 2.84 kg/m^{2}s 36
Figure 2.35 : Expanded metal dripping regions 38
Figure 3.1: Free-body diagram of a falling drop in an air stream 40
Figure 3.2 : Deformed drop geometry 43
Figure 3.3 : Control volume for a cooling drop 44
Figure 3.4 : Comparison of velocity between drop deformation and non-deformation model 48
Figure 3.5 : Cooling of drops 48
Figure 3.6 : Transfer characteristics for different flow configurations 49
Figure 4.1 : Cutting of a drop on a slat 54
Figure 4.2 : Average cutting fraction for different slat widths 55
Figure 4.3 : Variables of equation 4.13 and 4.14 56
Figure 4.4 : Drop impacting on a slat 57
Figure 4.5 : Cutting mass distribution (d_i = 5 mm, W = 3 mm) 57
Figure 4.6 : Schematic representation of the shape factor 58
Figure 4.7 : Predicted cumulative mass distributions below slat grid for G_w = 2.84 kg/m^{2}s, 64
Figure 4.8 : Predicted Sauter mean diameters below slat grid for G_w = 2.84kg/m^{2}s, H_{fg} = 0.6 m 64
Figure 4.9 : Measured and predicted Sauter means below one layer of slat grid, G_w = 2.84 kg/m^{2}s, no air 65
Figure 4.10 : Measured and predicted mass distribution, G_w = 2.84 kg/m^{2}s, no air, H_{fg} = 0.6 m 66
Figure 4.11 : Effect of distance below the fill on the Sauter mean diameter, S = 10 mm, W = 3mm 66
Figure 4.12 : Effect of slat width on the Sauter mean diameter, H_{fg} = 0.6 m, S = 10 mm 67

Figure 4.13 : Effect of spacing between the slats on Sauter mean diameter, W = 3 mm, H_{fg} = 0.6 m 67
Figure 4.14 : Comparison between the bottom profiles of slats, G_w = 2.84 kg/m^{2}s, No air 67
Figure 4.15 : Predicted Sauter mean diameters below one layer of slat grid, G_w = 2.84 kg/m^{2}s 68
Figure 5.1 : Control volume for cross flow rain zone section 72
Figure 5.2 : Solution grid for cross flow model 73
Figure 5.3 : Water temp. (dist. A - measured) 78
Figure 5.4 : Water temperature (dist. A-mono) 78
Figure 5.5 : Air humidity (dist. A – measured) 78
Figure 5.6 : Air humidity (dist. A – mono) 78
Figure 5.7 : Air temp. (dist. A – measured) 78
Figure 5.8 : Air temperature (dist. A – mono) 78
Figure 5.9 : Water outlet temperatures as predicted with CFD 79
Figure 5.10 : Merkel numbers for distribution A and B (Lagrangian method) 80
Figure 5.11 : Merkel numbers for distributions A and B (Merkel method) 81
Figure 5.12 : Merkel numbers for distributions A and B (e-NTU method) 82
Figure 5.13 : Merkel numbers for distributions A and B (Poppe method) 83
Figure 5.14 : Pressure drop (Dist. A – mono) 83
Figure 5.15 : Pressure drop (Dist. B – mono) 83
Figure 5.16 : Pressure drop (Distribution A) 84
Figure 5.17 : Pressure drop (Distribution B) 84
Figure 5.18 : Pressure drop (Distribution A) 84
Figure 5.19 : Pressure drop (Distribution B) 84
Figure 5.20 : Loss coefficients (Dist. A) 85
Figure 5.21 : Loss coefficients (Dist. B) 85
Figure 5.22: Rain zone Merkel ratio between monodisperse and polydisperse distributions A and B (G_w = 2.84 kg/m^{2}s) 85
Figure 5.23 : Scaled increase in total Merkel number between distributions A and B in the rain zone, G_w = 2.84kg/m^{2}s, G_a 2.28 kg/m^{2}s 86
Figure 5.24 : Rain zone pressure drop ratio between distributions A and B (G_w = 2.84 kg/m^{2}s) 86

Figure 5.25 : Scaled increase in total tower pressure drop between distributions A and B, G_w = 2.84kg/m^{2}s, G_a = 2.28 kg/m^{2}s 87

Figure B.1 : Schematic of the layout of the camera housing 100

Figure B.2 : Image processing algorithm 102

Figure C.1 : Loss coefficients for different slat widths with S = 10 mm 104

Figure D.1 : Apparatus for dripping experiments on slats 105

Figure E.1 : Calibration curve for FOXBORO pressure transducer 106

Figure E.2 : Venturi calibration curve 108

Figure E.3 : Errors in flow rate prediction relative to measured flow rate 109

Figure E.4 : Mass flow through Air Flow Venturi for an air density of 1.23 kg/m^3 110

Figure E.5 : Setup for the calibration of the Nikon D70S camera 111

Figure E.6 : Cumulative mass distribution results for different calibration values, G_w = 2.84 kg/m^{2}s 112

Figure F.1 : Opening screen 113

Figure F.2 : Load an image into the program 114

Figure F.3 : Setting the filter parameter values 116

Figure F.4 : Run the program 117

Figure F.5 : Visualization of results 117

Figure F.6 : Export to Excel 118

Figure I.1 : Splash distribution for a *5 mm* incoming drop 131

Figure I.2 : Cutting distribution for *5 mm* incoming drop 132

LIST OF TABLES

Table 2.1 : Test cases for fill tests 21
Table 2.2 : Constants for Rosin Rammler equation with Sauter mean diameters 25
Table 2.3 : Constants for Rosin Rammler equation with Sauter mean diameters 28
Table 2.4 : Constants for Rosin Rammler equation with Sauter mean diameters 32
Table 2.5 : Sauter means for 0.8m grid spacing and air tests, G_w = 2.84 kg/m^{2}s 35
Table 4.1 : Constants for Equation (4.2) 52
Table 4.2 : PVC slat profiles (3 mm wide) for Γ = 0.078 kg/ms with primary drop sizes 59
Table 5.1 : Input drop distributions for CFD analysis 70
Table G.1 : Cumulative mass distributions right below film fill. 119
Table G.2 : Cumulative mass distributions right below trickle fill. 119
Table G.3 : Cumulative mass distributions right below fibre cement fill 121
Table G.4 : Cumulative mass distribution immediately below designed slat grid 122
Table G.5 : Cumulative mass distribution immediately below expanded metal grid 123
Table G.6 : Cumulative mass distribution immediately below trickle grid with no air 123
Table G.7 : Cumulative mass distribution for test facility sprayers, G_w = 2.84 kg/m^{2}s, No air 124
Table G.8 : Cumulative mass distribution for 0.8m grid spacing test with and without air 124
Table H.1 : Initial conditions for single drop sample calculation 125
Table I.1 : Input values to drop size reduction model 129
Table I.2 : Splash distribution for *5 mm* incoming drop 131
Table I.3 : Cutting distribution for 5 mm incoming drop 132
Table J.1 : Input variables for *e*-NTU method 134
Table K.1: Input variables to Poppe cross flow model 137

1

INTRODUCTION

1.1 General background

In industrial thermal systems like power plants, petrochemical plants and air-conditioning systems waste heat must be rejected to the environment. This can be done by rejecting heat to the ocean or rivers by means of a water-cooled condenser, known as once through cooling, or to the atmosphere by using cooling towers or dry air-cooled condensers. The type of heat rejection system used is dependent on environmental conditions such as temperature, humidity, the availability and also the cost of cooling water.

Large natural draught and mechanical draught cooling towers are widely used in industries and differ with regard to the way air flow is affected. In mechanical draught towers, fans are used to provide air flow whereas in natural draught towers air flow is caused by buoyancy effects in a high tower. Cooling towers can also be classified according to the way in which heat is rejected to the atmosphere, for example wet- or dry-cooling. In wet-cooling towers, water comes into direct contact with the cooling air, whereas in dry cooling the process fluid is in finned tubes and is therefore separated from the air. A further classification is the direction of the air flow in relation to the direction of the water flow which can be in cross flow or counter flow.

An increased tower performance can be beneficial to the economy as well as to the environment. Life cycle costs are reduced with an improved tower, which means that the same performance, which can be quantified in terms of range or Merkel transfer characteristic at constant inlet water temperature, can be achieved at lower cost; also meaning that less fossil fuel is burnt in the case of power plants.

Natural draught wet-cooling towers are generally installed when direct cooling is not possible, sufficient cooling water is available and it is economical to do so. Figure 1.1 shows a typical counter flow natural draught wet-cooling tower.

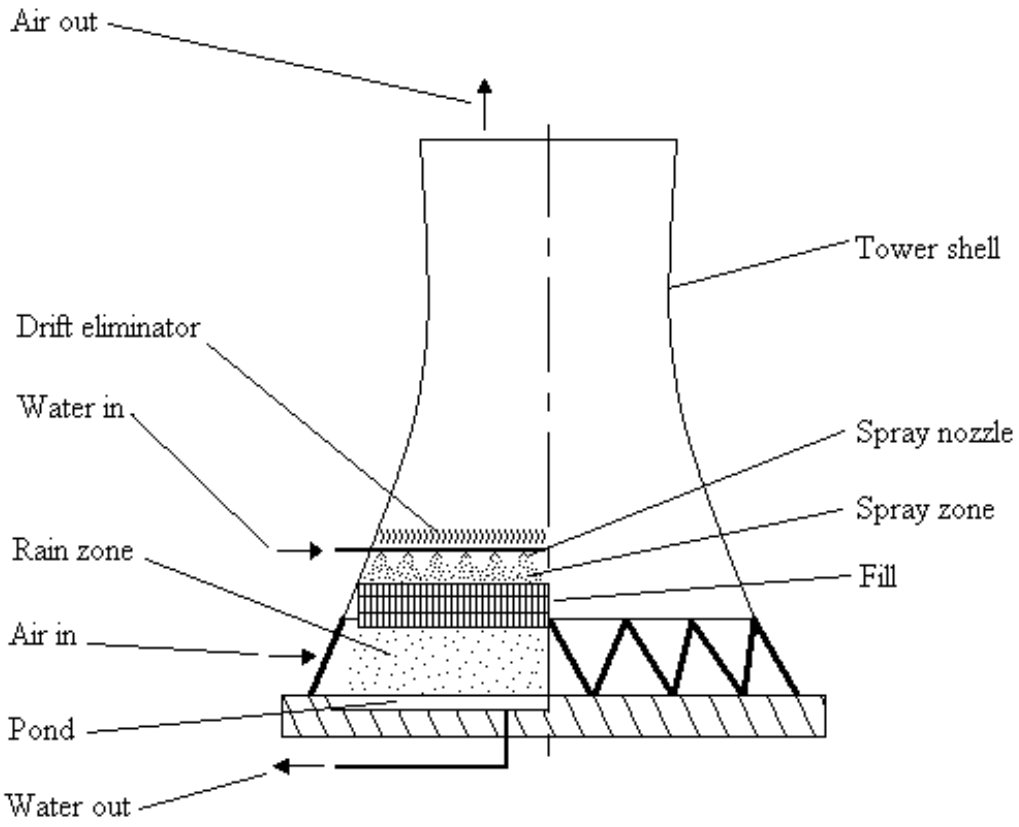

Figure 1.1 : Counter flow natural draught wet cooling tower

Hot cooling water is distributed onto the fill by means of sprayers. In the fill, the surface area between the water and the air is increased for efficient cooling by means of convection heat transfer and mass transfer. Film fill generally comprises plastic, asbestos or fibre cement sheets placed closely together, which allow water to spread in a thin layer over a large area of the fill. Splash fills are designed to break the mass of water falling through the cooling tower into a large number of smaller drops. In trickle fills the water runs down the fill consisting of fine plastic or metal grids. In the rain zone below the fill, the water falls through the air stream as drops between 0.25 and 10 mm in size. According to Kröger [2004KR1], 10 to 20 % of the overall heat and mass transfer of large counter flow wet-cooling towers take place in the rain zone. Drops that are bigger than 10 mm in diameter are seldom encountered, because as they accelerate they become unstable due to the dynamic forces they encounter and break up into smaller drops. After the water has passed through the rain zone, it falls into a pond from which it is pumped back to the plant.

The temperature and humidity of the air in the tower increase as it passes over the water. This reduces the air density above the fill resulting in a natural draught of air through the cooling tower. Cool air enters from the bottom of the cooling tower and the warmer air exits at the top. When drops are very small they can be entrained into the air stream and blown out at the top of the cooling tower. This increases the loss of water to the atmosphere which means that more make-up water is needed. Another bigger problem is that the cooling water contains contaminants, which then leave the tower. Furthermore, drift freezes when it is cold, causing roads to become iced. To combat these drift losses a drift eliminator is inserted above the sprayer section in the cooling tower. Small drops accumulate on the drift eliminator, to form bigger drops which fall back onto the fill under gravity.

This thesis is concerned with reducing the mean drop size in the rain zone of natural draught wet-cooling towers leading to enhanced cooling tower performance.

1.2 Literature study

In order to investigate the performance of the rain zone the drop distribution of the water entering the rain zone must be known, which is generally dependent on the type of fill that is installed in the cooling tower. Kröger [2004KR1] reports that film and trickle fills produce a spectrum of drops with Sauter mean diameters (equation 1.2) ranging between 5 mm and 6 mm and that the Sauter mean diameter of drops below a splash type fill varies between 3 mm and 4 mm. Oosthuizen [1995OO1] measured a Sauter mean drop distribution under a trickle fill of 5 mm to 5.5 mm. The drop distribution below a fill can be presented in terms of a cumulative mass distribution represented by the Rosin Rammler distribution function expressed as

$$R(d) = e^{-\left(\frac{d}{\overline{d}}\right)^{n_{RR}}} \tag{1.1}$$

where

R(d) = Cumulative mass fraction

d = Drop diameter

$\overline{d}$ = Mean drop diameter

n_{RR} = Spread parameter

The Sauter [1981AL1] mean drop diameter is defined as

$$d_{32} = \frac{\sum nd^3}{\sum nd^2} \tag{1.2}$$

As the drops exit the fill, they accelerate under gravity while heat and mass transfer takes place between the water and the air. In the numerical model of Khan et al. [2003KH1] it is illustrated that evaporation is the predominant mode of heat transfer, contributing 62.5 % of the total rate of heat transfer at the bottom of the tower and almost 90 % above the fill. As the Reynolds number of the falling drop increases, the drop shape changes to a non-symmetrical ellipsoidal shape [1994DR1] due to the increased hydrodynamic pressure at the front stagnation point. Beard and Chuang [1987BE1] measured the drop deformation at terminal velocity and the data was correlated by Dreyer [1994DR1]. According to Dreyer [1994DR1] this oblate shape of the drop tends to promote the formation of an attached wake and the onset of wake shedding that causes an increase in the drag coefficient. Other phenomena that occur in a drop as it falls through the air are oscillation and internal circulation [1978CL1]. According to Le Clair et. al [1972LE1] the effect of internal circulation on the drag of a drop is less than 1%. Beard [1977BE1] and Pruppacher and Klett [1978PR1] concluded that the oscillating frequency of the drop as it falls is too high to have a noticeable effect on the drag of the drop. When the drop break-up of a splash fill is modelled, it is important to model the velocity at which the drop impacts the fill accurately. Dreyer [1994DR1] correlated an equation in which the drag coefficient of a sphere is modified to take deformation, internal circulation and oscillation into account.

If the average drop size in the rain zone can be decreased, the effectiveness of the rain zone and therefore the whole cooling tower can be increased. This can be done by placing a splash grid at a certain distance below the fill region. Oosthuizen [1995OO1] placed two layers of splash grid with a constant spacing of 0.1 m between them at various distances below a trickle fill. The splash grid was made from coarse expanded metal sheeting. Oosthuizen achieved the best drop break-up results when the double layer of splash grid was placed 0.67 m below the trickle fill, which produced a Sauter mean diameter of around 4 mm. When the spacing between the fill and the grid was increased further, the Sauter mean diameter for the distribution below the splash grid increased again. Further tests had to be done to see if the

Sauter mean diameter could be decreased even more. From the mathematical modelling of a spray cooling tower, Hollands [1974HO1] concluded that the drops must be uniformly distributed and as small as 1 – 2 mm.

In the PhD thesis of Dreyer [1994DR1], a splash grid for a counter flow wet-cooling tower was modelled. Dreyer mentions three different modes for drop break-up over narrow slats i.e. splashing, cutting and dripping below the slats. The splashing and cutting were thoroughly investigated by Dreyer, while Yung [1980YU1] investigated dripping below horizontal tubes. Dreyer incorporated this theory for determining dripping below slats.

According to Dreyer [1994DR1], drop break-up on narrow slats is dominated by cutting and on wider slats, splashing becomes more dominant. The size of the drops dripping from the slats increases as the slat width increases.

According to Dreyer [1996DR2], a splash pack comprising slats narrower than 10 mm is the most effective if the porosity of the splash pack is 80 %. Effectiveness in this case was defined as the ratio of the overall transfer characteristic to the pressure drop.

Oosthuizen [1995OO1] reported that a decrease in Sauter mean diameter from 5.31 mm to 4.05 mm can lead to an increase in the tower cooling capacity of up to 5 %. This value was obtained with the SPSIM computer program that was developed by Dreyer [1994DR1].

Kloppers [2003KL1] critically evaluated the performance prediction of cross flow and counter flow wet-cooling towers. Equations were derived from first principles and the Merkel, Poppe and e-NTU methods were used to predict the thermal performance of a cooling tower. These methods can also be used to determine the performance increase of a rain zone where the average drop size is reduced by means of grids.

1.3 Objectives

The main aim of the project is to improve the rain zone performance of cooling towers by reducing the mean drop size in this region by inserting splash grids below the fill. In order to determine the optimal grid configuration, the objectives are as follows:

- Measure the drop size distribution below different fills to investigate the effects of air and water mass flow rate on the Sauter mean drop size.
- Design a rain zone performance enhancing device that reduces the Sauter mean drop diameter and measure the effect of spacing below the fill on its drop size reduction capabilities.
- Investigate the expected improvement in rain zone performance using CFD.

1.4 Motivation

In large scale counter flow wet-cooling towers, 10 to 20 % of the overall heat is rejected in the rain zone of the cooling tower [2004KR1]. A considerable improvement in this section of the cooling tower will lead to a considerable improvement in the overall performance of the cooling tower. Performance improvement is quantified in terms of the Merkel transfer characteristic or the range of the cooling tower at constant inlet water temperatures. If for example the Sauter mean diameter in a cross flow rain zone is decreased from 5.19 mm to 2.73 mm, the increase in rain zone Merkel number is in the order of 160 % with a corresponding reduction in water outlet temperature of around 2 – 3 °C (Chapter 5). If it is assumed that this rain zone contributes 10 – 20 % of the total tower Merkel number, this means an increase in total tower Merkel number of 16 – 32 %. The increase in total performance for a large scale counter flow cooling tower can even be slightly more because of the counter flowing component of air relative to the falling water.

Reducing the life cycle costs of cooling towers can be beneficial for business, as well as the environment.

1.5 Scope of work

To meet the objectives, the scope of the work is as follows:

- Develop measurement equipment and software to measure the drop size distribution in a rain zone by means of a photographic procedure.
- Measure the drop distribution directly below different types of fill.
- Design, manufacture and test a special grid comprising evenly spaced PVC slats to reduce the Sauter mean drop diameter in the rain zone.
- Test a grid made from commercially available expanded metal sheeting.

- Develop computer code to predict the drop size distribution obtained by installing a single grid of evenly spaced slats below the fill and compare the results to measured data.
- Develop a computer program to determine heat and mass transfer from a single drop falling under gravity as well as the drop velocity and trajectory.
- Develop numerical models to determine the Merkel performance characteristic of a cross flow rain zone.
- Develop a CFD model to predict the water outlet temperatures of the rain zones comprising of different monodisperse and polydisperse drop sizes. Predicted outlet temperatures from the CFD model also serve as input to the numerical models for determining rain zone Merkel numbers.
- Use the previous 3 models to compare the improvement in rain zone performance characteristic and outlet water temperatures when a drop size reduction grid is installed.

1.6 Thesis summary

The summary of this thesis is represented in this section and the content of each chapter is briefly described.

CHAPTER 1. INTRODUCTION

This chapter gives a brief description of cooling towers. It also presents an overall literature survey, objectives, motivation and the scope of the work in this thesis. A summary of the thesis is also provided at the end of this chapter.

CHAPTER 2. DROP DISTRIBUTION AND MEASUREMENT

In chapter 2 the drop distributions directly below trickle, film and fibre cement fill are measured under different air and water flow conditions in a counter flow test facility. Single and multiple layers of grids are installed below a trickle fill and the drop distributions are measured directly below these grids. Two different types of grids are tested namely an expanded metal grid and a slat grid that is specially designed. The effects of spacing between two layers of slat grid and distance below the fill are also investigated. Lastly the change in drop distribution from just below the slat grid to further below the grid is measured.

CHAPTER 3. MODELLING OF MOTION AND COOLING OF SINGLE DROPS FALLING THROUGH AIR

The governing equations of motion and temperature are derived in this chapter and the results obtained from the derived models are presented. Merkel numbers based on the single drop model for counter flowing, cross flowing and still air are also determined.

CHAPTER 4. MODELLING OF DROP SIZE REDUCTION BY MEANS OF SLATS

The model used to predict the drop distribution below a single layer of slat grid is presented in this chapter. This is done by making use of cutting, splashing and dripping models. A correlation for cutting drop distribution is proposed as well as improved slat profiles that minimize the size of the drops formed by dripping. Experimental results are compared to the results obtained with the model and a correlation is proposed for determining the reduction in Sauter mean diameter through a slat grid.

CHAPTER 5. MODELLING OF CROSS FLOW RAIN ZONE PERFORMANCE

In chapter 5, four different methods for determining the Merkel performance characteristic of a cross flow section are used. The first method is a Lagrangian method (chapter 3) and the equations of motion and cooling are integrated over the fall height of the drops. The Merkel, Poppe and e-NTU methods are also used to determine the performance characteristic of the rain zone, but needs measured data as an input which is obtained from a CFD analysis. The numerical models, together with CFD are used to quantify the increase in rain zone Merkel number due to smaller drops caused by splash grids. The pressure drop for a cross flow section are also investigated and the increase in rain zone pressure drop due to the smaller drops caused by splash grids is quantified.

CHAPTER 6. CONCLUSION

In this chapter the conclusions that can be made from the work done is presented.

2

MEASUREMENT OF DROP SIZE DISTRIBUTION

2.1 Introduction

There is significant potential for enhancing cooling tower performance by reducing the drop size in the rain zone; however limited data is found in literature on this region. It is therefore necessary to generate data by measuring drop distributions under different fills and grids. The main goal is to increase the effectiveness of a rain zone by decreasing the average drop diameter.

Oosthuizen [1995OO1] was able to increase the performance of a rain zone by installing two layers of coarse expanded metal grids below the fill, resulting in a smaller mean drop size. Oosthuizen achieved the best drop size reduction when the two layers of grid were installed 0.67 m below the fill which corresponded to a decrease in the Sauter mean diameter from 5.31 mm to 4.05 mm. Although the spacing between the expanded metal grids and the fill were varied, the effect of varying the spacing between the expanded metal grids was not investigated.

Dreyer [1994DR1] measured the distribution under two types of splash grids of which the slat widths are 9 mm and 25 mm respectively. For the grid with the 9 mm slats, 10 layers were used with a slat pitch of 100 mm. The 25 mm grid was used in a 7 layer setup with a slat pitch of 300 mm. The Sauter mean diameters measured below these setups varied between 3 and 4 mm. It isn't exactly clear how far below the grids these measurements were taken. Tests were conducted at water mass flows of 1.8 kg/m^{2}s and 3 kg/m^{2}s with a constant counter flow air velocity of 1.5 m/s. The water was distributed onto the fill with a distribution system that produces spray with a Sauter mean diameter of 4.84 mm at 3.1 kg/s.

In this section, the experimental apparatus, measurement techniques and test procedures used to measure drop size distribution below different cooling tower fill configurations are described. Drop distribution data can be used to determine rain zone performance and ultimately cooling tower performance analytically or numerically. Drop distributions are

measured below single and multiple layers of two types of splash grids. These splash grids are installed at various distances below the fill to determine which spacing is optimal i.e. creates the smallest drops. The spacing between two layers of slat grid is also increased and the effect on drop size measured.

2.2 Description of experimental equipment

The experimental apparatus for this section is a counter flow induced draught cooling tower test facility as shown in figures 2.1 and 2.2. Different types of cooling tower fill material are installed into the fill region and drop distributions are measured directly below each fill for different water and air flow rates. In order to investigate the drop size reduction capability of different grids, single and multiple layers of two types of grids are installed below a trickle fill and the drop distributions are measured just below the lowest grid. One of the grids, shown in figures 2.3 and 2.4, is specifically designed and consists of horizontal slats, 3 mm wide and 12 mm high, spaced 10 mm apart. The other grid is made from commercially available expanded metal with dimensions shown in figure 2.5 and a photograph of the grid in figure 2.6.

Measurement equipment developed for this project is used to measure drop size distribution.

2.2.1 Indoor counter flow cooling tower test facility

Consider the test facility shown in figures 2.1 and 2.2. Water is pumped from the pond of the test facility, through a venturi where the flow rate is measured by aid of a pressure transducer, to the water distribution section by means of a 15 kW variable speed centrifugal pump. Most of the water is spread evenly onto the fill through which it passes before entering the rain zone where it falls vertically under gravity in the form of drops of various sizes before returning to the basin again. The residual water is collected in the bypass channel from where it drains to the bypass water tank. The cross-sectional surface area of the rain zone is 1.5 m^2 (1.5 m x 1.0 m) and is smaller than the fill section above it, which has a cross sectional area of 2.7 m^2 (1.8 m x 1.5 m).

Ambient air is drawn into the section from the environment through the rounded inlet at the bottom of the test section by means of an axial fan located at the top of the test section. Air passes through the rain zone and the fill, where water vapour and small drops get entrained

into the air stream, before passing through the drift eliminator on which entrained drops accumulate to fall back onto the fill under gravity.

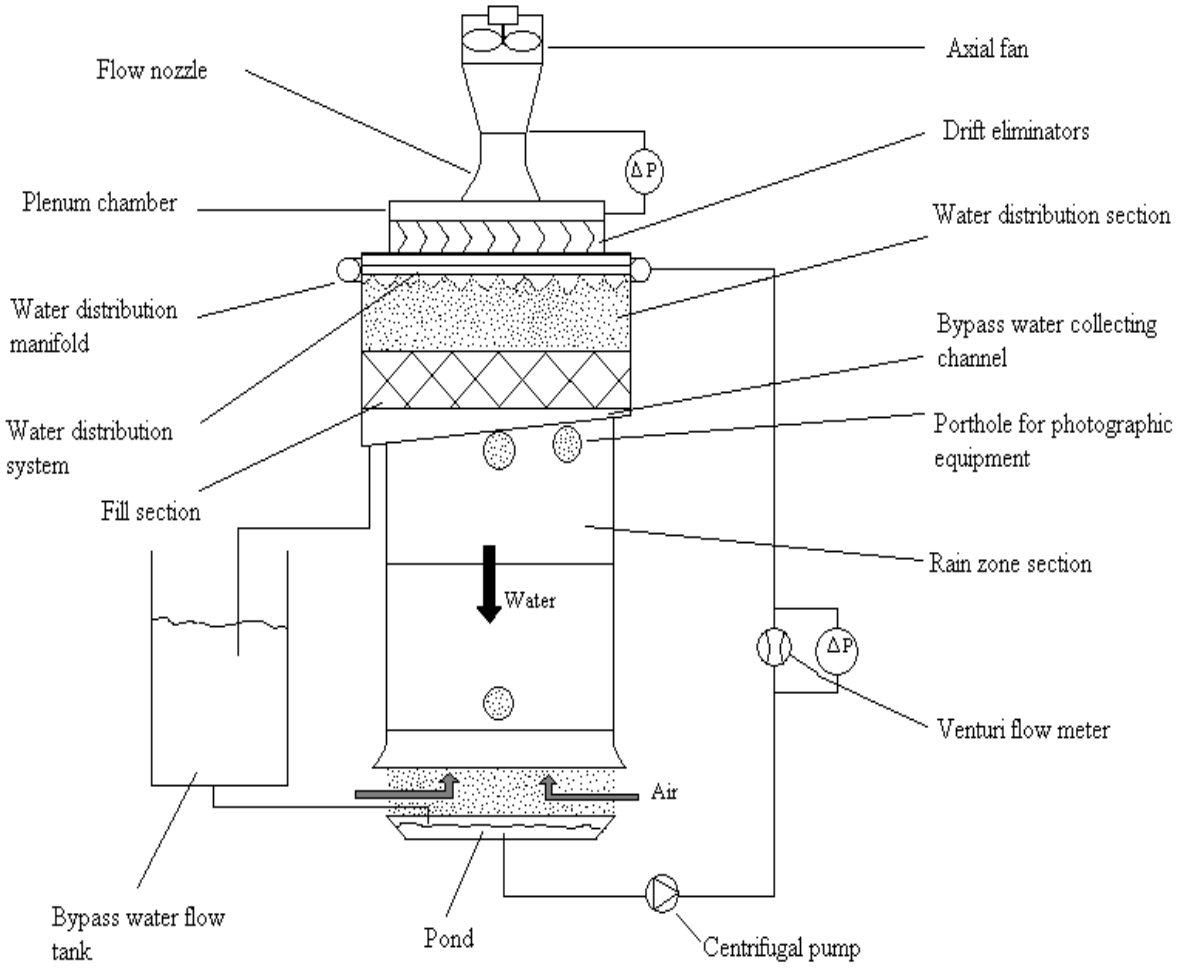

Figure 2.1 : Schematic representation of the counter flow cooling tower test facility

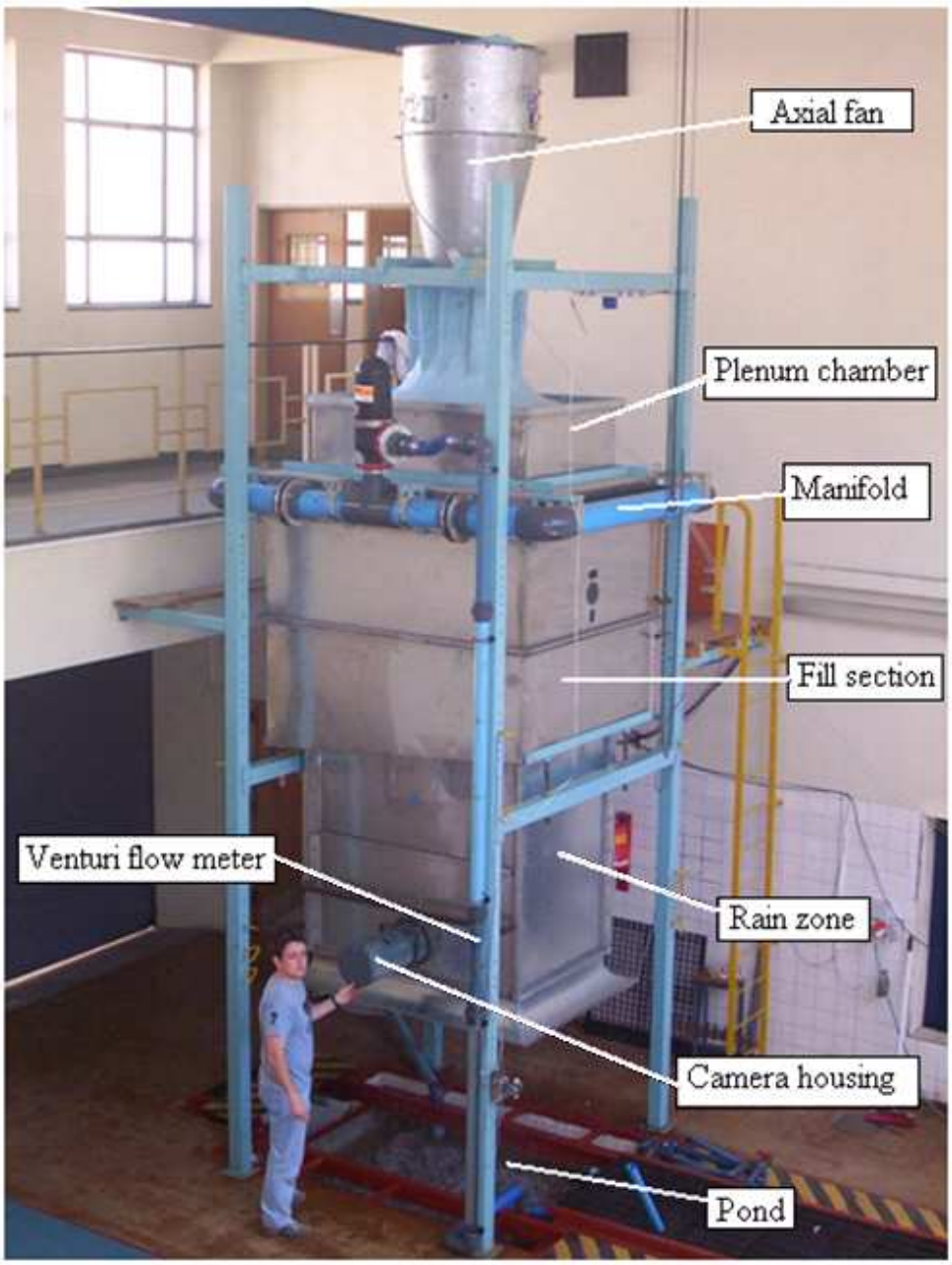

Figure 2.2: Photograph of the counter flow cooling tower test facility

2.2.2 Grid consisting of evenly spaced slats

A grid is designed and manufactured consisting of horizontally placed 3 mm wide by 12 mm high PVC slats that are spaced 10 mm apart. Refer to figures 2.3 and 2.4 for the respective layout and a photograph of the grid. The slats are mounted onto a slotted stainless steel frame with brackets at the ends of the frame so that it is possible to attach more than one layer on top of each other. The design of this grid is described in Appendix C.

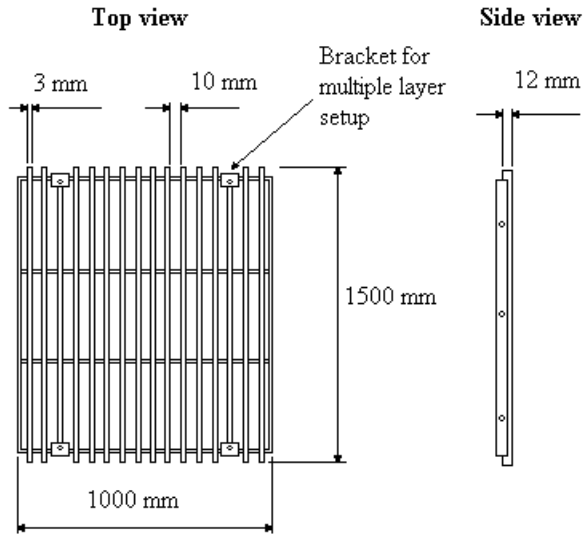

Figure 2.3 : Layout of the slat grid

Figure 2.4 : Photograph of the slat grid

2.2.3 Expanded metal grid

This grid is made from commercially available expanded metal material with dimensions as given in figure 2.5 and a photograph is provided in figure 2.6.

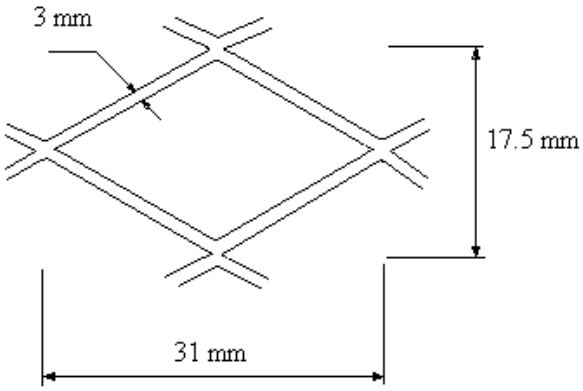

Figure 2.5 : Expanded metal grid dimensions

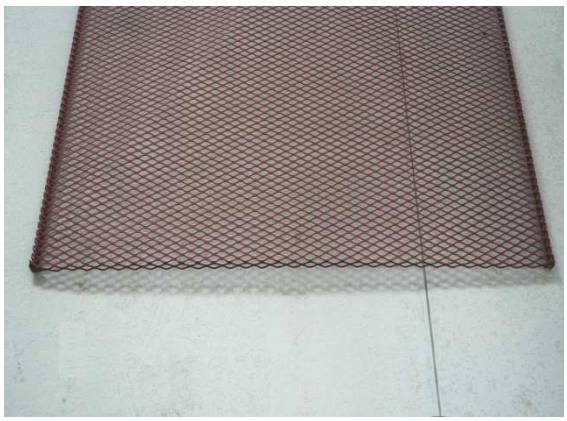

Figure 2.6 : Expanded metal grid photograph

2.2.4 Water drop size measurement equipment

A schematic of the drop measurement equipment assembly is shown in figure 2.7 and a photograph of the camera housing is shown in figure 2.8.

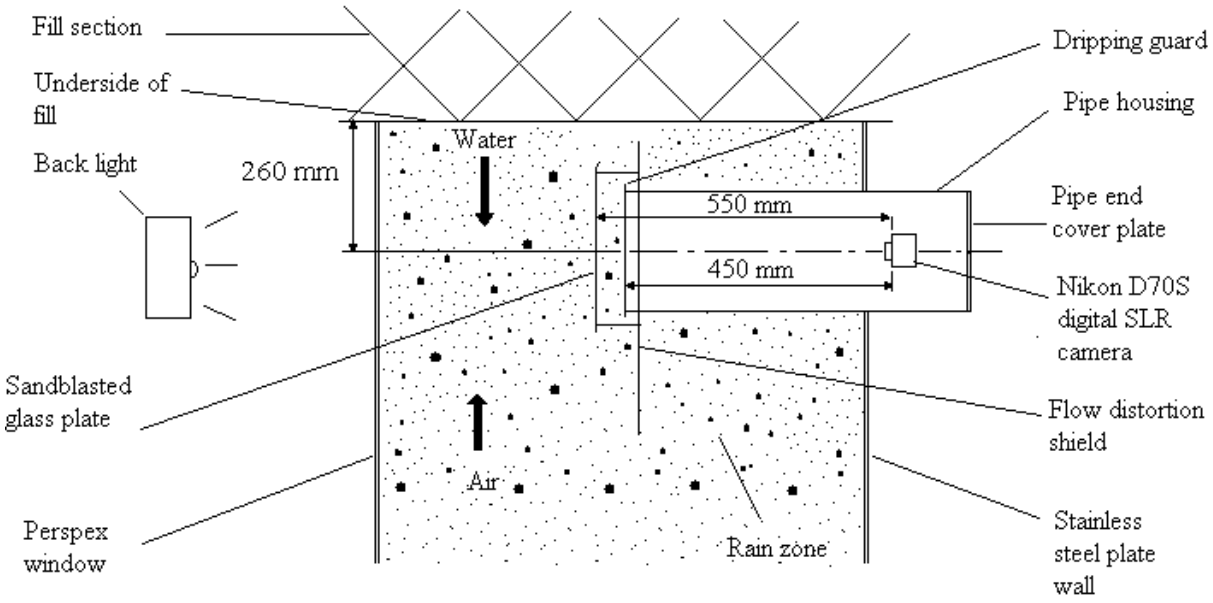

Figure 2.7 : Setup of drop measurement equipment in a rain zone

The water drop measurement equipment is developed and designed in order to do the required drop size measurements in the rain zone. It consists of a pipe housing that can be inserted through the side wall of the rain zone section and is shown in figure 2.8. The different locations where the housing can be inserted can be seen in figure 2.1. This housing is used to hold the camera which is used to take images of the falling drops in the rain zone under different water and air flow conditions.

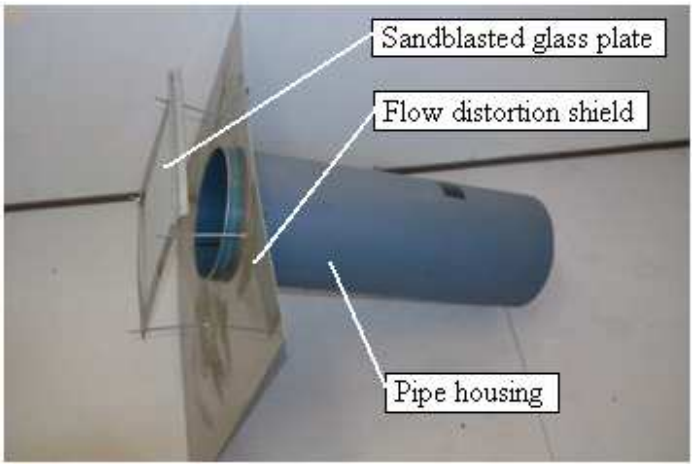

Figure 2.8 : Photograph of drop size measurement camera housing

Strong backlighting is used from the outside of the tower to illuminate the photographic region with the aid of three 1000 W tungsten halogen lights. This is possible because of the Perspex window on the side of the test section.

2.3 Measurement techniques

2.3.1 Drop size measurement

Azzopardi [1979AZ1] reviewed different techniques to measure drop sizes and divided them into the following groups:

1. Photographic methods
2. Impact methods
3. Thermal methods
4. Electrical methods
5. Optical methods
6. Time of residence methods

Between the different drop measurement techniques the photographic technique is the most popular drop measurement technique because of its low cost and relative simplicity.

Oosthuizen [1995OO1] made use of a direct photographic technique to measure drop distributions. The camera was focussed on a plain of specified distance in front of the camera lens. When a photo was taken, the flash light was reflected from a background behind the focus plain to make sure drop edges are visible. The data was extracted from the photograph by applying different image processing operations to the image to identify and extract drop data.

Dreyer [1994DR1] also made use of a photographic method to measure the drop distributions. In this method drops were caught in a Petri dish filled with silicone oil after which the drops in the dish were photographed and measured by making use of image processing software.

Lui [1997LI1] photographed 69 - 198μm diesel drops that were released into a high speed air stream. As the drops passed in front of the camera, lighting was done from behind the drops

into the camera lens with a nano-pulse light. A 35 mm Nikon camera equipped with a long distance microscope was used to capture the images.

Rogers [2002RO1] made use of a laser diffraction method and high speed photography to measure and visualize drop sizes in aerosol sprays.

For the drop distribution measurement of this thesis, a direct photographic procedure is developed to measure drop distributions. Drops are photographed against a sandblasted glass plate in the rain zone and lighting is done from behind the glass plate with three 1000 W tungsten halogen static lights. A software program, specially developed for this purpose, is used to extract the data from the images. The design detail of the photographic equipment is provided in appendix B.

The new photographic procedure can be divided into two parts, which are the physical taking of digital photographic images and the extraction of the data from the images by making use of image processing operations.

2.3.1.1 Photographic imaging

A camera is placed in a housing inserted through the side wall which protrudes into the counter flow cooling tower test facility for taking images of the falling drops.

The image must be of high resolution and therefore the maximum resolution of the camera (6 megapixels) is used. Furthermore, the drops must be well defined and easily recognizable with dark, well defined edges. This is achieved by implementing strong backlighting. The drop edges reflect the light away from the lens and therefore appear dark on the image. The drop edges in the photograph are referred to as high frequency regions which distinguish them from the other regions in the image. High frequency regions are defined as regions where the rate of change of the colour from one pixel to the next is high.

2.3.1.2 Image Processing and data extraction from images

By employing high pass filters, the low frequency regions in the image can be filtered out, leaving the image with easy detectable edges. After the use of a high pass filter, an edge detection filter like the Sobel [2002GO1] filter is used to isolate the drop edges in the image.

A software program that isolates each of the drops in an image is developed and the algorithm is presented in Appendix B. In figure 2.11 the operating screen of the software program can be seen. The program converts all the drops in the image to white blobs by detecting their edges and converting the colour of all the pixels enclosed by the edges to white, and all the others to black as shown in figures 2.9 and 2.10. The user manual for the program is provided in Appendix F.

Each drop identified on the image is numbered and its size is determined by counting the number of white pixels. The drop's projected area can be obtained by multiplying the number of pixels by a calibration value, from which the drop diameter can be determined with the following equation

$$d_d = \left(4A_{pr}/\pi\right)^{0.5} \tag{2.1}$$

The calibration procedure and calibration values are discussed and presented in Appendix E.

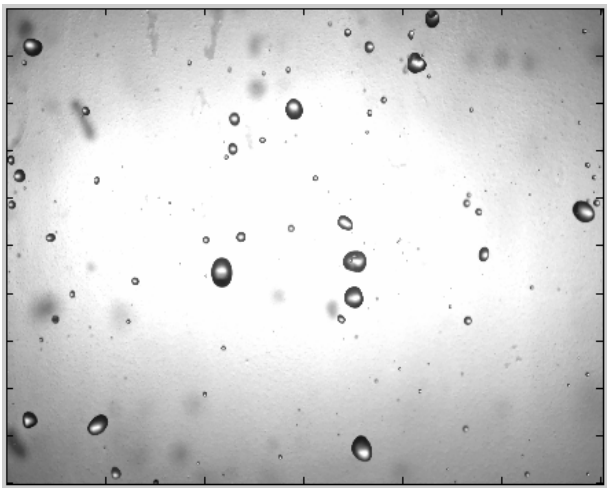

Figure 2.9 : Original image

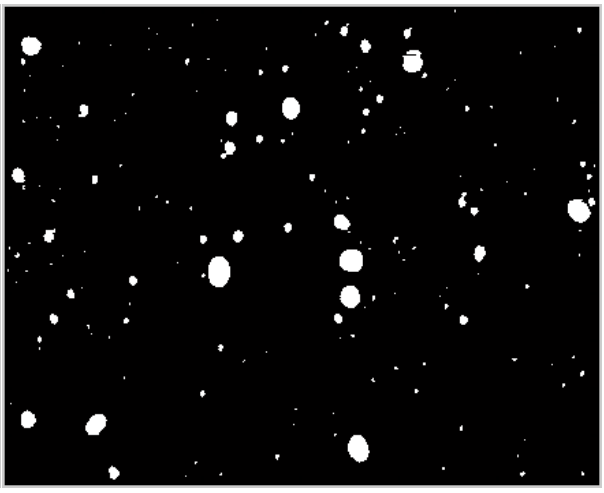

Figure 2.10 : Processed image showing blobs

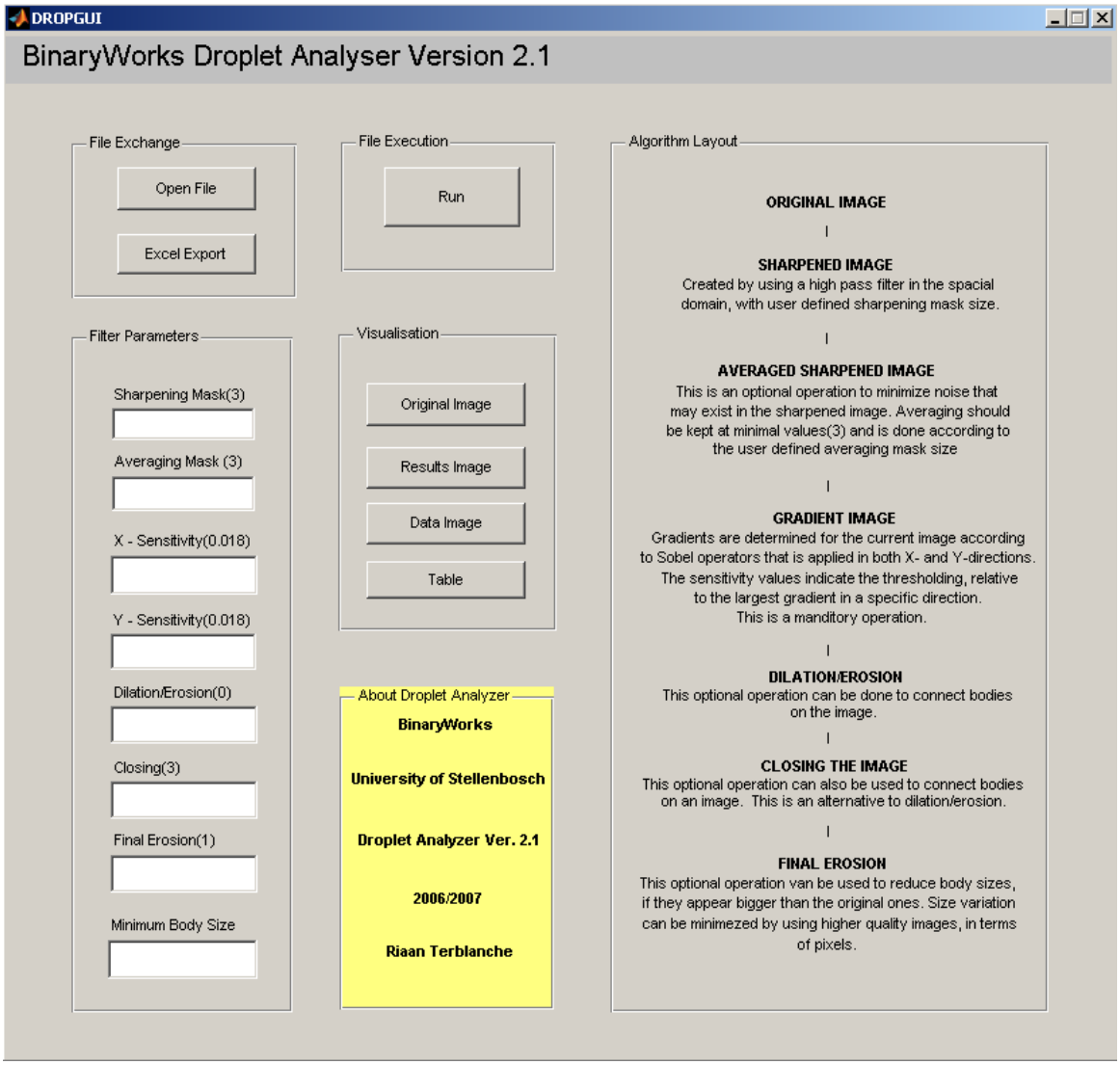

Figure 2.11 : User interface screen for the image processing software program

After extracting the data from the image, the mass distribution is plotted from which a Rosin Rammler [1939RO1] distribution function can be obtained. The Rosin Rammler function is merely an empirical relation based on the assumption that there is an exponential relationship between the drop diameter and the cumulative mass distribution of the drops.

The Rosin Rammler size distribution function is given as

$$R(d) = e^{-\left(\frac{d}{\bar{d}}\right)^{\overline{n_{RR}}}} \tag{2.2}$$

where $R(d)$ = Cumulative mass fraction

d = Drop diameter

$\overline{d}$ = Mean diameter of drops

$\overline{n_{RR}}$ = Average spread parameter

The two unknowns in the Rosin Rammler equation are $\overline{d}$ and n_{RR}. The mean diameter of the drops can be determined from the measured cumulative mass distribution at the diameter value where the distribution equals e^{-1} and the values for the spread parameter can be found by

$$n_{RR} = \frac{ln(-lnY_d)}{ln\left(\frac{d}{\overline{d}}\right)} \tag{2.3}$$

The spread parameter is calculated for each drop size and the average value is subsequently used for the Rosin Rammler distribution curve.

The Sauter mean diameter [1981AL1] defined by equation (1.2) is a uniform drop diameter for a monodisperse drop distribution that is representative of a polydisperse drop distribution having similar heat and mass transfer and pressure drop characteristics. Pierce [2007PI1] modelled (CFD) the performance of a counter flow rain zone as well as a circular wet cooling tower rain zone based on a polydisperse drop distribution and showed that the results compared favourably with a monodisperse drop distribution based on the Sauter mean diameter. Merkel numbers varied between 4% and 6% for the circular cooling tower rain zone while the inlet loss coefficients varied by 5 %. The counter flow loss coefficients varied between 16% and 18% and the Merkel numbers varied between 8% and 10 %.

$$d_{32} = \frac{\sum nd^3}{\sum nd^2} \tag{1.2}$$

2.3.2 Water flow rate measurement

The water flow measurement is done by measuring the pressure difference over a venturi flow meter with the aid of a pressure transducer. The calibration curves for the venturi meter and

pressure transducer are provided in Appendix E. The location of the venturi flow meter can be seen in figure 2.1.

2.3.3 Air flow rate measurement

The air flow measurement is done by measuring the pressure difference over the air flow nozzle that is situated below the axial fan at the top of the cooling tower test facility as can be seen in figure 2.1. The pressure difference over the air flow nozzle is measured using a Betz manometer. The calibration curve for the air flow nozzle is also provided in Appendix E.

2.4 Test procedure

The test procedure for the measurement of the drop size distributions can be divided into two main sections:

1. The physical taking of the digital images.
2. The extraction of the data from these images using the image processing software developed for this purpose.

2.4.1 Taking digital images

1) Insert the camera housing into the desired position in the cooling tower test section.
2) Set the cooling tower test section to the desired water and air flow conditions.
3) Switch on the backlights.
4) Set the camera to the correct settings. A shutter speed of 1/8000 is used, but F-Stop must be set according to the light conditions, normally around F8. The camera is also set to its maximum zoom.
5) Set the remote trigger on the camera if it is used.
6) Place the camera into the housing and fasten it to the mounting that is provided.
   Make sure the backlights illuminate the photographic region evenly by firstly taking a few test photographs and secondly by visually inspecting the results.
7) Close the pipe end cover plate at the back of the camera housing.
8) Capture images by triggering the camera with the remote or through a hole that is provided on the camera housing.
9) Open the pipe end cover plate at the back of the camera housing.
10) Remove camera from its housing.
11) Change the air and water flow settings in the test section for the next test or turn everything off.

2.4.2 Image processing and data extraction from images

1) Connect the camera to a personal computer.
2) Download the images on the camera to the computer.
3) Open the image processing software program.
4) Load an image into the software program with the “Open File” command in the “File Exchange” menu.
5) Set the correct parameter values in the “Filter Parameters” menu as discussed in Appendix F.
6) Run the software program to extract the data from the image.
7) Inspect the results obtained with the software by comparing the original image with the results after the image processing is completed.
8) Export the data to Excel by clicking on the “Excel Export” button.
9) Process the data and plot the desired graphs.

2.5 Results

In this section the drop measurement results below different types of cooling tower fill and different configurations of the expanded metal grid and the slat grid are provided. The test cases for the fill tests are provided in table 2.1.

Table 2.1 : Test cases for fill tests

Water [kg/m^{2}s] / Air [kg/m^{2}s]	1.40	2.84	4.20
1.22	X	X	X
1.71	X	X	X
2.28	X	X	X
2.85	X	X	X

Splash grid tests are done with a water flow rate of 2.84 kg/m^{2}s and no air flow.

2.5.1 Characteristic drop distribution under different fill types

2.5.1.1 Film fill

In this test, the drop distributions 260 mm under a cross-fluted film packing, as shown in figure 2.12, is measured. Two layers of fill are installed perpendicular to each other in the cooling tower test facility which corresponds to a fill height of 600 mm.

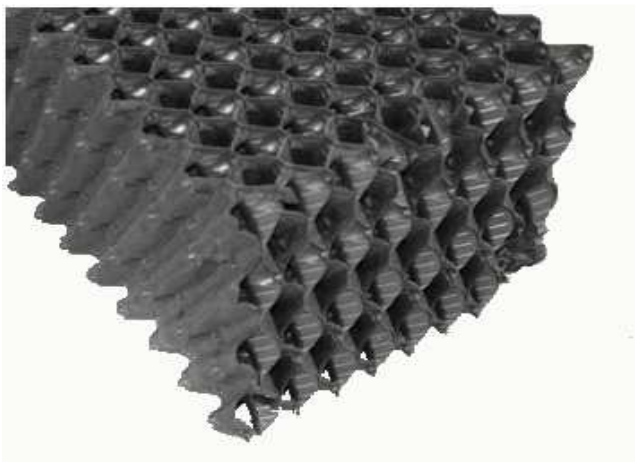

Figure 2.12 : Film fill

The measured cumulative mass distributions can be seen in figure 2.13 to figure 2.16, as well as the empirical Rosin Rammler distribution curve.

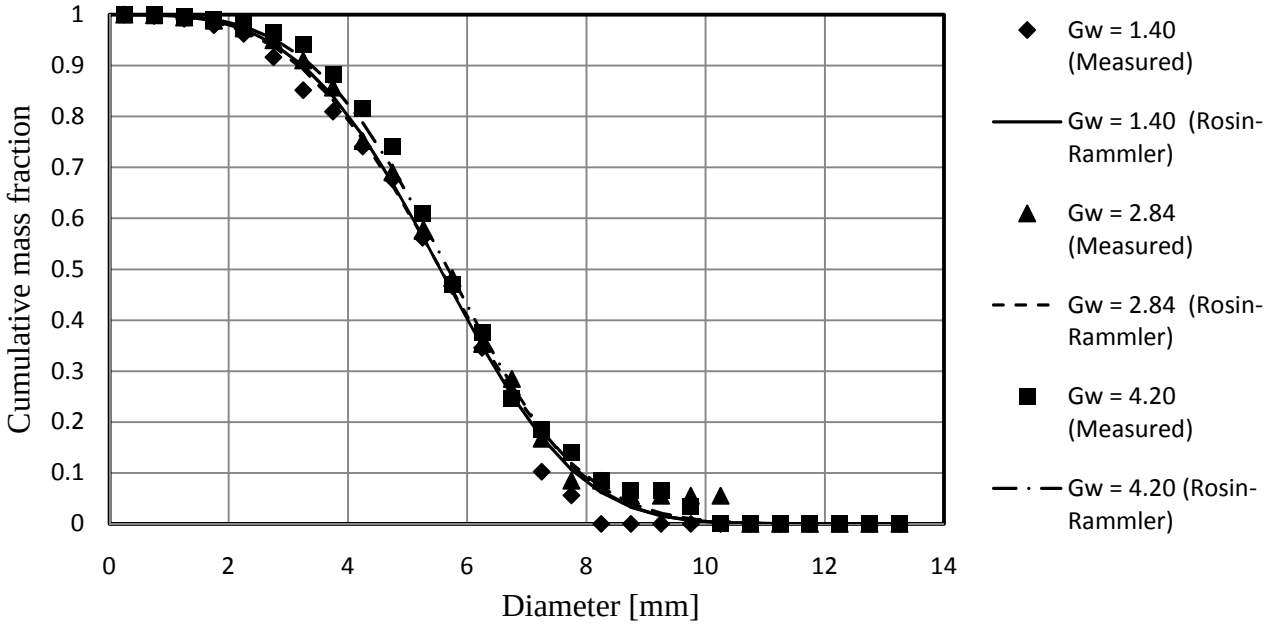

Figure 2.13 : Cumulative mass distribution directly under film packing, G_a = 1.22 kg/m^{2}s

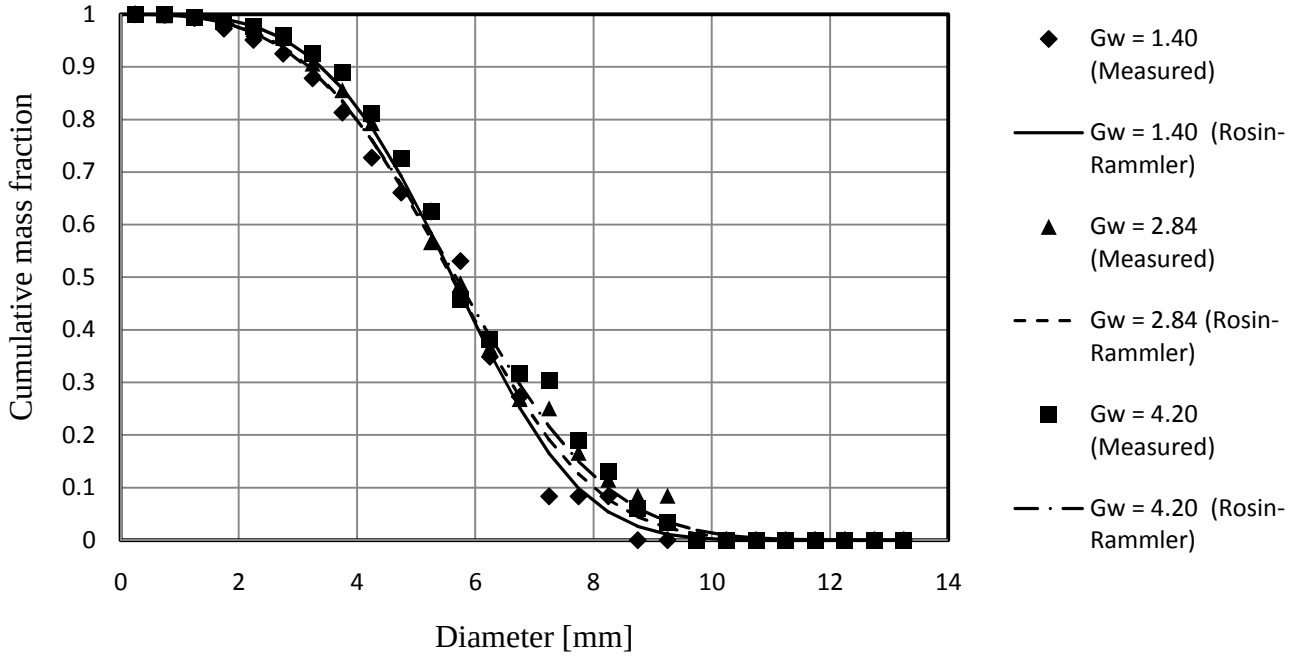

Figure 2.14 : Cumulative mass distribution directly under film packing, G_a = 1.71 kg/m^{2}s

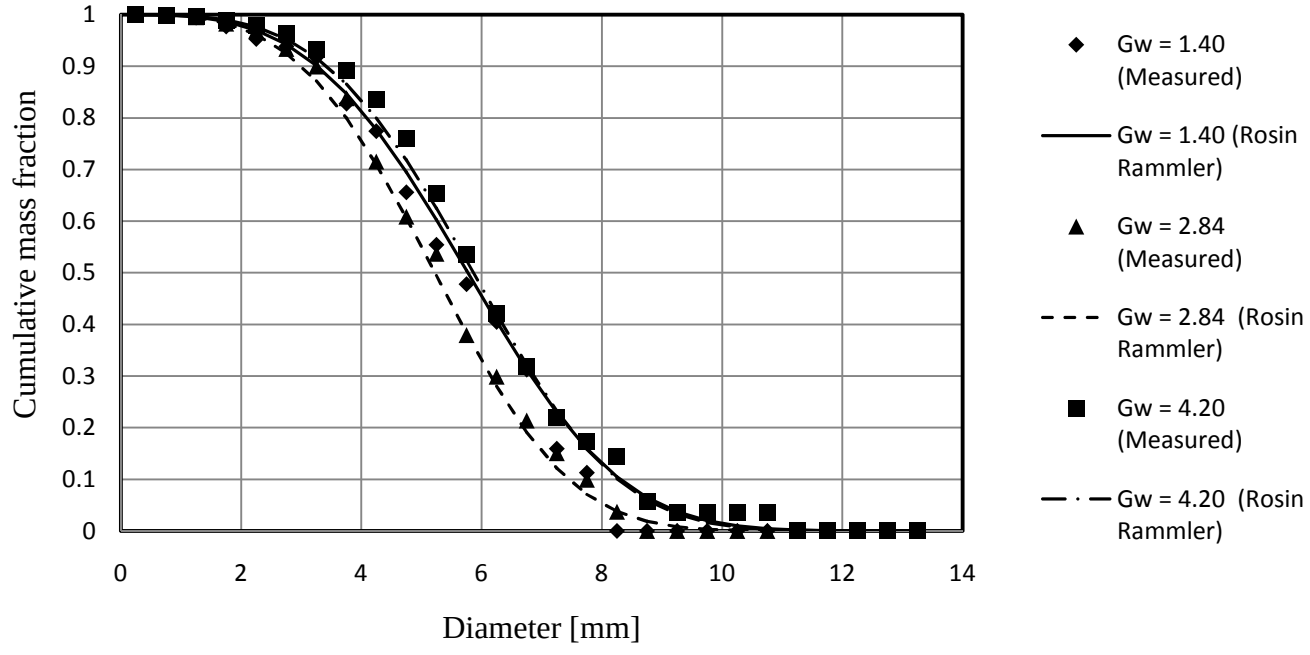

Figure 2.15 : Cumulative mass distribution directly under film packing, G_a = 2.28 kg/m^{2}s

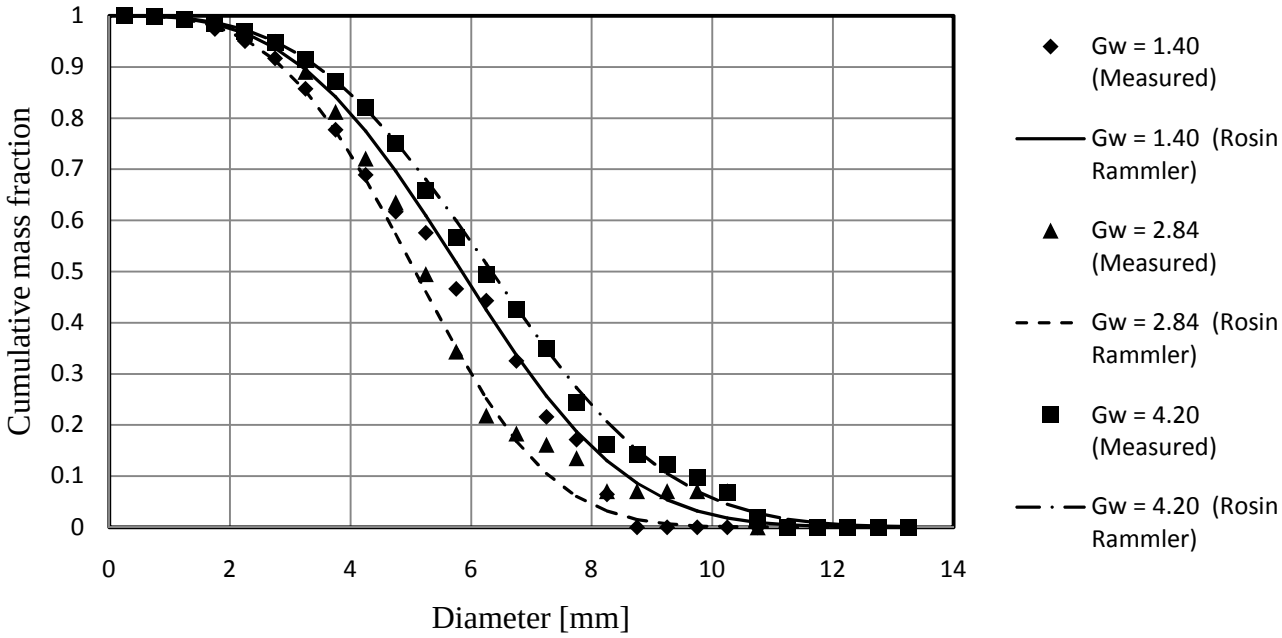

Figure 2.16 : Cumulative mass distribution directly under film packing, G_a = 2.85 kg/m^{2}s

In figure 2.17 the Sauter mean diameter for all the measured cases (Table 2.1) are plotted for the different air and water mass flow combinations considered.

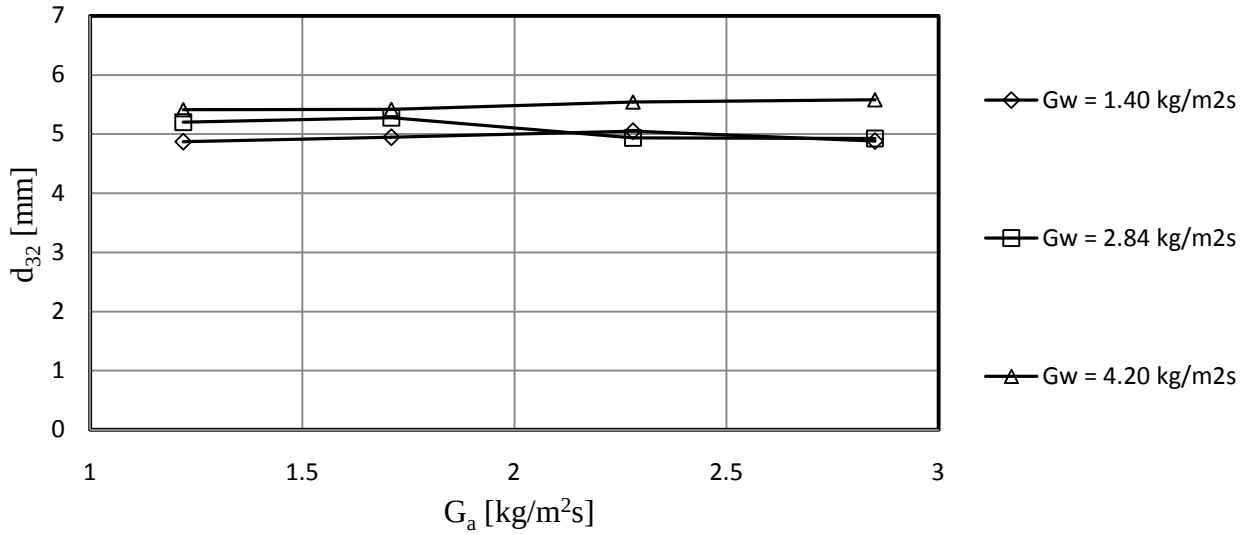

Figure 2.17 : Sauter mean diameters directly under film packing

In table 2.2 the Rosin Rammler constants, as used in equation (2.2), are provided together with the corresponding Sauter mean diameters. Appendix G provides the measured cumulative mass distributions for the various air and water flow combinations under the film fill.

Table 2.2 : Constants for Rosin Rammler equation with Sauter mean diameters of film fill

G_a/G_w	G_a	G_w	$\bar{d}$[mm]	n_{RR}[-]	d_{32}
0.2905	1.22	4.20	6.2774	3.6730	5.4116
0.4071	1.71	4.20	6.3538	3.2340	5.4173
0.4296	1.22	2.84	6.1916	3.3749	5.2000
0.5429	2.28	4.20	6.5107	3.5090	5.5412
0.6021	1.71	2.84	6.2437	3.3720	5.2764
0.6786	2.85	4.20	7.1255	3.1174	5.5773
0.8028	2.28	2.84	5.8210	3.4027	4.9356
0.8714	1.22	1.40	6.1586	3.5117	4.8723
1.0035	2.85	2.84	5.6687	3.3080	4.9228
1.2214	1.71	1.40	6.1974	3.7615	4.9463
1.6286	2.28	1.40	6.4483	3.3095	5.0502
2.0357	2.85	1.40	6.5690	3.1312	4.8789

2.5.1.2 Trickle fill

In this section the measured drop distributions 260 mm under a double layer of trickle fill can be seen. This corresponds to a fill height of 900 mm. An example of the trickle fill used in these measurements can be seen in figure 2.18.

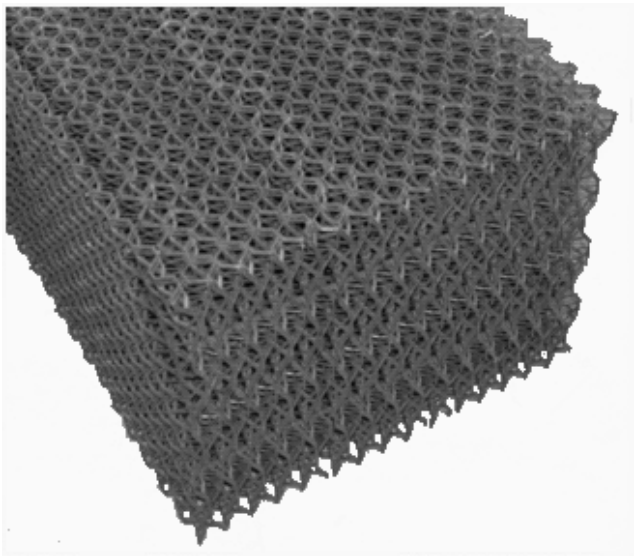

Figure 2.18 : Trickle fill

The measured cumulative mass distributions can be seen in figure 2.19 to figure 2.22 together with corresponding empirical Rosin Rammler distribution curves.

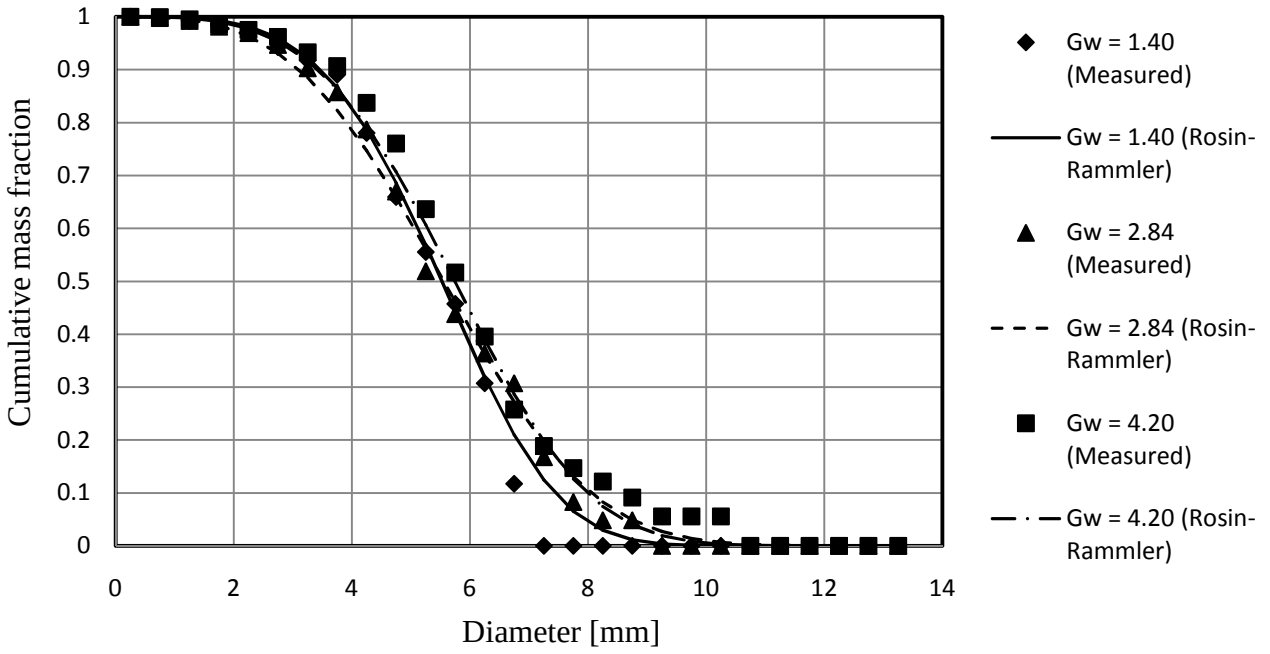

Figure 2.19 : Cumulative mass distribution directly under trickle fill, G_a = 1.22 kg/m^{2}s

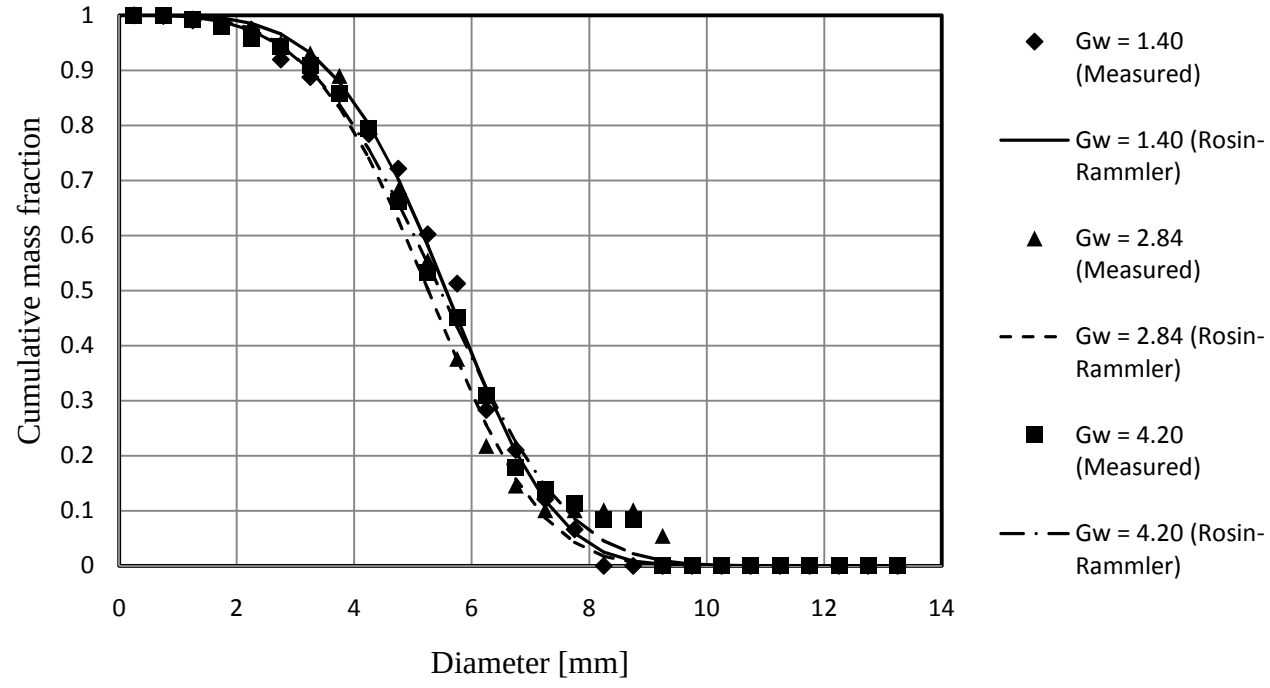

Figure 2.20 : Cumulative mass distribution directly under trickle fill, G_a = 1.71 kg/m^{2}s

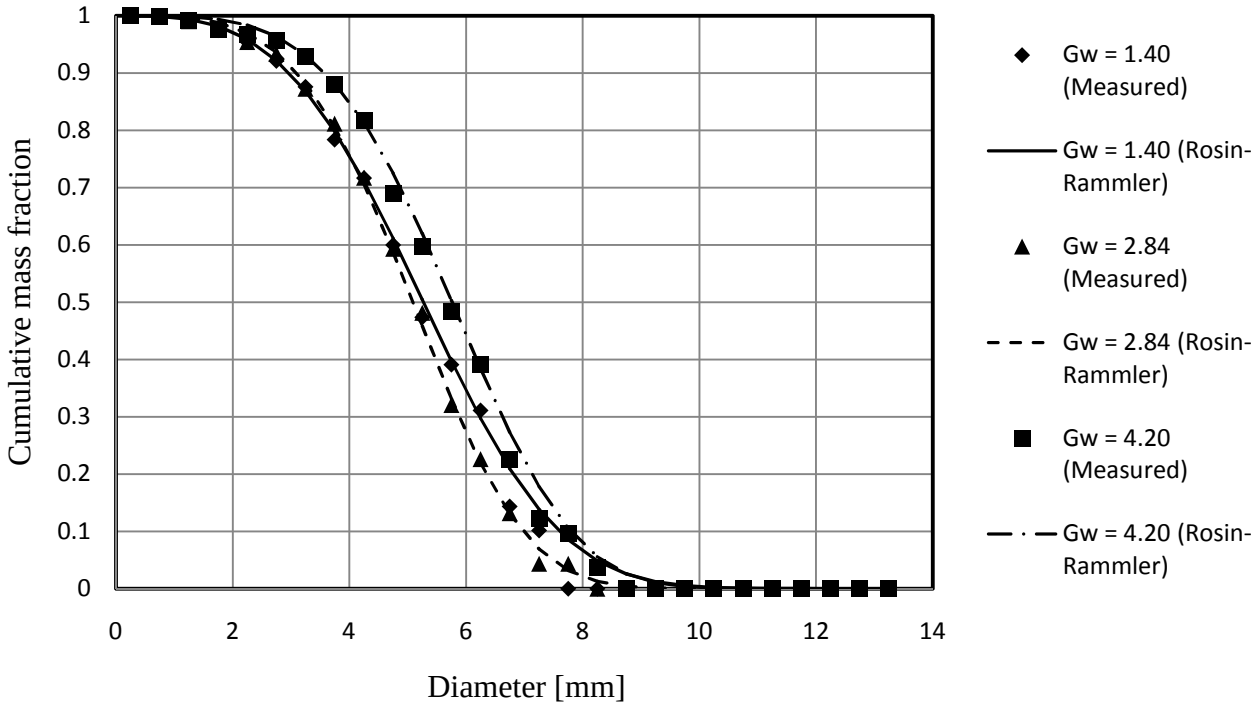

Figure 2.21 : Cumulative mass distribution directly under trickle fill, G_a = 2.28 kg/m^{2}s

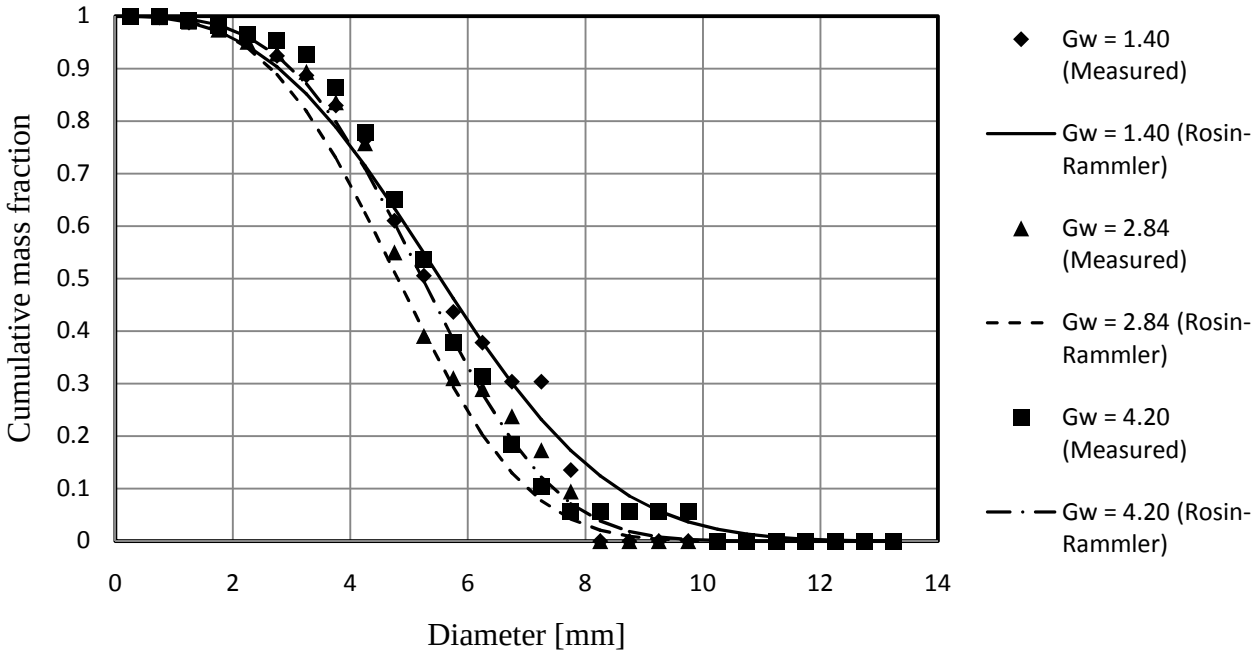

Figure 2.22 : Cumulative mass distribution directly under trickle fill, G_a = 2.85 kg/m^{2}s

In figure 2.23 the measured Sauter mean diameters are plotted for the different air and water mass flow rates considered.

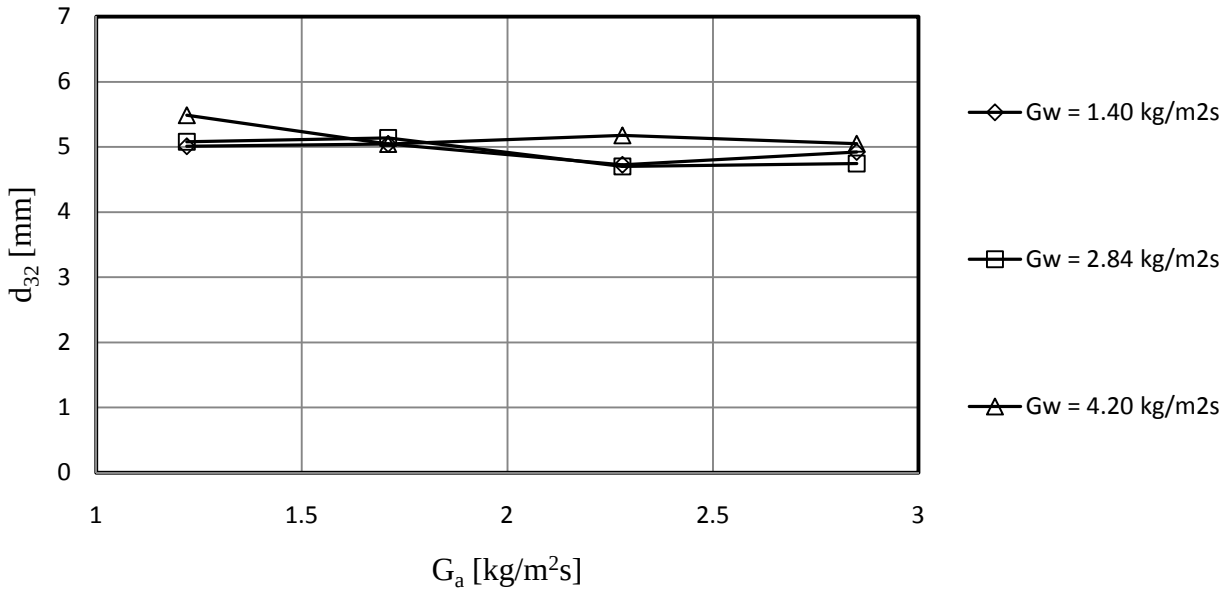

Figure 2.23 : Sauter mean diameter directly under trickle fill

In table 2.3 the Rosin Rammler constants, as used in equation (2.2), are provided together with the corresponding Sauter mean diameters. The measured distributions for the different air and water flow combinations under the trickle fill are provided in Appendix G.

Table 2.3 : Constants for Rosin Rammler equation with Sauter mean diameters of trickle fill

G_a/G_w	G_a	G_w	$\bar{d}$[mm]	n_{RR}[-]	d_{32}
0.2905	1.22	4.20	6.3512	3.6495	5.4849
0.4071	1.71	4.20	6.0442	3.6300	5.0442
0.4296	1.22	2.84	6.2215	3.2368	5.0785
0.5429	2.28	4.20	6.3202	3.9768	5.1762
0.6021	1.71	2.84	5.7752	3.9242	5.1365
0.6786	2.85	4.20	5.8233	3.3944	5.0504
0.8028	2.28	2.84	5.6024	3.8185	4.700
0.8714	1.22	1.40	6.0479	4.0532	5.0113
1.0035	2.85	2.84	5.3928	3.1790	4.7441
1.2214	1.71	1.40	6.0648	4.2493	5.0452
1.6286	2.28	1.40	5.8932	3.2932	4.7248
2.0357	2.85	1.40	6.3177	2.7542	4.9203

2.5.1.3 Fibre cement fill

The fill setup in the test section and the fill itself is shown in figure 2.24 and figure 2.25 respectively.

This type of fill was in former years commonly used in South African counter flow wet-cooling towers. It consists of vertical asbestos sheets, which are 4 mm thick, 900 mm high and spaced 20 mm apart.

Drop distribution measurements are taken 260 mm below the fill. Because of the fact that the water distribution system in the cooling tower test facility sprays the water vertically down and not like the sprayers that are used in the industry, the fill is covered with a layer of shade cloth on top. This is done to minimize the effect of the sprayers on the measurement by preventing the spray from falling through the fill without contact.

Figure 2.24 : Fill installation

Figure 2.25 : Fibre cement fill

The measured cumulative mass distributions, below the fibre cement fill, for different air and water flow combinations, together with the empirical Rosin Rammler function are shown in figure 2.26 to figure 2.29.

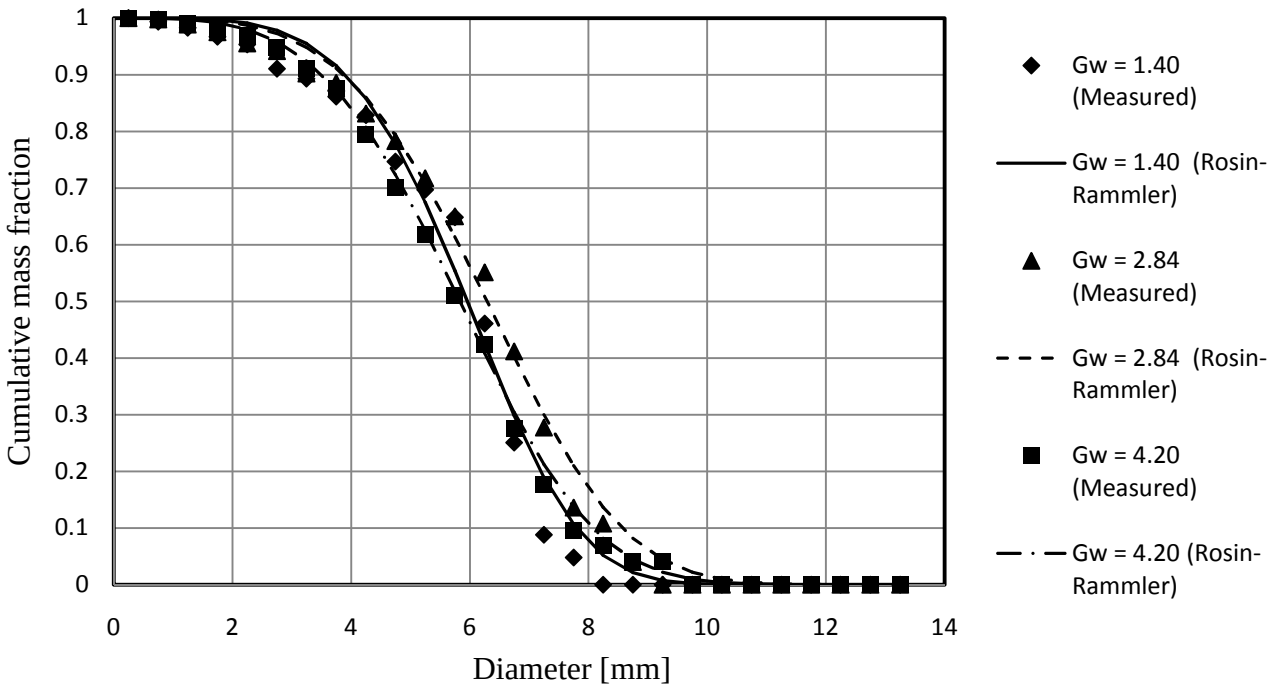

Figure 2.26 : Cumulative mass distribution directly under fibre cement fill, G_a = 1.22 kg/m^{2}s

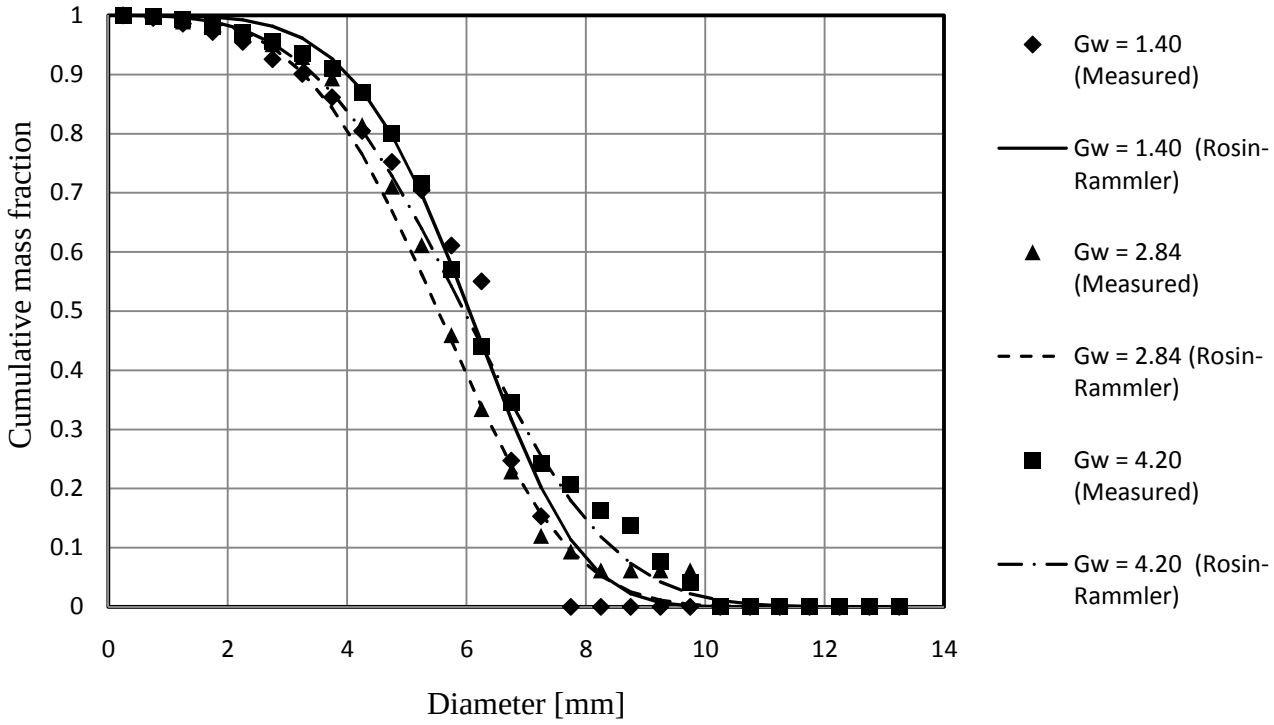

Figure 2.27 : Cumulative mass distributions directly under fibre cement fill, G_a = 1.71 kg/m^{2}s

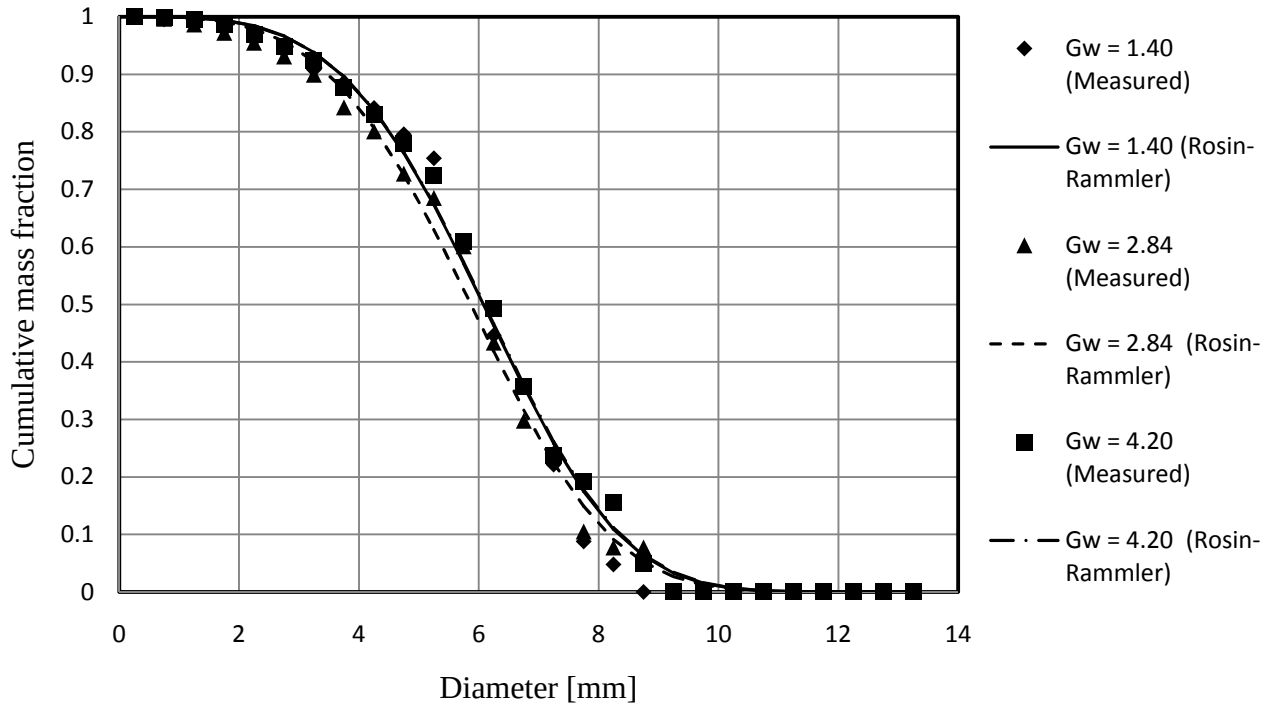

Figure 2.28 : Cumulative mass distribution directly under fibre cement fill, G_a = 2.28 kg/m^{2}s

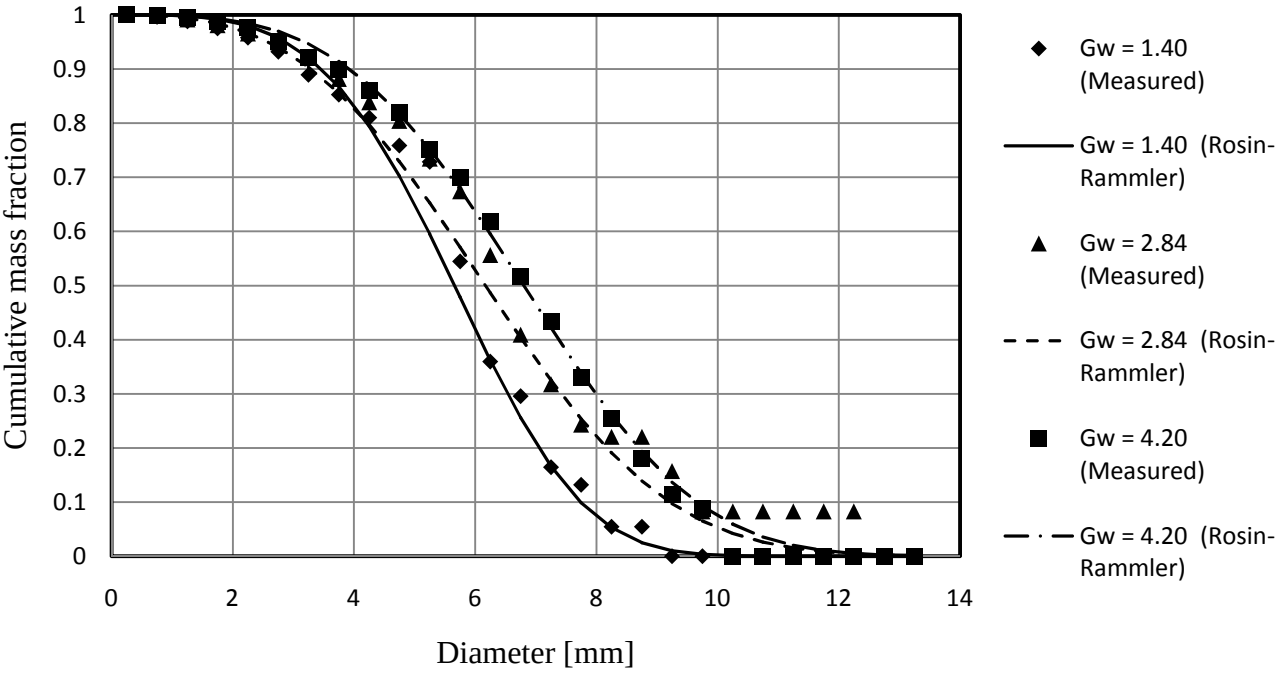

Figure 2.29 : Cumulative mass distribution directly under fibre cement fill, G_a = 2.85 kg/m^{2}s

Figure 2.30 shows a plot of the Sauter mean diameters for the corresponding air to water mass flow combinations.

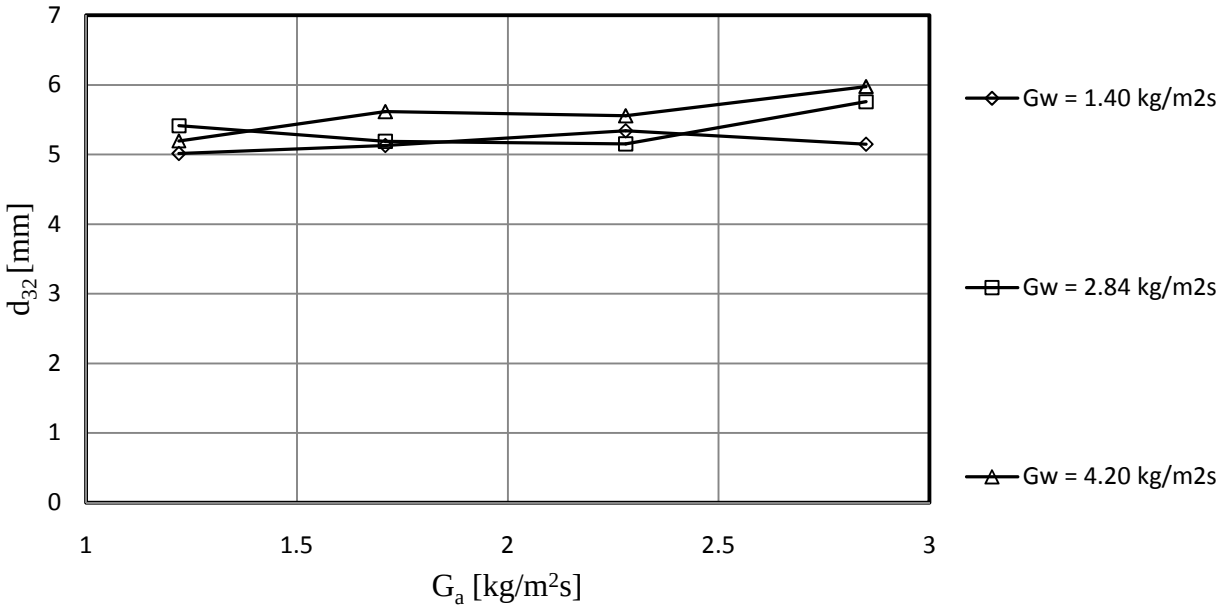

Figure 2.30 : Sauter mean diameter immediately below the fibre cement fill

Table 2.4 shows the Rosin Rammler parameters as well as the related Sauter mean diameters for the measured data. The measured data are provided in Appendix G.

Table 2.4 : Constants for Rosin Rammler equation with Sauter mean diameters of fibre cement

G_a/G_w	G_a	G_w	$\bar{d}$[mm]	n_{RR}[-]	d_{32}
0.2905	1.22	4.20	6.4404	3.7067	5.1950
0.4071	1.71	4.20	6.6276	3.4561	5.6161
0.4296	1.22	2.84	6.9125	3.8940	5.4159
0.5429	2.28	4.20	6.7114	3.8002	5.5570
0.6021	1.71	2.84	6.1159	3.6255	5.1885
0.6786	2.85	4.20	7.5694	3.4311	5.9771
0.8028	2.28	2.84	6.4924	3.6368	5.1519
0.8714	1.22	1.40	6.4706	4.4675	5.0127
1.0035	2.85	2.84	6.9743	2.9973	5.7606
1.2214	1.71	1.40	6.5510	4.6232	5.1288
1.6286	2.28	1.40	6.6962	3.8060	5.3386
2.0357	2.85	1.40	6.2274	3.8432	5.1471

2.5.2 Drop break-up characteristics of a specifically designed slat grid

In this section, drop distributions are measured below different arrangements of the slat grid specifically designed for this project, installed below the trickle fill. These arrangements include varying the height between the grid and the fill and also inserting multiple layers of the grid. Where multiple layers of the grid are used the spacing between the layers is kept at 60 mm and a staggered configuration is used. For these tests the water mass flow rate is kept constant at 2.84 kg/m^{2}s with no air flow. The Sauter mean diameter 260 m below the trickle fill for this case is 5.19 mm and below the water distribution system it is 3.57 mm. All measurements are provided in Appendix G.

The drop distribution measurements are always taken 260 mm below the lowest slat grid in the arrangement to ensure that all tests are conducted in a consistent manner. The results of the designed slat grid tests can be seen in figure 2.31.

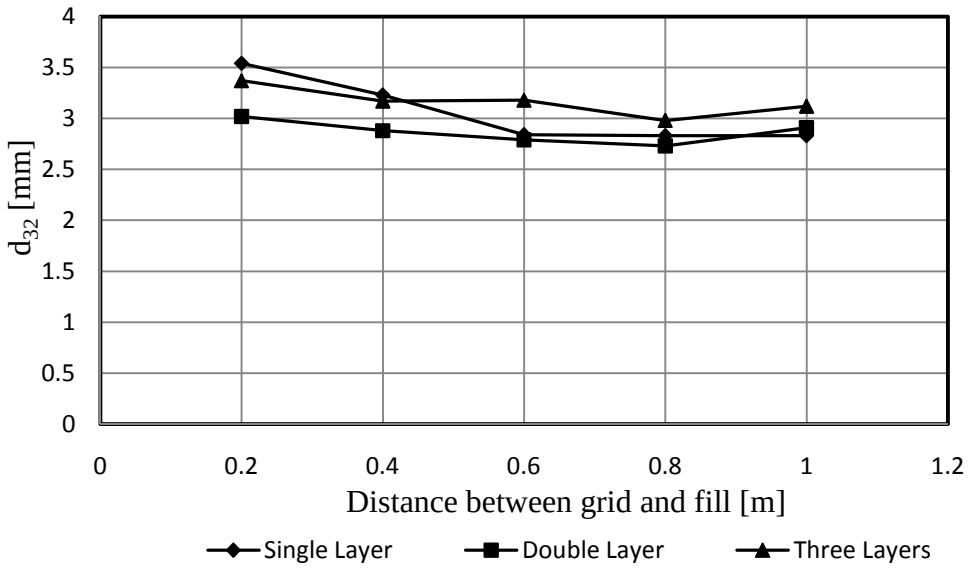

Figure 2.31 : Sauter mean diameter directly below different slat grid arrangements, G_w = 2.84 kg/m^{2}s

It can be seen from figure 2.31 that the optimum distance between the grid and the fill is in the region of 0.6 m to 0.8 m. It is in this region that the smallest Sauter mean diameters are measured below a single and double layer of grid. A similar phenomenon was observed by Oosthuizen [1995OO1] for a double layer of coarse expanded metal grid.

Figure 2.31 also show that three layers of grid give the worst results except at 0.2 m and 0.4 m where it is only slightly better than a single layer. This can be attributed to the fact that an

increased number of slats causes an increased amount of dripping below the arrangement. Primary dripping drop sizes for 3 mm slats are typically around 6 mm in diameter according to equation (4.21) [1994DR1].

There is some improvement in the drop size reduction when two layers of slat grid are staggered with respect to each other, as opposed to one layer. The reason for this is that it is possible for a drop larger than 6 - 7 mm to pass through one layer of the slat grid seeing that the spacing between the slats is 10 mm. The dripping below the 3 mm slats causes the formation of drops with diameters between 6 and 7 mm and the introduction of a second or third layer of grid also means an increased amount of dripping. Seeing that the Sauter mean diameter is much more sensitive to the number of larger drops, a second layer can still contribute to decreasing the Sauter mean diameter, because it eliminates the largest drops. However, when drops passed through the second layer all the drops larger than 6 – 7 mm are eliminated and the dripping effect from the third layer outweighs its contribution to drop break-up.

Other effects like counter flowing air, spacing between the different layers of slat grid, as well as drop break-up or coalescence that takes place as the drops travels through the rain zone below the grid needs to be investigated. Figure 2.32 show the layout of these experiments.

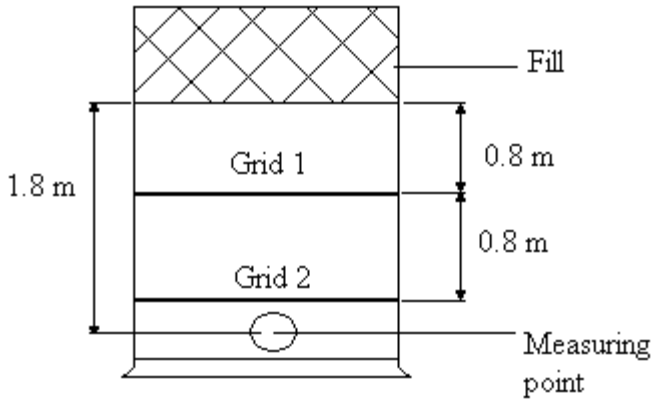

Figure 2.32 : Test setup for grid spacing and air tests

One layer of slat grid is placed 0.8 m below the cooling tower fill and the drop measurement is taken 1.8 m below the fill. The measurement is done with and without counter flowing air. This is then repeated when another grid is placed 0.8 m below the first grid. For all four cases

the water mass flow is 2.84 kg/m^{2}s and when counter flowing air is introduced in two of the cases the air mass flow is 2.28 kg/m^{2}s. The Sauter mean diameters for all four cases are given in table 2.5 and the measured data in Appendix G.

Table 2.5 : Sauter means for 0.8m grid spacing and air tests, G_w = 2.84 kg/m^{2}s

G_a [kg/m^{2}s]	Number of layers	d_{32} [mm]
0	1	2.83 [260 mm below grid]
2.28	1	2.85
0	1	2.54
2.28	2	2.48
0	2	2.47

Bad water quality often encountered in cooling towers can lead to fouling and blockage of splash grids, which could be avoided or reduced by increasing the slat pitch. Tests are therefore conducted on two grids installed 60 mm apart, where the slats are staggered and the pitch on each grid is increased to 20 mm by removing alternate slats. The goal is to obtain a slat configuration equivalent to that of a single grid tested above, but which provides larger openings for objects in the water to pass through. In figure 2.33 the measured Sauter mean diameters immediately below this configuration are compared to the Sauter mean diameters measured below a single grid of the original layout as shown in figure 2.3.

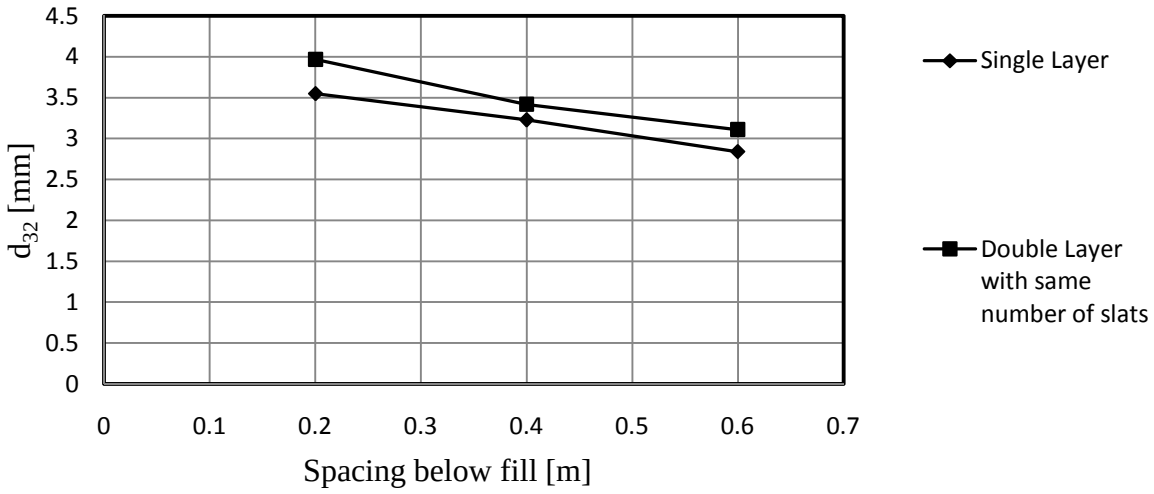

Figure 2.33 : Sauter mean diameters immediately below equivalent slat grid setups, G_w = 2.84 kg/m^{2}s

2.5.3 Drop break-up characteristics of expanded metal grid

The drop distribution directly below one and two layers of expanded metal grid is also measured for different spacings between the grid and the fill. The expanded metal grids are inserted below a trickle fill with no counter flowing air and a water mass flow of 2.84 kg/m^{2}s.

For the measurements done under a double layer of the grid, the spacing between the individual layers is 100 mm.

Figure 2.34 shows the results for the drop size measurements under the expanded metal grids.

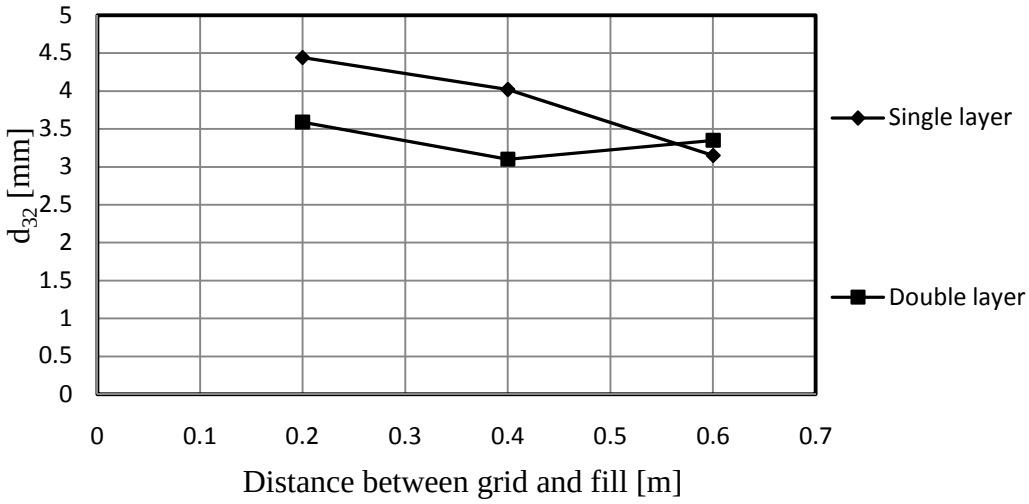

Figure 2.34 : Sauter means measured immediately below expanded metal grids, G_w = 2.84 kg/m^{2}s

2.6 Discussion of results

The drop distribution is measured below three types of cooling tower fill. The trickle fill produced the smallest drops followed by the film fill. The Sauter mean diameter for the distributions measured below the fills generally range from 5 – 6 mm, but Sauter means as large as 6.0 mm are measured below the fibre cement fill. The data for the trickle and film packing is in accordance with Kröger [2004KR1] where it is stated that the Sauter mean diameters below these types of fill are in the order of 5 – 6 mm. Oosthuizen [1995OO1] measured the drop distribution below a trickle fill and the Sauter mean varied between 5 – 5.5 mm. These values compare well with the results measured in this chapter although Oosthuizen

[1995OO1] took his measurement 2.125 m below the fill while the fill measurements in this chapter are done 260 mm below the fill.

As drops fall through the rain zone there is some break-up that takes place because of the increasing hydrodynamic forces on the front end of an accelerating drop, but the change in Sauter mean diameter tend to be relatively small. This can also be seen below a grid that is placed into the rain zone. By comparing the Sauter means measured 0.26 m below a single layer of slat grid with the Sauter mean measured 1 m below the same layer it can be seen that there is some drop size reduction over the rain zone, which can be seen in table 2.5. Over the 0.75 m, the Sauter mean diameter decreased from 2.83 mm to 2.54 mm. Drops do not only break up as they fall through the rain zone, but also collides with other drops. Dreyer [1994DR1] reported that these effects are negligible in performance calculations.

Two types of grids are inserted into the rain zone to reduce the drop sizes. The one is designed and the other one is made from commercially available expanded metal. Better drop break-up is achieved with the designed grid. Oosthuizen [1995OO1] inserted a double layer of coarse expanded metal grid below trickle fill and achieved a minimum Sauter mean of around 4.05 mm for a grid placement of 0.67 m below a trickle fill. For the designed grid a Sauter mean diameter of 2.73 mm is achieved with a double layer of grid placed 0.8 m below the trickle fill and spacing between the grids of 60 mm. If the spacing between the grids is increased to 0.8 while distance between the fill and grid is kept at 0.8 m, the Sauter mean diameter reduces to 2.47 mm. This is the smallest measured Sauter mean diameter.

2.7 Conclusion and recommendations

From the experimental work done in this chapter it becomes evident that the best spacing between a drop size reduction grid and the fill is between 0.6 m and 0.8 m. If the spacing is increased further the Sauter mean can either stay constant or start to increase again.

Better drop size reduction is achieved with the slat grid than with the expanded metal. The reason for this might be the areas in the expanded metal grid shown in figure 2.35, from which larger drops drip. When designing a splash grid care must therefore be taken to ensure that areas like these are eliminated.

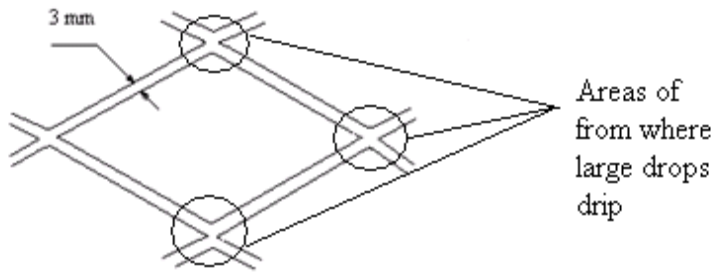

Figure 2.35 : Expanded metal dripping regions

Now that the best location for a grid is determined it is also necessary to find the best layout for the slat grid (chapter 4) in terms of slat spacing and slat width. The profile of the bottom of the slat must also be taken into account to minimize the size of the drops that drip from below the slats. This is something that needs to be improved if better drop size reduction is to be achieved with multiple layer setups where more than two layers of slat grid are to be used. It can be seen in figure 2.31 that the Sauter mean is worse for a three layer setup of the slat grid than for a double layer setup when normal slats as shown in figure 2.3 are used.

3

MODELLING OF MOTION AND COOLING OF SINGLE DROPS FALLING THROUGH AIR

3.1 Introduction

In this chapter the thermal and dynamic behaviour of a falling drop in 2 dimensions is modelled by numerically solving the equations of motion and cooling derived from first principles. Existing correlations for the mass transfer, heat transfer and drag coefficients are incorporated in the governing differential equations in order to solve them. At the end of the chapter the results obtained from the model are presented.

It is important for the work done in this thesis to be able to model the cooling, velocity and trajectory of a single drop in still air as well as in counter and cross flowing air. The results of motion obtained from this work provide input data for the model of chapter 4 for determining the size reduction of drops by means of evenly spaced slats. In order to model the drop size reduction it is necessary to know the speed at which a drop will impact a given slat if it falls from a certain height. The different drag models show that the effect of drop deformation on the speed of a drop falling from heights normally associated with cooling tower rain zones is negligible. The results obtained are used for the validation of CFD models and the numerical models for cross flow in chapter 5. The results are also used to determine the Merkel [1925ME1] transfer characteristic for a rain zone under the assumption that air properties stay constant as well as the pressure drop for a monodisperse rain zone.

3.2 Background

The governing differential equation for drop speed is derived from Newton's second law and a correlation for drag from literature is used in this equation. From literature it can be seen that there are a number of ways in which the drag for a drop can be modelled. A number of correlations are found in literature for spheres and are correlated by researchers such as Turton and Levenspiel [1986TU1], Clift et. al. [1978CL1], Ferreira [1997FE1] etc.

Dreyer [1994DR1] proposed a correlation for the drag coefficient of accelerating drops, which includes the effect of drop deformation. He correlated the data from Beard and Chuang [1987BE1] for the drag coefficient of a deforming drop at terminal velocity. Dreyer [1994DR1] proposed a correlation for drop deformation during acceleration that is a function of drop velocity and then went on to propose a correlation for the drag coefficient that takes the drop deformation into account.

The governing differential equations for temperature change are derived from the first law of thermodynamics. Correlations are employed for the heat and mass transfer coefficients based on the heat and mass transfer analogy. Numerous researchers studied heat and mass transfer from drops: Frossling [1938FR1], Snyder [1951SN1], Ranz and Marshall [1952RA1], Yao and Schrock [1976YA1], Miura et. al. [1977MI1], Srikrishna et. al. [1982SR1].

3.2 Governing differential equations and numerical methods

3.2.1 Governing equations for drop velocity

The free body diagram for a drop falling through air coming from the side at a certain angle can be seen in figure 3.1. Figure 3.1 also illustrates the angle of the air velocity relative to the drop as well as the drop speed.

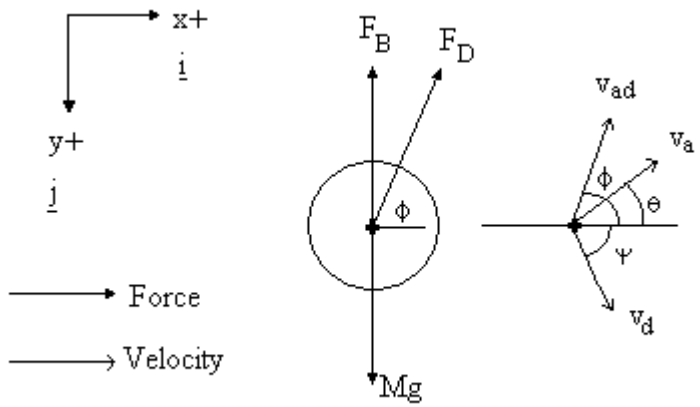

Figure 3.1: Free-body diagram of a falling drop in an air stream

From Newton's second law, the following vector equation in Cartesian co-ordinates can be derived for the momentum change of the drop as a result of forces acting on it.

$$\mathbf{F_R} = \left(v_{dx}\mathbf{i} + v_{dy}\mathbf{j}\right)\frac{\partial M}{\partial t} + M\left(\frac{\partial v_{dx}}{\partial t}\mathbf{i} + \frac{\partial v_{dy}}{\partial t}\mathbf{j}\right) \tag{3.1}$$

The relative velocity between the air and the drop is expressed by

$$\mathbf{v_{ad}} = \left(|v_a|\cos\theta - v_{dx}\right)\mathbf{i} - \left(|v_a|\sin\theta + v_{dy}\right)\mathbf{j} \tag{3.2}$$

The angle ϕ for the relative velocity and also the drag force is given by

$$\phi = \tan^{-1}\left(\frac{-\left[|v_a|\sin\theta + v_{dy}\right]}{|v_a|\cos\theta - v_{dx}}\right) \tag{3.3}$$

The magnitude of the drag force acting on the drop is given by

$$|F_D| = \frac{1}{2}C_D\rho_{av}|v_{ad}|^2A_f \tag{3.4}$$

The resultant force acting on the drop is the vector sum of the drag, weight and buoyancy forces and can now be given by

$$\mathbf{F_R} = \left(|F_D|\cos\phi\right)\mathbf{i} + \left(\rho_d V_d g - |F_D|\sin\phi - \rho_{av}V_d g\right)\mathbf{j} \tag{3.5}$$

By substituting equation (3.5) back into equation (3.1), the equation for drop motion in two dimensions can be expressed as

$$\begin{aligned}\left(\frac{\partial v_{dx}}{\partial t}\mathbf{i} + \frac{\partial v_{dy}}{\partial t}\mathbf{j}\right) &= M^{-1}\Big[\left(|F_D|\cos\phi\right)\mathbf{i} + \left(\rho_d V_d g - |F_D|\sin\phi - \rho_{av}V_d g\right)\mathbf{j} \\ &\quad - \left(v_{dx}\mathbf{i} + v_{dy}\mathbf{j}\right)\frac{\partial M}{\partial t}\Big]\end{aligned} \tag{3.6}$$

When modelling the drag of a water drop it can be assumed that the drop stays spherical the whole time, while the more correct method is to take the effect of drop deformation into account.

If the drop is modelled as a perfect sphere the correlation for drag coefficient proposed by Turton and Levenspiel [1986TU1] can be used as given by equation (3.7). According to Clift [1978CL1] the dynamic behaviour of a falling drop is well approximated by a spherical model if the Eotvos (Eo) number is smaller than 0.15.

$$C_{D.sphere} = 24\frac{\left(1 + 0.173{Re_d}^{0.657}\right)}{Re_d} + \frac{0.413}{\left(1 + 16300{Re_d}^{-1.09}\right)} \tag{3.7}$$

This equation gives good results for low Reynolds numbers and small drop diameters or in other words, falling drops with Eotvos numbers smaller than 0.15. When Reynolds numbers start to increase or drop diameters get larger this assumption is not valid anymore because drop shapes start changing to non-symmetrical ellipsoidal shapes [1994DR1]. This happens because of the increasing hydrodynamic pressure at the front surface of the drop while the rear has a more uniform hydrodynamic pressure [1994DR1], [1978CL1]. According to Clift [1978CL1] the increasing oblateness of a drop at higher Reynolds numbers tends to promote the formation of a wake behind the drop that in turn leads to vortex shedding, which subsequently leads to higher drag coefficients. Clift [1978CL1] reported that the appearance of a wake and the onset of wake shedding occur at Re values of between 20 and 200 respectively when the system is contaminated. However, for a purified system with the same properties the wake can be delayed to Re = 800. Secondary motion like drop oscillation also occurs in a falling drop and the onset of this motion coincides with the onset of vortex shedding from the wake [1978CL1].

To take the deformation of a drop into account when calculating drag coefficient, one starts by determining the aspect ratio of a spherical body that is defined by

$$E = \left(\frac{d_a}{d_b}\right) \tag{3.8}$$

where d_a and d_b are depicted in figure 3.2.

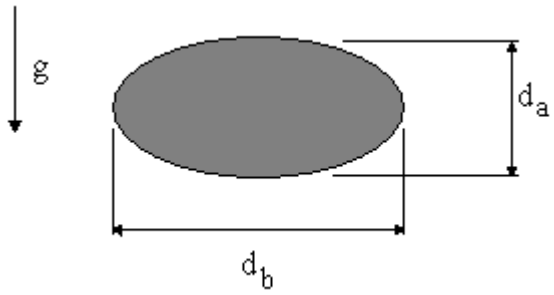

Figure 3.2 : Deformed drop geometry

Dreyer [1994DR1] correlated the data for drop deformation at terminal velocity that was measured by Beard and Chuang [1987BE1].This correlation is given by

$$E_T = (1 + 0.148Eo^{0.85})^{-1} \qquad Eo > 0 \tag{3.9}$$

where the Eotvos number, Eo, is given by:

$$Eo = \frac{g{d_d}^2(\rho_d - \rho_{av})}{\sigma_d} \tag{3.10}$$

Dreyer [1994DR1] also proposed a correlation for the deformation of an accelerating drop which is given by

$$E = 1 - \left(\frac{v_d}{v_T}\right)^2 (1 - E_T) \tag{3.11}$$

The improved drag coefficient can now be determined from

$$\left(\frac{C_D}{C_{D,sphere}}\right) = 1 - 0.17185(1 - E) + 6.692(1 - E)^2 - 6.605(1 - E)^3 \tag{3.12}$$

It should be noted that the improved drop drag coefficient is based on the actual frontal area of the deformed drop with the diameter of the deformed drop given by

$$d_{fr} = d_{d,sphere}E^{-1/3} \tag{3.13}$$

3.2.2 Governing equations for temperature change

In figure 3.3 the control volume for a drop is shown that is subjected to heat and mass transfer.

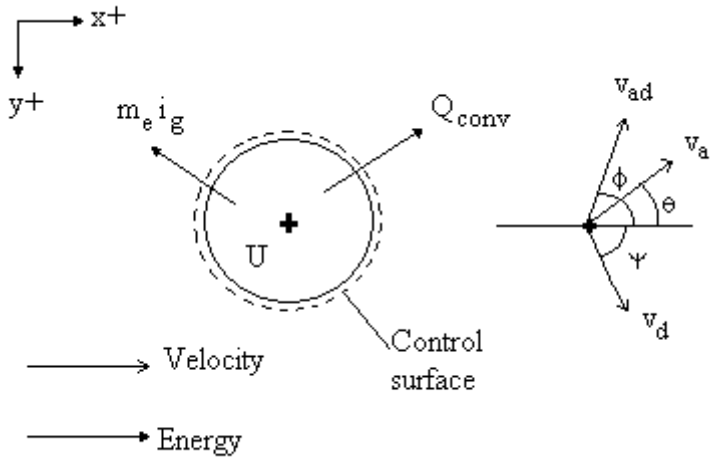

Figure 3.3 : Control volume for a cooling drop

From the first law of thermodynamics the rate of energy change in a falling drop can be derived and is given by

$$\frac{\partial U}{\partial t} = -Q_{conv} - m_e i_g \tag{3.14}$$

The rate of change of the internal energy of the drop can also be expressed by

$$\frac{\partial U}{\partial t} = \frac{\partial (M c_v T)}{\partial t} = MT\frac{dc_v}{dt} + Mc_v\frac{dT}{dt} + c_v T\frac{dM}{dt} \tag{3.15}$$

In equation (3.15) the assumption can be made that the rate of change of the specific heat is negligible and the specific heat for constant pressure equals the specific heat for constant volume in a water drop. The rate of change of internal energy can now be given by the following relation:

$$\frac{\partial U}{\partial t} = Mc_p\frac{dT}{dt} + c_p T\frac{dM}{dt} \tag{3.16}$$

By combining equations (3.16) and (3.14) and by realizing that m_e = -dM/dt, the rate of temperature change in a falling drop can be expressed by

$$\frac{dT}{dt} = \frac{-m_e i_{fg} - Q_{conv}}{M c_{pw}} \tag{3.17}$$

The convection heat transfer can be modelled by using the following equation for convection heat transfer rate.

$$Q_{conv} = h_c A_s (T - T_\infty) \tag{3.18}$$

The only unknown in equation (3.18) is the convection heat transfer coefficient h_c, which can be determined from the Nusselt number. Ranz and Marshall [1952RA1] proposed the following correlation for spheres:

$$Nu_d = 2 + 0.6 Re_d^{\frac{1}{2}} Pr_{av}^{\frac{1}{3}} \qquad for \qquad 2 \leq Re \leq 800 \tag{3.19}$$

All properties in equation (3.19) are evaluated at the film temperature between the drop and the surrounding air.

Martin [2005MA1] proposed the following correlation for Nusselt number in terms of friction factor which comes from the analogy that exist between frictional pressure drop and heat transfer

$$Nu_d = 2 + 0.4038\left(c_F Re_d{}^2 Pr\right)^{\frac{1}{3}} \quad for \quad 10^{-1} \leq Re \leq 10^6 \tag{3.20}$$

where

$$c_F = 16/Re + 3.73 Re^{\frac{1}{2}} + 0.03 \tag{3.21}$$

Pierce [2007PI1] made use of a modified form of the equation by Ranz and Marshall [1952RA1]

$$Nu_d = 2 + 0.6 g_{YS} Re_d^{\frac{1}{2}} Pr_{av}^{\frac{1}{3}} \qquad for \qquad Re < 2500 \tag{3.22}$$

where

$$g_{YS} = 0.68\left(\frac{C_D Re^2}{(C_D Re^2)_T}\right)^{-0.28} + \frac{0.95}{\left(1 + 1.4\left(\frac{C_D Re^2}{(C_D Re^2)_T}\right)^{-2}\right)} \tag{3.23}$$

When the Nusselt number is determined, the heat transfer coefficient can be obtained from the definition of the Nusselt number.

$$Nu_d = \frac{h_c d}{k_{av}} \tag{3.24}$$

There is also enthalpy transfer to the air stream because of evaporation that takes place. In order to quantify the enthalpy transfer the mass transfer rate must be determined

The mass transfer [1996IN1] from a drop travelling through air at a certain velocity can be expressed approximately by

$$m_e = h_D A_S(\rho_{vs} - \rho_{v\infty}) \tag{3.25}$$

In order to determine the mass transfer rate from the drop, the mass transfer coefficient h_D must be obtained. This can be obtained by first determining the Sherwood number as correlated by Ranz and Marshall [1952RA1].

$$Sh_d = 2 + 0.6 Re_d^{\frac{1}{2}} Sc^{\frac{1}{3}} \tag{3.26}$$

Martin [2005MA1] proposed the following correlation for the Sherwood number in terms of friction factor

$$Sh_d = 2 + 0.4038(c_F Re^2 Sc)^{\frac{1}{3}} \tag{3.27}$$

with c_F given by equation (3.21).

The mass transfer coefficient can now be obtained from the definition of the Sherwood number as given by

$$Sh_d = \frac{h_D d}{D_{AB}} \tag{3.28}$$

All properties for the Sherwood number are evaluated at the film temperature between the drop and the air.

Different diffusion coefficients exist in literature [1984PE1] [1934GI1], but Gilliland [1934GI1] is considered adequate for the drop model and can be obtained from

$$D_{AB} = \frac{\left[0.04357 {T_{db}}^{1.5} \left[\frac{1}{M_a} + \frac{1}{M_v}\right]^{0.5}\right]}{\left[P_{atm}\left(V_a^{\frac{1}{3}} + V_v^{\frac{1}{3}}\right)^2\right]} \tag{3.29}$$

where M_a and M_v are the molar mass values for the air and water vapour respectively and V_a and V_b are the corresponding molecular volumes. For air M_a = 28.97 kg/mol and V_a = 29.9 m^3/mol, while for water vapour M_v = 18.016 kg/mol and V_v = 18.8 m^3/mol.

A Merkel number for the rain zone based on the Lagrangian method for a single drop in which the air side enthalpy and temperature changes are ignored can be determined from the relation for Merkel number given by

$$Me = \frac{h_d a_{rz} H_{rz}}{G_w} \tag{3.30}$$

where h_d is determined from the assumption that the Lewis factor ($h_c/h_d c_{pma}$) equals unity and a_{rz} is the ratio of the total drop surface area contained in m_w to the total volume over which these drops are spread in the rain zone. The volume over which the drops are spread is simply the cross sectional area of the rain zone multiplied by the distance the drop under consideration falls in one second.

The relation between h_D and h_d is given by

$$h_d = h_D\,(c_{sw} - c)/(w_{sw} - w) \tag{3.31}$$

3.3 Results

Figure 3.4 shows the velocities of single drops for different path lengths. In figure 3.5 the temperature change for different drop sizes are determined. The results of this section are obtained with air dry bulb and wet bulb temperatures of 298 K and 295.76 K respectively and atmospheric pressure of 101325 Pa. The initial water temperature is 323 K. A sample calculation for a single drop falling in still air is provided in Appendix H.

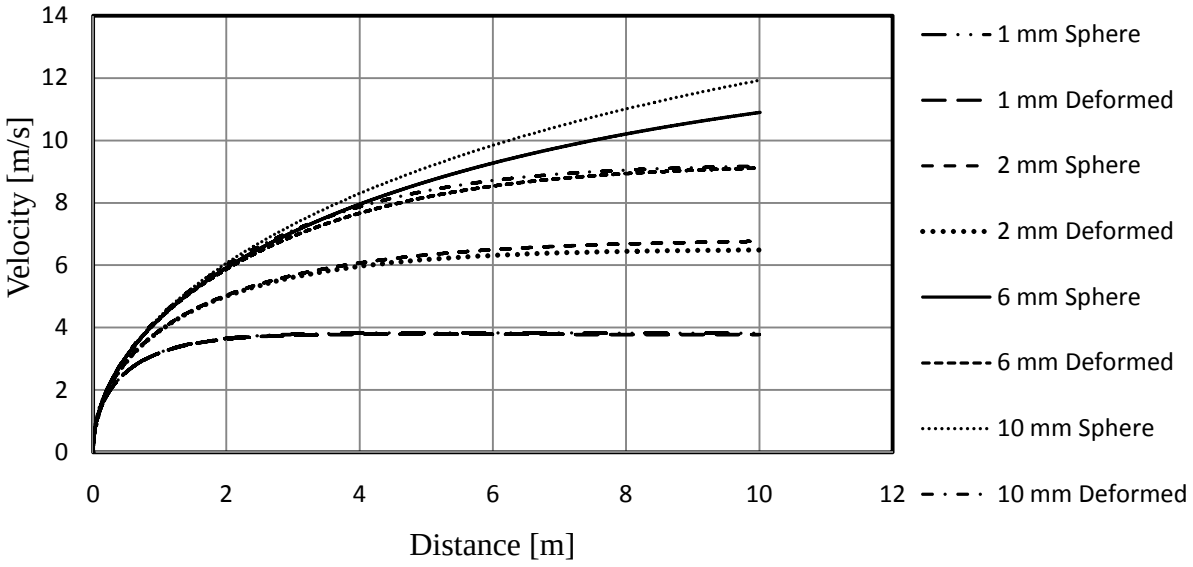

Figure 3.4 : Comparison of velocity between drop deformation and non-deformation model

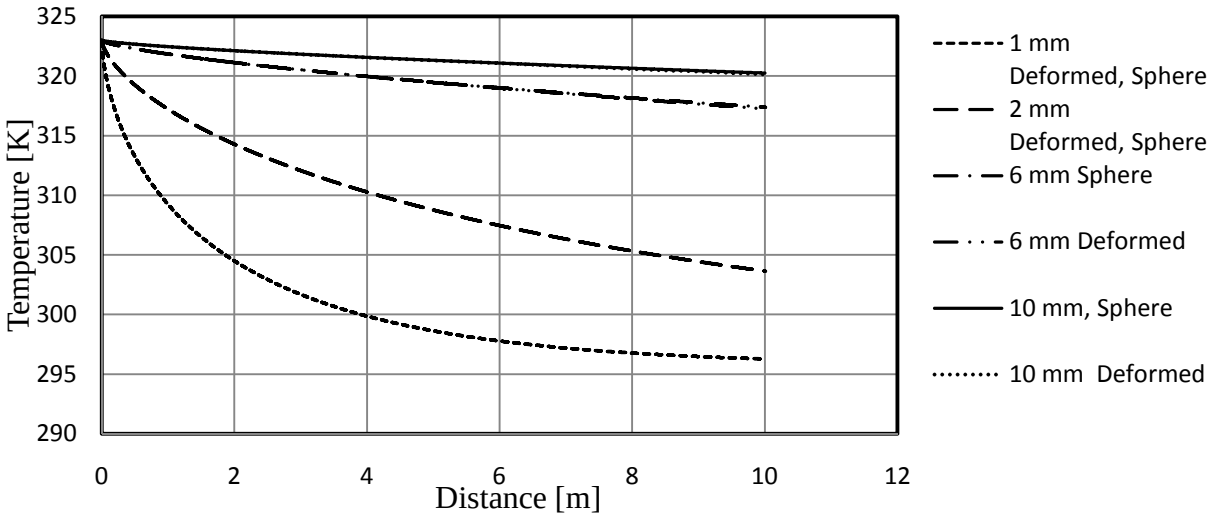

Figure 3.5 : Cooling of drops

In figure 3.6 the Merkel transfer characteristic, as determined with the Lagrangian model of this chapter, for different drop sizes in counter flowing, cross flowing and still air are compared. The fall height (H_{rz}) in each case is 2 m and the air side temperature and humidity changes are ignored.

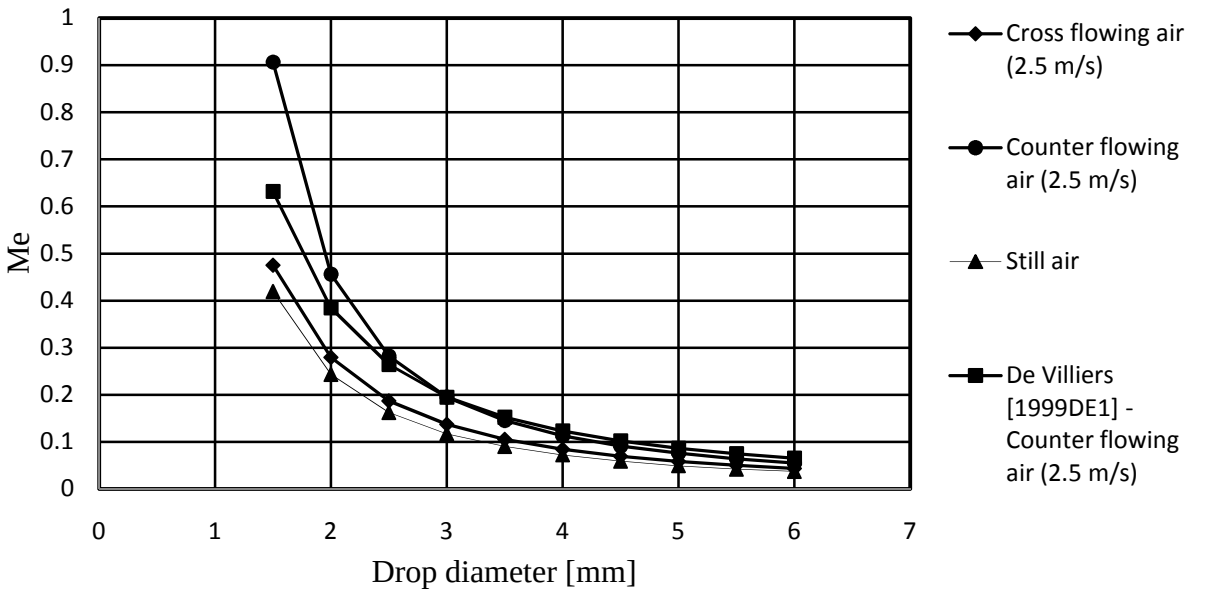

Figure 3.6 : Transfer characteristics for different flow configurations

The De Villiers [1999DE1] correlation for counter flow Merkel number used in figure 3.6 is given by the following equations

$$\frac{h_d A}{m_w} = 3.6\left(\frac{D}{v_i d_d}\right)\left(\frac{H_i}{d_d}\right)\left(\frac{p_a}{R_v T_a}/\rho_w\right) Sc^{0.33}\left[ln\left(\frac{w_{sw}+0.622}{w+0.622}\right)/(w_{sw}-w)\right] \times [5.01134 a_\rho \rho_a - 192121.7 a_\mu \mu_a - 2.57724 + 23.61842 \times (0.2539(0.15 a_v v_i)^{1.67} + 0.18)(0.83667(a_L H_i)^{-0.5299} + 0.42) \times (43.0696(a_L d_d)^{0.7947} + 0.52)] \quad (3.32)$$

where

$$a_\mu = 3.061 \times 10^{-6}\left[\frac{{\rho_w}^4 g^9}{\sigma_w}\right]^{0.25} \quad (3.33a)$$

$$a_\rho = \frac{998}{\rho_w} \quad (3.33b)$$

$$a_v = 73.298\left[\frac{g^5 {\sigma_w}^3}{{\rho_w}^3}\right]^{0.25} \quad (3.33c)$$

$$a_L = 6.122\left[\frac{g\sigma_w}{\rho_w}\right]^{0.25} \tag{3.32d}$$

Equation (3.31) is valid for $1\ \mathrm{m/s} \leq v_i \leq 5\ \mathrm{m/s}$ and $0.5\ \mathrm{m} \leq H_i \leq 5.5\ \mathrm{m}$ and $2\ \mathrm{mm} \leq d_d \leq 8\ \mathrm{mm}$

4

MODELLING OF DROP SIZE REDUCTION BY MEANS OF SLATS

4.1 Introduction

In this chapter the mathematical model used to predict the drop size reduction obtained by installing a grid of horizontal evenly spaced slats in a rain zone is presented. This model is used for grid design and provides valuable insight into the different mechanisms associated with drop impingement on slats resulting in drop break-up. The first part of the chapter looks at the basic theory applicable to drop break-up over narrow slats involving splashing, cutting and dripping from below the slat [1994DR1]. The drop size distributions associated with each of the break-up modes are discussed and a new correlation is proposed for the distribution of drops formed by cutting. The results from the model are compared to measured data and finally a correlation for the reduction in Sauter mean diameter for drops falling through a slat grid is proposed.

4.2 Theory

4.2.1 Splashing

When water splashes from a surface covered by a thin layer of liquid, the sequence of events can be described as follows: a thin film of liquid called the crown is thrown upwards; jets form at the upper rim of the crown as the crown becomes unstable; these jets break up into many small fragments that are ejected at high velocities [1971LE1]. Stow and Steiner [1977ST1] concluded that there are a number of variables that influence the consequences of a splashing event namely: the impact velocity, the roughness and curvature of the target and the extent to which the target is covered by a liquid layer. Levin and Hobbs [1971LE1] used high speed photographic techniques to observe splashing and reported that there is no observable difference in the splashing on a dry surface and a surface covered by a 0.5 mm thick liquid layer. There was however a difference in the time scale associated with the collapsing of the crown.

When a drop impacts on a narrow slat, a fraction of the drop splashes sideways [1988YA2] while the remaining water leaves the slat as cut drops or drops dripping from below the slat. The mass fraction of the original drop of water that splashes away from a slat is defined as the splash fraction. This fraction is simply the mass of fluid contained in the splash drops over the mass of the original incoming drop falling on the surface expressed as

$$f_s = \frac{M_s}{M_i} \tag{4.1}$$

Dreyer [1994DR1] proposes an empirical relation for the average splash fraction of a drop falling on a narrow slat covered with a thin layer of water. The constants for equation (4.2) are given in table 4.1.

$$\bar{f}_s = 0.01\left(c_1 + c_2\left(\frac{\delta}{W}\right)\right)\left(c_3 + c_4\left(\left(\frac{We}{We_{ref}}\right)\left(\frac{d_i}{W}\right)^2\right)^{c_5}\right)\left(c_6 + c_7\left(\frac{d_i}{W}\right)^{c_8}\right) \tag{4.2}$$

where

$$We = \frac{\rho_d v^2 d_i}{\sigma} \tag{4.3}$$

Table 4.1 : Constants for Equation (4.2)

Constant	10 mm slat	5 mm slat	2 mm slat
C_1	4.882	6.613	10.737
C_2	22.930	8.200	6.805
C_3	-2.301	-12.550	-12.996
C_4	3.242	13.700	14.766
C_5	5.327E-02	1.628E-02	3.578E-02
C_6	8.061	5.506E-01	1.210E-01
C_7	2.598	12.551	15.575
C_8	-2.977	-1.792	-2.148

We_{ref} is the Weber number for the largest stable drop, falling at terminal velocity. The Weber number is the ratio of the disruptive hydrodynamic force to the stabilizing surface tension forces in a free falling drop [1994DR1]. The largest stable drop diameter can be expressed by

$$d_m = \sqrt{\frac{16\sigma}{g(\rho_d - \rho_{av})}} \tag{4.4}$$

The cumulative mass distribution of the drops that are formed by splashing can be described by the following Rosin Rammler equation.

$$R(d) = 1 - exp\left(-\left(\frac{d}{d_{RR}}\right)^{n_{RR}}\right) \tag{4.5}$$

where

$$d_{RR} = d_{50}\left(0.6931^{-\left(\frac{1}{n_{RR}}\right)}\right) \tag{4.6}$$

The spread parameter was correlated by Dreyer [1994DR1] and is given by

$$n_{RR} = \left(24.532 - 75.174\left(\frac{\delta}{d_i}\right)\left(\frac{We_i}{We_{ref}}\right)^{0.74}\right) \times \left(0.149 + 6.801 \cdot 10^{-4}\left(\frac{KE}{KE_{ref}}\right)^{-0.76}\right) \tag{4.7}$$

KE_{ref} is the reference kinetic energy defined as

$$KE_{ref} = 0.5\left(\frac{\rho_d \pi {d_m}^3}{6}\right){v_T}^2 \tag{4.8}$$

The mass median diameter to maximum stable drop diameter ratio, as correlated by Dreyer [1994DR1] is given by

$$\left(\frac{d_{50}}{d_m}\right) = 3.08 \cdot 10^{-2} + \left(-0.163 + 4.560 \cdot 10^{-2}\left(\frac{\delta}{d_m}\right)^{-0.34}\right) \left(-0.804 - 0.619\left(\frac{We_i}{We_{ref}}\right)^{-0.27}\right)\left(-1.738 + 1.980\left(\frac{\delta}{d_i}\right)^{-0.17}\right) \tag{4.9}$$

Dreyer [1994DR1] also determined the following equation for the mean water film thickness on a slat for different conditions

$$\bar{\delta} = 0.315 - 1.387 \cdot 10^{-2} G_w - 2.550 \cdot 10^{-3} v_a + 1.575 \cdot 10^{-2} W - 3.992 \cdot 10^{-4} W^2 + 1.916 \cdot 10^{-3}(G_w W) + 2.188 \cdot 10^{-3}(v_a W) \tag{4.10}$$

4.2.2 Cutting

When a drop impacts on a slat that is narrower than its diameter, the drop break-up is a combination of splashing and cutting. Cutting is when a part of the drop, normally the part not directly over the slat, is cut off from the impacting drop by the sharp edge of the slat. The mass fraction of water that leaves a slat in the form of cut drops can be defined by a cutting fraction. This fraction is simply the mass of the drops that form due to cutting, divided by the mass of the original drop expressed as

$$f_c = \frac{M_c}{M_i} \tag{4.11}$$

The cutting of drops by a slat is shown in figure 4.1. The rest of the water splashes or drips from below the slat.

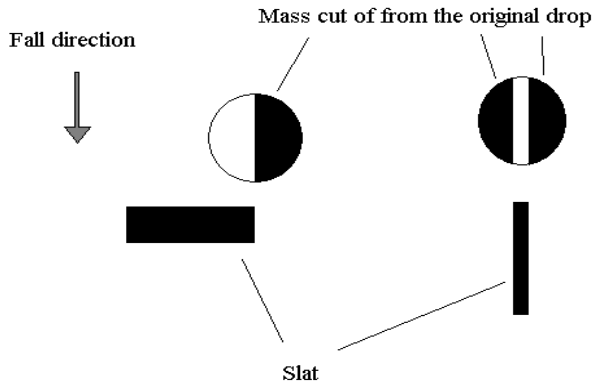

Figure 4.1 : Cutting of a drop on a slat

The average cutting fraction of drops impacting a slat is the average fraction of the mass cut off by a sharp edged slat of width W, if a drop of diameter d_i impacts the slat at every position between $-(W+ d_i)/2$ and $(W+ d_i)/2$. The average cutting fraction is given by the following equation by Dreyer [1994DR1]:

$$\overline{f_c} = \frac{\left(\int_{-(W+ d_i)/2}^{(W+ d_i)/2} f_c(x)\partial x\right)}{W + d_i} = \frac{d_i}{W + d_i} \tag{4.12}$$

Figure 4.2 shows average cutting fraction against drop diameter for different slat widths.

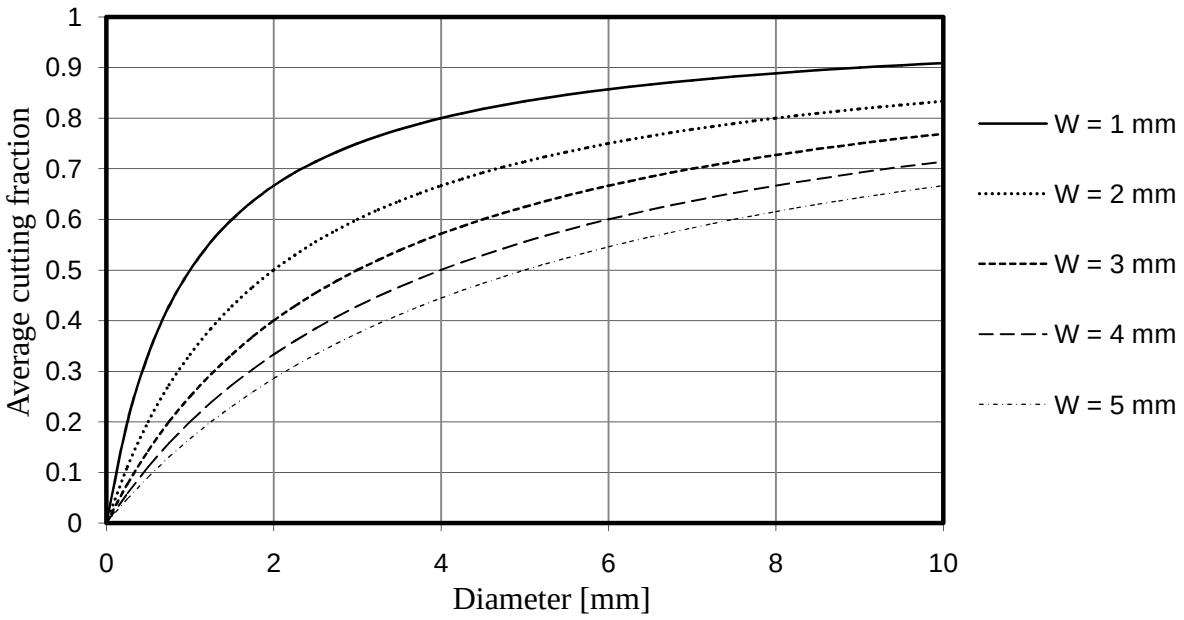

Figure 4.2 : Average cutting fraction for different slat widths

If it is assumed that the part of the drop that is cut from the original drop is not directly over the slat, the mass of the cut drops can be calculated by

$$M_c = \rho_d \left[\frac{\pi b^2}{3}\left(\frac{3d_i}{2} - b\right)\right] \tag{4.13}$$

where

$$b = \left(\frac{2x - W}{2}\right) + \left(\frac{d_i}{2}\right) \tag{4.14}$$

Figure 4.3 illustrates the variables used in equations (4.13) and (4.14).

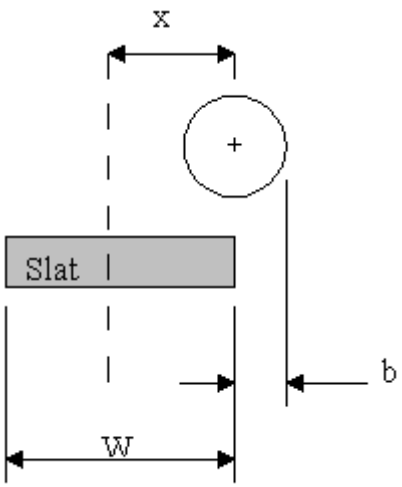

Figure 4.3 : Variables of equation 4.13 and 4.14

Dreyer [1994DR1] suggests that the average mass of drops that form, due to cutting of a drop impacting a slat between x=0 and x = (W + d_i)/2 can be calculated with equation (4.13), by simply replacing b with the following average relations.

$$b_{Aavg} = \left(\frac{3d_i}{4}\right) - \left(\frac{W}{4}\right) \tag{4.15}$$

$$b_{Bavg} = \left(\frac{d_i}{4}\right) - \left(\frac{W}{4}\right) \tag{4.16}$$

Another way of representing the mass distribution is suggested for the purposes of modelling the splash grid by the author of this thesis. Rather than representing the mass distribution of the drops impacting a slat between x = 0 and x = (W + d_i)/2 as two drops of an average size, the cumulative mass distribution as shown by the following equation is suggested.

$$\begin{aligned} R\left(\frac{d}{d_i}\right) = {} & 0.498216\left(\frac{d}{d_i}\right)^6 + 0.246347\left(\frac{d}{d_i}\right)^5 + 0.039492\left(\frac{d}{d_i}\right)^4 \\ & - 0.061091\left(\frac{d}{d_i}\right)^3 - 0.010561\left(\frac{d}{d_i}\right)^2 + 0.028724\left(\frac{d}{d_i}\right) \\ & - 0.003663 \end{aligned} \tag{4.17}$$

Figure 4.4 shows a drop impacting on a narrow slat. Equation (4.17) is obtained by looking at the mass distribution of the drops formed by cutting, when a drop impacts a slat between x = 0 and x = (W + d_i)/2 in 200 increments. For each increment the mass of the drop not directly over the slat on both sides of the slat is determined with equation (4.13) by substituting b with b_A and b_B given by equations (4.18) and (4.19). The assumption is made that the two new drops are spherical and the diameter of both drops are determined from the two masses. When the drops formed by cutting at all the increments are determined, their cumulative mass distribution is plotted and the curve of equation (4.17) is obtained. Figure 4.5 shows the cutting mass distribution for 5 mm drops impacting a 3 mm slat from x = 0 to x = (W + d_i)/2 in 200 increments and the cutting mass distribution predicted by equation (4.17).

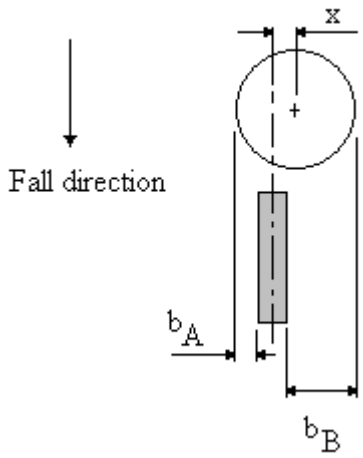

Figure 4.4 : Drop impacting on a slat

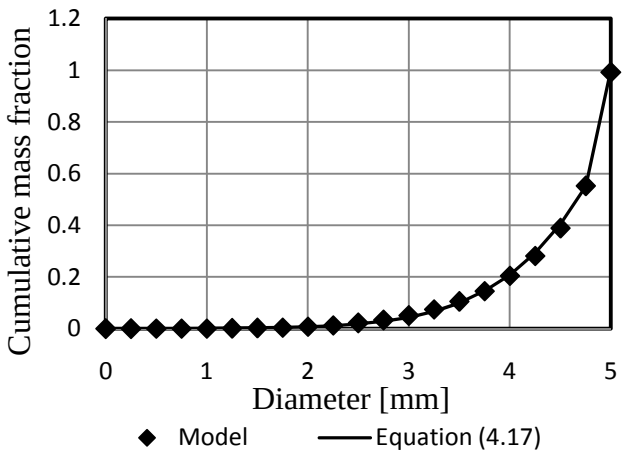

Figure 4. 5 : Cutting mass distribution (d_i = 5 mm, W = 3 mm)

The variables b_A and b_B in figure 4.4 are expressed by

$$b_A = (d_i - W)/2 - x \tag{4.18}$$

$$b_B = (d_i - W)/2 + x \tag{4.19}$$

4.2.3 Dripping

Dripping is when drops hang from below a slat and drip down due to gravity. The size distribution of the drops that form because of dripping is influenced by the geometry of the slat.

According to Yung [1980YU1] dripping occurs when large primary drops form at fixed points below the slats due to water running down the side of the slats. Every primary drop that drips from the slat is followed by a number of smaller, satellite drops. Dreyer [1994DR1] established that the sizes of the primary drops could be linked to a shape factor for the specific geometry. The shape factor is defined by equation (4.20) and depicted by figure 4.6.

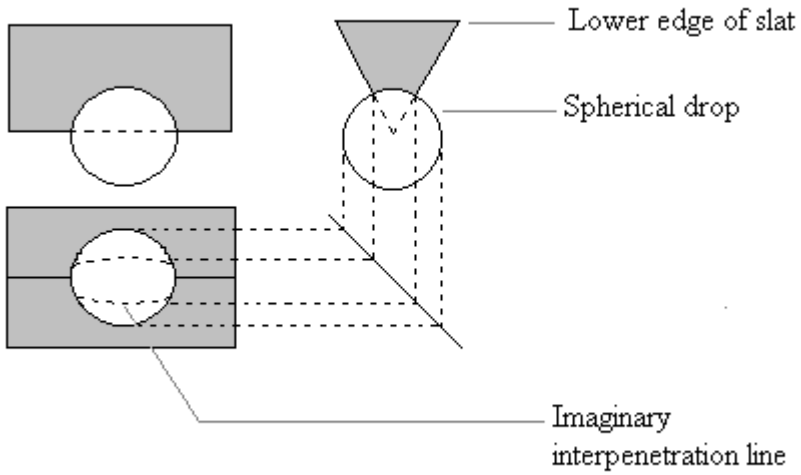

Figure 4.6 : Schematic representation of the shape factor

S = Circumference of interpenetration line on slat / Circumference of sphere (4.20)

The primary drop size that drips from the bottom of a slat can be expressed as

$$d_p = C\sqrt{\frac{\sigma}{g(\rho_d - \rho_{av})}} \tag{4.21}$$

The non-dimensional drop size is calculated using equation (4.22) and is a function of the shape factor.

$$C = 2.206 + \left(\frac{0.0597}{1.1 - S}\right) \tag{4.22}$$

It can be noted that the shape factor (S), for a large horizontal surface equals 1 and that of a thin horizontal slat equals more or less $2/\pi$. For the purpose of modelling the slat grid, the shape factor can be taken as $2/\pi$ because 3 mm slats are used.

The size of the primary drop dripping from below a 3 mm slat is normally about of 6 - 7 mm as confirmed by Dreyer [1994DR1]. This can become a problem when multiple layers of the slat grid are inserted in the rain zone to try and achieve better drop break-up. With multiple layers the dripping becomes more dominant because of the increased overall slat length from where the dripping can take place. The Sauter mean diameter below the multiple layers can thus be even larger than that of a single layer.

The sizes of the drops that drip from below a slat can be decreased by changing the profile of the slat bottom as shown in table 4.2 for 3 mm wide slats. Tests are done in which the profile of the bottom surface of the slat is varied to determine the reduction in primary drop size. The tests are done with the experimental rig described in Appendix D.

Table 4.2 : PVC slat profiles (3 mm wide) for Γ = 0.078 kg/ms with primary drop sizes

Slat	Profile	d_p [mm]
A		6.88
B	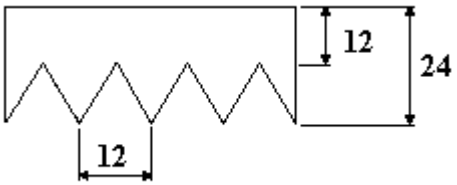	5.13
C	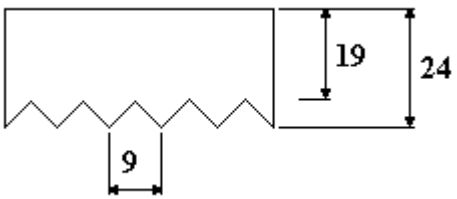	5.42

Table 4.2 *(Continued)*

Slat	Profile	d_p [mm]
D	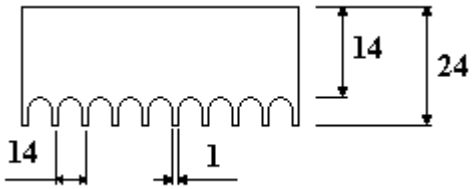	4.63
E	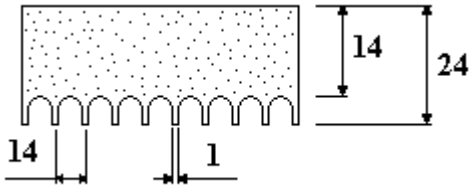 *(Sandblasted)*	5.35
F	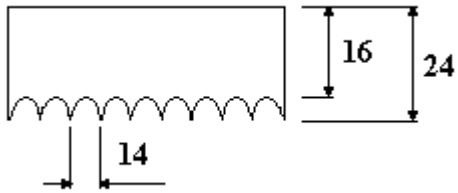 *(Sharpened over the slat length)*	4.01
G	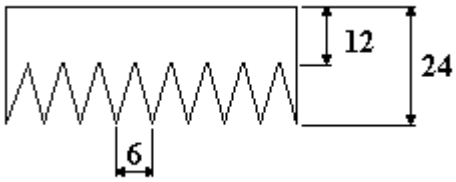	6.30
H	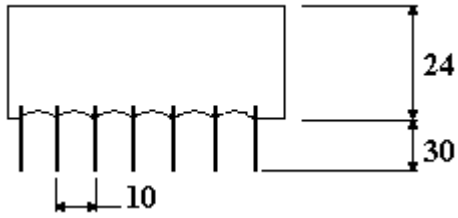 *(Embedded fins)*	5.38

4.3 Solution procedure

In order to model the drop break-up, the initial cumulative mass distribution of the drops above the grid must be known. To simplify the calculations drops are allocated to different parcels. A parcel in this case, is a group of drops of which the diameters do not vary by more than 0.25 mm. All the drops in the parcel are given the mean diameter value of the parcel.

The average splash fraction for each parcel can be determined from equation (4.2) and the drop distribution of the splash drops that are formed due to splashing can be determined from equation (4.5).

The average cutting fraction of each parcel can be determined from equation (4.12) and the distribution of the drops formed by cutting can be determined from equation (4.17).

The combined cutting and splashing cumulative mass distribution are determined by summating the number of drops in the splashing and cutting parcels that represents the same diameter, and then calculating the cumulative mass distribution.

The mass flow rate of the drops dripping from below the slats can be determined by doing a mass balance which is discussed later in this section. Equation (4.21) is now used to determine the diameter of the primary drop dripping from below a slat. For every primary drop there are five satellite drops and their sizes vary linearly between $0.24d_p$ and $0.46d_p$.

4.3.1 Initial drop distribution

The initial drop distribution entering the rain zone must be provided as an input to the model. Distributions were measured for different air and water flow combinations under different types of fill material and the results are presented and discussed in chapter 2.

4.3.2 Drop drag models

The drag model (equation 3.12) which takes drop deformation into account is used to model the drop drag. The dynamic behaviour of a deforming drop and that of a sphere of the same density and size are similar when falling at lower speeds. At higher speeds however they deviate, ultimately projecting significantly different terminal velocities.

4.3.3 Drop-drop collisions

As the drops travel between the fill and the slat grid, the larger drops fall faster than the smaller ones which could result in possible collisions between larger and smaller drops. After collision the two drops can bounce away from each other, coalesce permanently or coalesce temporarily and then bounce away from each other again. Dreyer [1994DR1] reported that the effect of drop collisions on the transfer characteristics and pressure drop were negligible in the sensitivity analysis of his model, so this will be ignored for this simplified model.

4.3.4 Film thickness on the slats

The average film thickness is calculated using equation (4.10). It is assumed that the water film is always completely formed on the slats.

4.3.5 Drop break-up

When drops fall on the slat grid, some of the drops will impact on the slats causing them to break up and others will pass through the grid unhindered. The way that this is determined is by determining the effective break area of the slats. If drops of diameter $d_{i,}$ impacts on a slat of width W and length L the effective break area of the slat can be calculated from

$$A_{bi} = L(W + d_i) \tag{4.23}$$

The number of drops of a specific size that fall on the slats of a splash grid that contains N_s slats can then be calculated from

$$N_{bi} = N_i \left(\frac{N_s L(W + d_i)}{A_{fr}} \right) \tag{4.24}$$

where

N_i = Total number of incoming drops of a specific diameter d_i

A_{fr} = Total cross-sectional frontal area

4.3.6 Splash model

The splash model as described in section 4.2.1 is used to model the splashing of drops on the slats of the slat grid. Firstly the total mass of drops of a specific drop diameter that impacts the slats is multiplied by the average splash fraction associated with the same drop diameter. Secondly the Rosin Rammler curve (equation 4.5) is used to determine the distribution of the splash drops.

4.3.7 Cutting model

The cutting distribution is determined by again multiplying the total mass of a specific size drop falling on the slats, by the average cutting fraction associated with the same diameter. The distribution of this mass is then determined by using the distribution given by equation (4.17).

4.3.8 Dripping model

The average dripping mass is determined by means of a mass balance over the slat grid to determine the mass of water dripping from the slats. The total incoming mass that impacts on the slats must be equal to the mass of water leaving the slats due to cutting, splashing and dripping. This can be expressed as

$$m_d = \sum_j \left(m_w N_s L\left(W + d_{i,j}\right)\right) - \sum_j \left(\overline{f_{s,j}} m_w N_s L\left(W + d_{i,j}\right)\right) - \sum_j \left(\overline{f_{c,j}} m_w N_s L\left(W + d_{i,j}\right)\right) \tag{4.25}$$

4.3.9 Upward flowing drops

When the counter flow air velocity becomes bigger than a drop's terminal velocity the drop will move in the direction of the air stream and it is assumed they never reach the splash grid. The mass of these drops are then simply subtracted from the incoming mass to the slat grid and ignored in further distribution calculations.

4.3.10 Modelling drops in parcels

Because there are too many different drop sizes present in a distribution, drops are grouped in parcels.

4.4 Results

In order to validate the model developed in this chapter, it must be proven that the model follows the same trends as the measured data and that the numerical values obtained from the model are comparable to measured data. Figure 4.7 shows the cumulative mass distribution obtained for a single water flow rate with different air flow rates as predicted by the model. The Sauter mean diameters for the distributions of figure 4.7 are shown in figure 4.8. In these results the spacing between the slat grid and the fill (H_{fg}) is kept at 0.6 m.

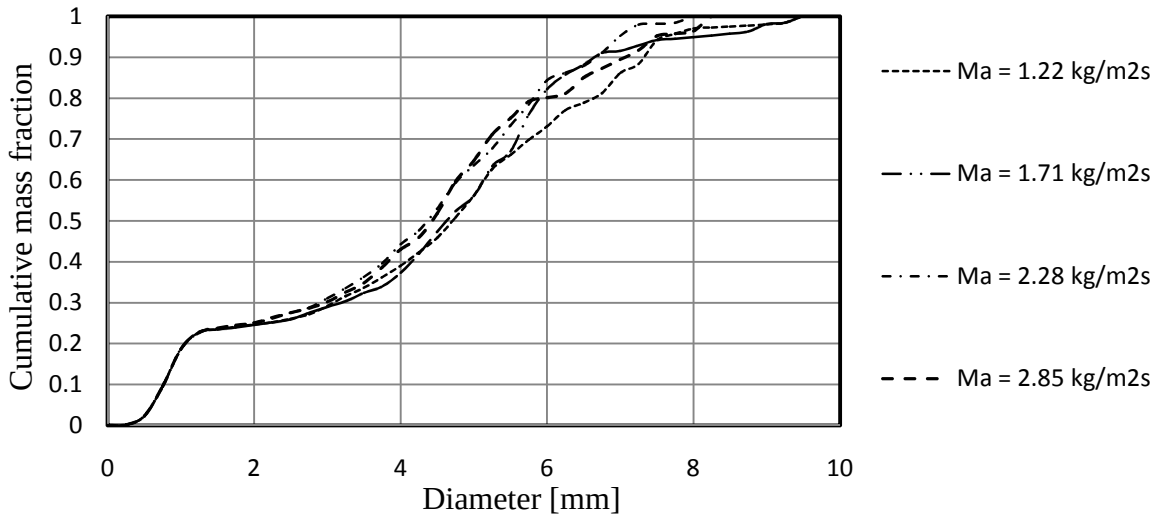

Figure 4.7 : Predicted cumulative mass distributions below slat grid for G_w = 2.84 kg/m^{2}s, H_{fg} = 0.6 m

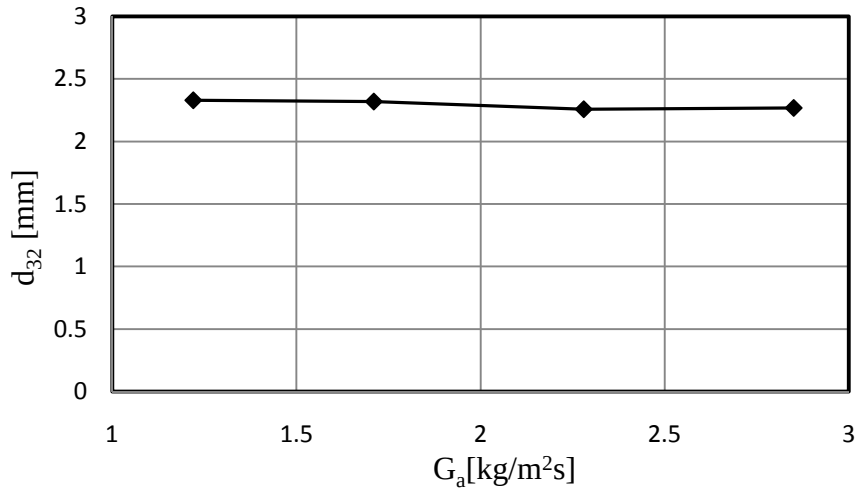

Figure 4.8 : Predicted Sauter mean diameters below slat grid for G_w = 2.84kg/m^{2}s, H_{fg} = 0.6 m

The input cumulative mass distributions used to predict the results shown in figures 4.7 and 4.8 are the mass distribution measured 260 mm below the trickle fill for the corresponding air and water flow rate combination as provided in chapter 2. With this approach the predicted

Sauter mean diameter below the grid seems to stay relatively constant with an increasing air mass flow rate.

The cumulative mass distribution of the drops measured immediately below the trickle fill for a water mass flow rate of 2.84 kg/m^{2}s with no air flow can be seen in figure 4.10. This is the input distribution used in the model for all further modelled results obtained in this section except where stated otherwise.

Figure 4.9 shows a comparison between the Sauter mean diameters measured immediately below one layer of slat grid with different fill-grid spacings and the values predicted by the model. In each case the cumulative mass distribution of figure 4.10 is used as an input to predict the Sauter mean diameter directly below the slat grid.

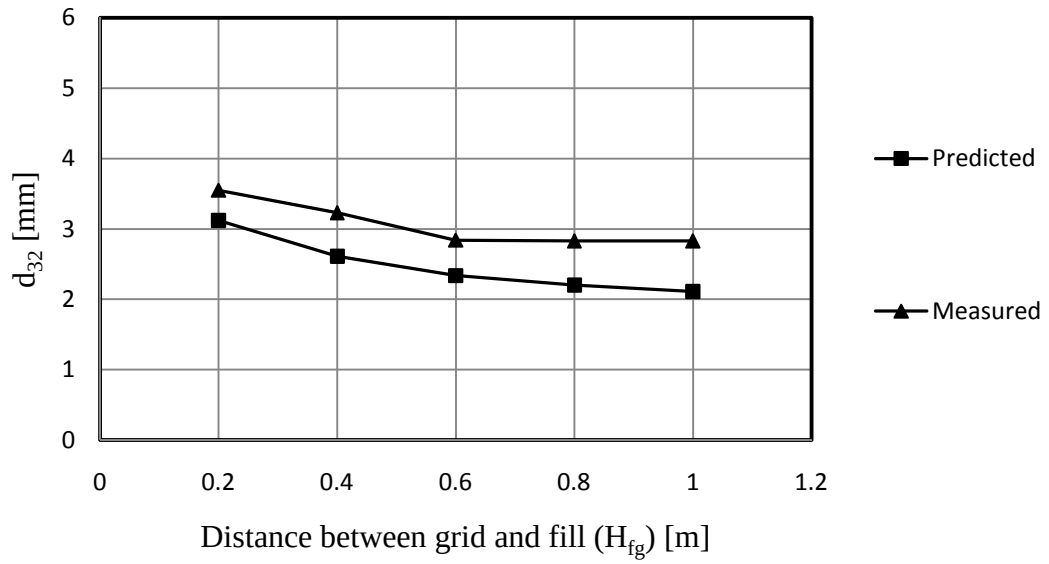

Figure 4.9 : Measured and predicted Sauter means below one layer of slat grid, G_w = 2.84 kg/m^{2}s, no air

Figure 4.10 also shows a comparison between the measured and predicted mass distribution below a single layer of the designed slat grid.

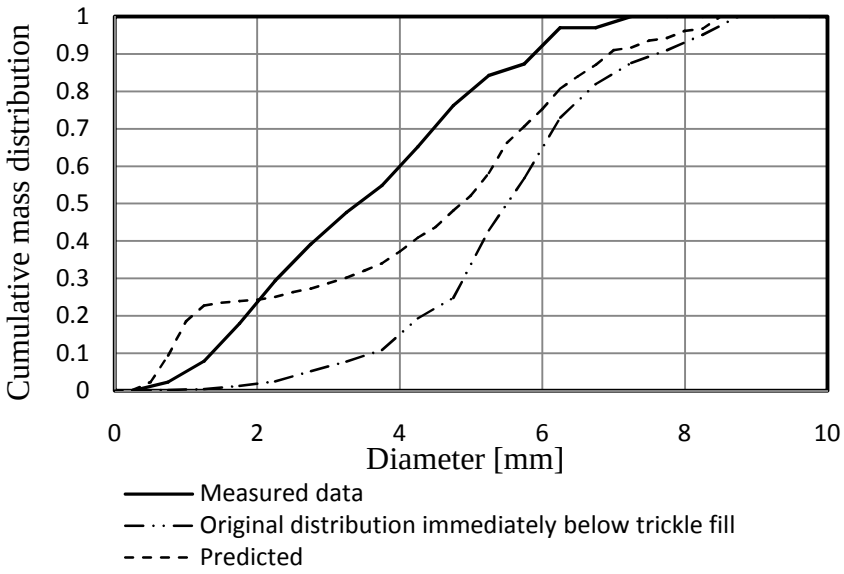

Figure 4.10 : Measured and predicted mass distribution, G_w = 2.84 kg/m^{2}s, no air, H_{fg} = 0.6 m

The model is used to conduct a sensitivity analysis to determine the influence of each variable on the drop size reduction of the slat grid. A correlation is proposed by the author for the drop size reduction of a slat grid and is given by

$$\frac{d_{32,o}}{d_{32,i}} = 0.22042\left({H_{fg}}^{-0.24636}\right)\left(W^{-0.24190}\right)\left(S^{0.41311}\right)e^{[0.02993G_a - 0.03097G_w]} \tag{4.26}$$

Figures 4.11 to 4.13 show the results of the sensitivity analysis together with the results predicted by equation (4.26). All the results are obtained for G_w = 2.84 kg/m^{2}s and no air flow.

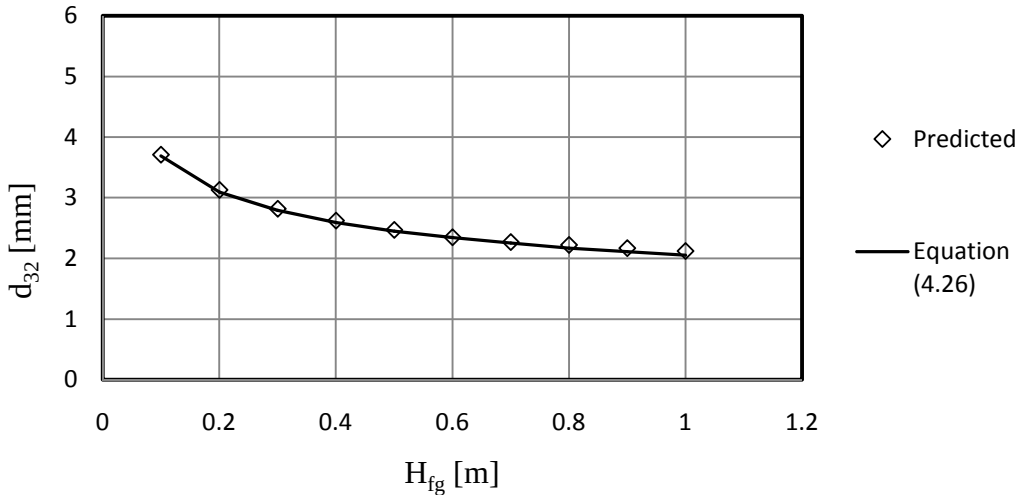

Figure 4.11 : Effect of distance below the fill on the Sauter mean diameter, S = 10 mm, W = 3mm

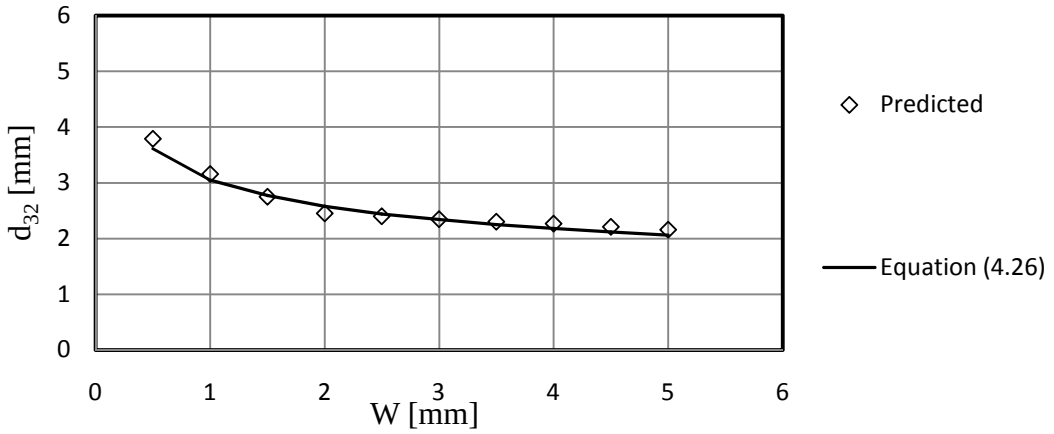

Figure 4.12 : Effect of slat width on the Sauter mean diameter, H_{fg} = 0.6 m, S = 10 mm

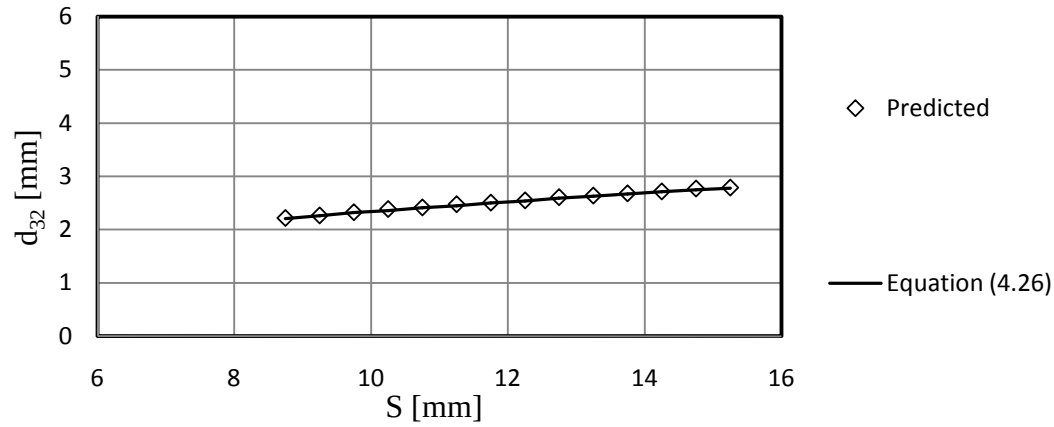

Figure 4.13 : Effect of spacing between the slats on Sauter mean diameter, W = 3 mm, H_{fg} = 0.6 m

Figure 4.14 shows the results obtained for a single layer of the slat grid with different slat profiles on the bottom of the slat. The profiles of slat A and slat F, as shown in table 4.2, are compared for different fill-grid spacings.

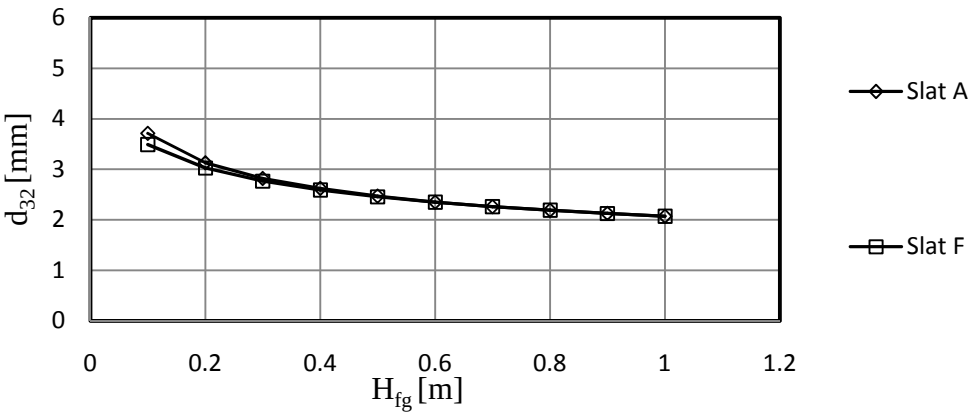

Figure 4.14 : Comparison between the bottom profiles of slats, G_w = 2.84 kg/m^{2}s, No air

In figure 4.15, equation (4.26) is used to predict the Sauter mean diameters immediately below one layer of slat grid for the same conditions as in figure 4.8. The results of the equations are compared to the results of figure 4.8 that is obtained with the model. The inlet Sauter means are the measured results immediately below a trickle fill for the applicable flow condition as provided in chapter 2.

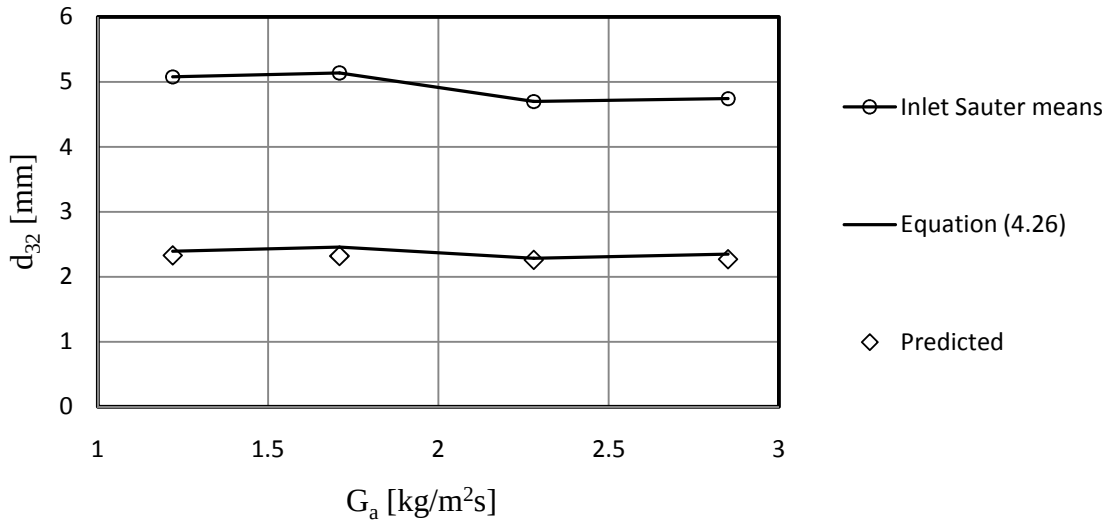

Figure 4.15 : Predicted Sauter mean diameters below one layer of slat grid, G_w = 2.84 kg/m^{2}s

A sample calculation for the break-up model is provided in Appendix I.

4.5 Discussion and recommendations

Although the simplified model isn't very accurate in predicting the drop distribution (figure 4.10) below a slat grid, it provides valuable insight into trends associated with the change of the different variables and serves as a handy design tool.

Figure 4.8 shows that the model follows the expected trend when the air mass flow is increased and the Sauter mean diameter stay relatively constant. This relationship between the Sauter mean and the air-water mass flow ratio is also seen in Oosthuizen's [1995OO1] measurements below a coarse expanded metal grid.

Figure 4.9 shows that the predicted Sauter mean diameter compares favourably with the experimental results, following the same trend with increasing distance between the grid and the fill. The model tends to under predict the Sauter mean diameter by around 15 % up to a

fill-grid distance of 0.6 m from where the deviation between the measured and predicted Sauter means start to increase because of the fact that the measured Sauter means stay constant. It can be seen from the measured data provided in figure 2.31 that the Sauter mean either becomes constant or increases again for a grid-fill spacing of larger than 0.6 m. Oosthuizen [1995OO1] also found that the Sauter mean diameter below a coarse expanded metal grid started increasing again at a fill-grid spacing of 0.67 m. Fill-grid spacing beyond 0.6 m are therefore assumed unimportant in terms of modelling.

The under prediction in Sauter mean comes from the way in which splashing is treated in the model. The simplifying assumption is made that drop interaction of any kind can be ignored. However, when a drop impacts on a slat in the rain zone of a wet-cooling tower the splash drops leave the slat at a certain trajectory after which three things can happen: the splash drops fall through the grid; upward moving splash drops coalesce with other falling drops; the splash drops impact on the same slat or on other slats, but do not cause any splashing because of their low kinetic energy and become part of the water film present on the slats. This means that many of the originally formed splash drops, generally smaller than 1.5 mm in diameter, are not present in the measurements because of their interaction with other falling drops. The measured Sauter mean diameter is therefore larger than the predicted one because of the absence of many of the smaller drops predicted by the model.

From the sensitivity analysis of the model an important observation can be made in terms of the optimum slat width for a slat grid like the one used in this thesis. It can be seen from figure 4.12 that slat widths greater than 3 mm do not significantly reduce the Sauter mean diameter anymore. When one looks at the loss coefficients for grids with sharp edged slats, one can see that the loss coefficient doubles from 3 mm to 5 mm slats. This can be seen in Appendix C. The assumption can then be made that a 3 mm slat is the optimum slat width.

Lastly the model shows that the spacing between the fill and the grid has a strong influence on drop size reduction up to the region between 0.6 m and 0.8 m.

5

MODELLING OF CROSS FLOW RAIN ZONE PERFORMANCE

5.1 Introduction

In counter flow natural draught wet-cooling towers, air entering the cooling tower moves in cross flow to the water whereas closer to the centre of the tower the air is virtually in counter flow.

This chapter looks at 4 different methods of analysis for modelling rain zone performance characteristic in cross flow configuration, namely Lagrangian, Poppe, Merkel and effectiveness-NTU (*e*-NTU). The data used for this investigation is obtained from CFD simulations based on the two distributions shown in table 5.1. Distribution A is measured below two layers of the designed grid (H_{fg} = 0.8 m, G_w = 2.84 kg/m^{2}s, no air) and distribution B is measured 260 mm below a trickle fill (G_w = 2.84 kg/m^{2}s, no air). Each distribution is modelled as a polydisperse distribution according to the Rosin Rammler parameters provided in table 5.1, a monodisperse distribution according to the Sauter mean diameter and the exact polydisperse distribution as measured in chapter 2. The measurement data are presented in chapter 2 and provided in Appendix G.

Table 5.1 : Input drop distributions for CFD analysis

Distribution	Minimum diameter [mm]	Maximum diameter [mm]	Mean diameter [mm]	Spread parameter [-]	d_{32} [mm]
A	0.75	7.75	3.971	1.555	2.73
B	0.25	8.75	5.948	4.1327	5.19

The main method for determining cooling tower performance is the Merkel method which is generally used to evaluate fill materials. Merkel's [1925ME1] theory for the evaluation of cooling towers relies on three important assumptions which are:

- The Lewis factor equals unity
- The air leaving the tower is saturated

- The water that evaporates is neglected in the energy balance

Poppe and Rögener [1991PO1] developed the Poppe model and do not make the simplifications of the Merkel method. They use a correlation (equation 5.5) by Bosnjakovic [1965BO1] to determine the Lewis factor. The Poppe and Merkel methods are solved iteratively and a solution is converged when the predicted outlet water temperature equals the measured temperatures or equals the outlet temperature predicted with CFD, as is the case in this chapter.

Jaber and Webb [1989JA1] developed the equations necessary to apply the effectiveness-NTU method directly to counter flow and cross flow cooling towers.

Marseilles et. al. [1990MA1] suggested that the assumption of the liquid surface temperature being equal to the bulk fluid temperature can lead to an over-prediction in the system performance at high inlet water temperatures. This means that no resistance to heat transfer is assumed on the liquid side. However from Marseilles's work the effect of film resistance only became significant for water inlet temperatures higher than 50 °C. Natural draught cooling towers usually operate at inlet water temperatures of up to 60 °C, while air cooled heat exchangers are generally used when the process fluid temperature exceeds 60 °C [2006VI1].

Kloppers [2005KL2] compared the Poppe, Merkel and e-NTU methods for determining the performances of a natural draught cooling tower. He concluded that the three methods predict almost the same water outlet temperature. The Merkel and e-NTU methods are expected to give identical results because the same simplifying assumptions are made for both these methods, but it can be seen from the analysis in section 5.4 that their Merkel numbers differ slightly.

Kloppers [2005KL2] shows that the Poppe method predicts higher heat rejection rates (Q) than the Merkel method because the Merkel method ignores the loss of water due to evaporation in the energy equation ($Q = m_w c_{pw}(T_{wi} - T_{wo})$). According to Grange [1994GR1] the Merkel method underestimates the evaporation water loss when compared to the Poppe method, but the difference in results decrease with increasing ambient temperatures.

The Lewis factor indicates the relative rate of convection heat transfer to evaporation and can range from 0.6 to 1.3 [2005KL2]. Higher Lewis numbers mean that more heat is rejected through convection by a direct system which leads to higher air outlet temperatures. It can also mean that less water is evaporating from the system. The definition of the Lewis factor can lead to different predicted outlet conditions, but these differences become unimportant when the ambient temperature is above approximately 26 °C [2005KL2].

5.2 Theoretical methods of analysis

Although the Merkel method is the main method for determining cooling tower performance, the Poppe method is discussed first in this section because of its completeness. The Merkel assumptions are then made and the differential equations in the Poppe section are reduced to the two Merkel equations. The *e*-NTU method is discussed and also rain zone pressure drop.

5.2.1 Poppe

By considering a control volume as shown in figure 5.1 for cross flow, the following differential equations for modelling the transfer characteristics can be derived as presented by Kloppers [2003KL1], [2004KR1]. This method does not make the simplifying assumptions of Merkel.

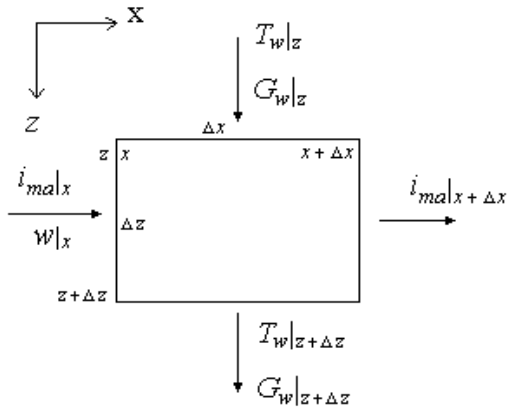

Figure 5.1 : Control volume for cross flow rain zone section

The temperature change of the water is given by

$$\frac{\partial T_w}{\partial z} = \frac{1}{c_{pw}} \frac{G_a}{G_w} \frac{h_d a_{fi}}{G_a} \left[\begin{matrix} (w_{sw} - w) c_{pw} T_w - (i_{masw} - i_{ma}) - \\ (Le_f - 1)[i_{masw} - i_{ma} - (w_{sw} - w) i_v] \end{matrix} \right] \quad (5.1)$$

Water evaporation rate is given by

$$\frac{\partial G_w}{\partial z} = -G_a \frac{h_d a_{fi}}{G_a} (w_{sw} - w) \tag{5.2}$$

As the cold air passes over the hot water the enthalpy of the air changes according to the following relation

$$\frac{\partial i_{ma}}{\partial x} = \frac{h_d a_{fi}}{G_a} \left[i_{masw} - i_{ma} + \left(Le_f - 1 \right) \{ i_{masw} - i_{ma} - i_v (w_{sw} - w) \} \right] \tag{5.3}$$

Because of the water that evaporates into the air stream the humidity of the air increases and the change can be modelled by

$$\frac{\partial w}{\partial x} = \frac{h_d a_{fi}}{G_a} (w_{sw} - w) \tag{5.4}$$

The Lewis factor in the differential equations above can be determined from the Bosnjakovic [1965BO1] relation expressed as

$$Le_f = 0.865^{\frac{2}{3}} \left[\frac{\left(\frac{w_{sw} + 0.622}{w + 0.622} \right) - 1}{ln \left(\frac{w_{sw} + 0.622}{w + 0.622} \right)} \right] \tag{5.5}$$

The differential equations for cross flow modelling can be solved by dividing the domain under consideration into a grid of cells, as shown in figure 5.2. The differential equations are then solved for each cell by employing the Eulerian numerical integration technique.

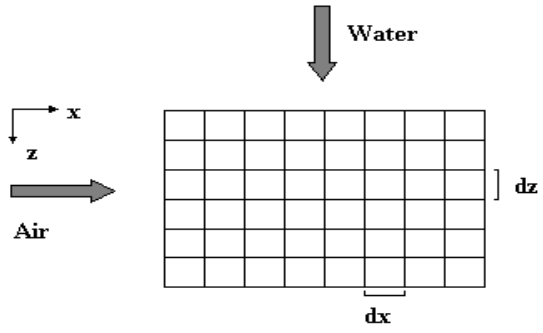

Figure 5.2 : Solution grid for cross flow model

The Merkel number is a dimensionless number that is used to describe the performance of a direct contact evaporative cooling system defined by equation (5.6). The Merkel number is determined by means of an iterative process where a value for the ratio $h_d a_{rz}/G_a$ is guessed in the above equations and then altered until the predicted outlet water temperature equals the measured water outlet temperature. The water side Merkel number at each grid point can then be determined from the following relation:

$$Me(i,j) = \frac{h_d a_{rz} H_{rz}}{G_{w(i,j)}} \tag{5.6}$$

The system Merkel number can now be determined by taking the average value of the Merkel numbers at every grid point. A sample calculation is provided in Appendix K.

5.2.2 Merkel

The Merkel method simplifies the Poppe method by assuming that the evaporative loss is negligible (dw = 0) and the Lewis factor equals unity. This means that equations (5.1) to (5.4) reduce to the following two equations

$$\frac{\partial i_{ma}}{\partial x} = \frac{h_d a_{fi}}{G_a}[i_{masw} - i_{ma}] \tag{5.7}$$

$$\frac{\partial T_w}{\partial z} = -\frac{1}{c_{pw}} \frac{G_a}{G_w} \frac{\partial i_{ma}}{\partial x} \tag{5.8}$$

The same technique as in the previous section is used for determining the Merkel number according to the Merkel method.

5.2.3 e-NTU

The e-NTU method is normally a method used to determine the performance of heat exchangers but can also be used to determine the Merkel performance characteristic of a cross flow rain zone. The applicable equations for a cooling tower were developed by Jaber and

Webb [1989JA1]. In order to determine the transfer characteristic, the effectiveness of the evaporative system must be determined and defined as

$$e_e = \frac{\mathrm{Q}}{\mathrm{Q_{max}}} \tag{5.9}$$

The cooling water side heat transfer rate can be given by

$$Q = m_w c_{pw}(T_{wi} - T_{wo}) \tag{5.10}$$

The first step in determining the value of Q_{max} is to determine the saturated air enthalpies at the inlet and outlet water temperatures respectively. This information is used to find the derivative of the enthalpy of saturated air with respect to water temperature, (di_{masw}/dT_w). After this ratio is determined the solution proceeds in one of two cases. Case 1 is shown by

Case 1:

$$(m_w\, c_{pw})/(di_{masw}/dT_w\,) < m_a \tag{5.11}$$

The minimum and maximum capacity rate for case 1 is given by

$$C_{emin} = m_w c_{pw}/(di_{masw}/dT_w) \tag{5.12}$$

$$C_{emax} = m_a \tag{5.13}$$

The evaporative capacity rate ratio can be given by

$$C_e = C_{emin}/C_{emax} = m_w c_{pw}/[(di_{masw}/dT_w)m_a] \tag{5.14}$$

Before finding Q_{max} a correction factor must be determined as given by

$$\lambda = (i_{maswo} + i_{maswi} - 2i_{masw})/4 \tag{5.15}$$

where i_{masw} is evaluated at the mean water temperature $T_{wm} = (T_{wi} + T_{wo})/2$.

Q_{max} can now be determined from

$$Q_{max} = C_{emin}(i_{maswi} - \lambda - i_{mai}) \tag{5.16}$$

The effectiveness of the cross flow evaporative cooler with unmixed streams can also be expressed in terms of NTU_e as given by

$$e_e = 1 - exp\left[NTU_e{}^{0.22}\{exp(-C_e NTU_e) - 1\}/C_e\right] \tag{5.17}$$

From equations (5.9) and (5.17) the NTU_e can be solved iteratively and the Merkel transfer characteristic can be obtained from the following relation

$$\frac{h_d a_{rz} H_{rz}}{G_w} = \frac{NTU_e c_{pwm}}{(di_{masw}/dT_w)} \tag{5.18}$$

NTU_e can be defined as follows:

$$NTU_e = h_d A(di_{masw}/dT_w)/\left(m_w c_{pw}\right) \tag{5.19}$$

where A is the total wetted transfer area.

The second case that must be considered is given by

Case 2:

$$m_a < m_w c_{pw}/(di_{masw}/dT_w) \tag{5.20}$$

The evaporative capacity rate ratio can be found by equation (5.21) and similar to case 1 the number of thermal units can be found by aid of equation (5.17)

$$C_e = m_a(di_{masw}/dT_w)/\left(m_w c_{pw}\right) \tag{5.21}$$

The Merkel transfer characteristic for case 2 is given by

$$\frac{h_d a_{rz} H_{rz}}{G_w} = m_a NTU_e / m_w \tag{5.22}$$

A sample calculation is provided in Appendix J.

5.2.4 Pressure drop

Smaller drops in a rain zone leads to an increased pressure drop in this region and therefore this increase in pressure needs to be quantified. The pressure drop over the cross flow rain zone under consideration in section 5.3 can be determined with the Lagrangian model of chapter 3 by summating the drag forces on all the drops present in the rain zone at different time steps over the fall height of the drops for different air and water flow combinations. For this calculation the air side changes are ignored and a monodisperse distribution is assumed. The total drag force on the drops is then divided by the inlet area of the rain zone to determine the pressure drop. This is given by

$$\Delta p_{rz} = \frac{1}{A_{fr}} \left(\sum_{i=1}^{l} \sum_{j=1}^{m} F_{D,i,j} \right) \tag{5.23}$$

where *l* indicates the number of time steps and *m* the number of drops per time step.

5.3 CFD

A CFD analysis is done for a cross flow rain zone under different air and water flow conditions for the drop distributions of table 5.1. Each distribution is modelled as a monodisperse as well as a polydisperse distribution. The water and air mass flow combination considered in the CFD analysis are the same as shown in table 2.1 except that in this case a cross flow arrangement is considered. The models used in the CFD analysis (Fluent) are provided in Appendix L.

Initial conditions used as input to the models are: T_{wi} = 323 K, T_a = 298 K , w = 0.01655 kg vapour/kg dry air and P_{atm} = 101325 Pa. The rain zone is modelled in 2D with a height and length of 2 m and 1.55 m respectively, which are the dimensions of the cross flow rain zone test facility at the University of Stellenbosch.

Figures 5.3 and 5.4 shows the water side CFD temperature solution obtained for a polydisperse (measured) and monodisperse drop distribution and a water flow rate of 2.84 kg/m^{2}s with an air flow rate of 2.28 kg/m^{2}s. The air side solution is shown in figures 5.5 and 5.8 for the same flow conditions.

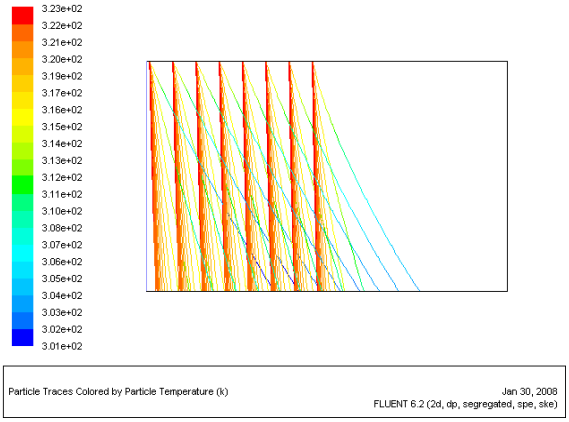

Figure 5.3 : Water temp. (dist. A - measured)

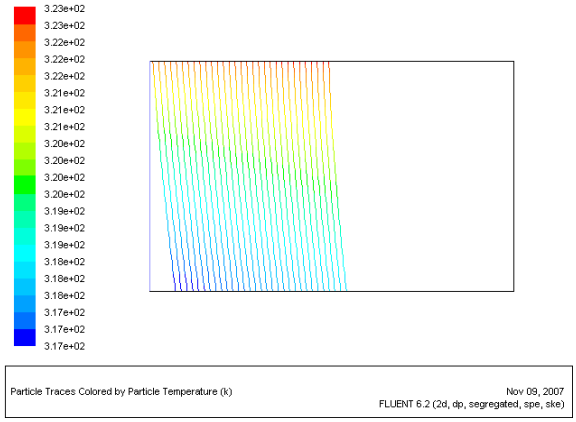

Figure 5.4 : Water temperature (dist. A-mono)

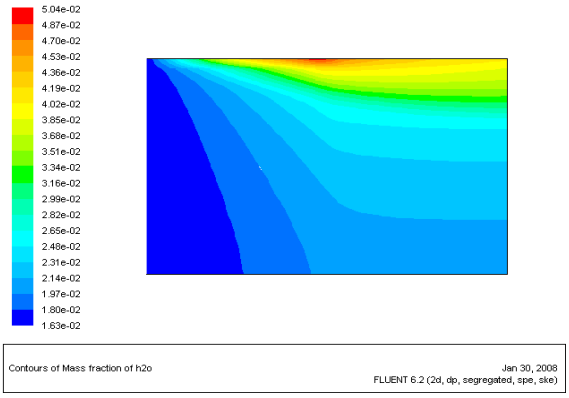

Figure 5.5 : Air humidity (dist. A – measured)

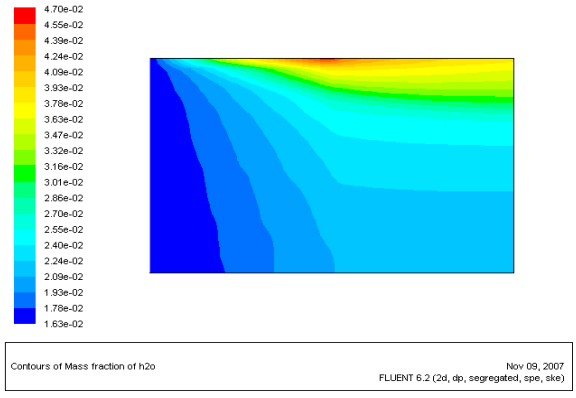

Figure 5.6 : Air humidity (dist. A – mono)

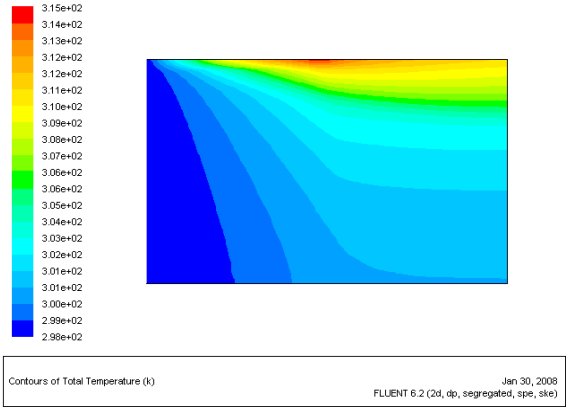

Figure 5.7 : Air temp. (dist. A – measured)

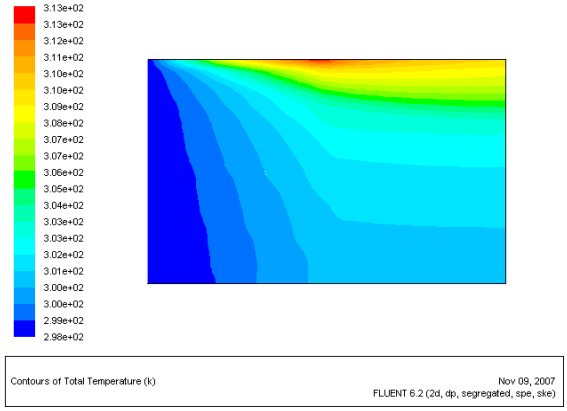

Figure 5.8 : Air temperature (dist. A – mono)

5.4 Results

The results for the average outlet water temperature as predicted with the CFD model for the different flow combinations mentioned in the previous section can be seen in figure 5.9.

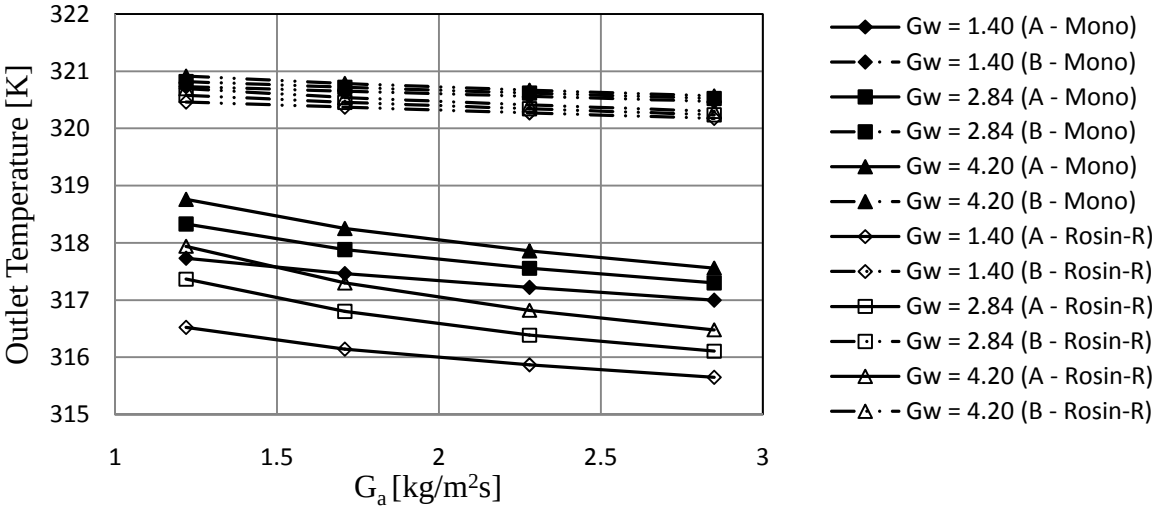

(a) Rosin-Rammler polydisperse and Sauter monodisperse

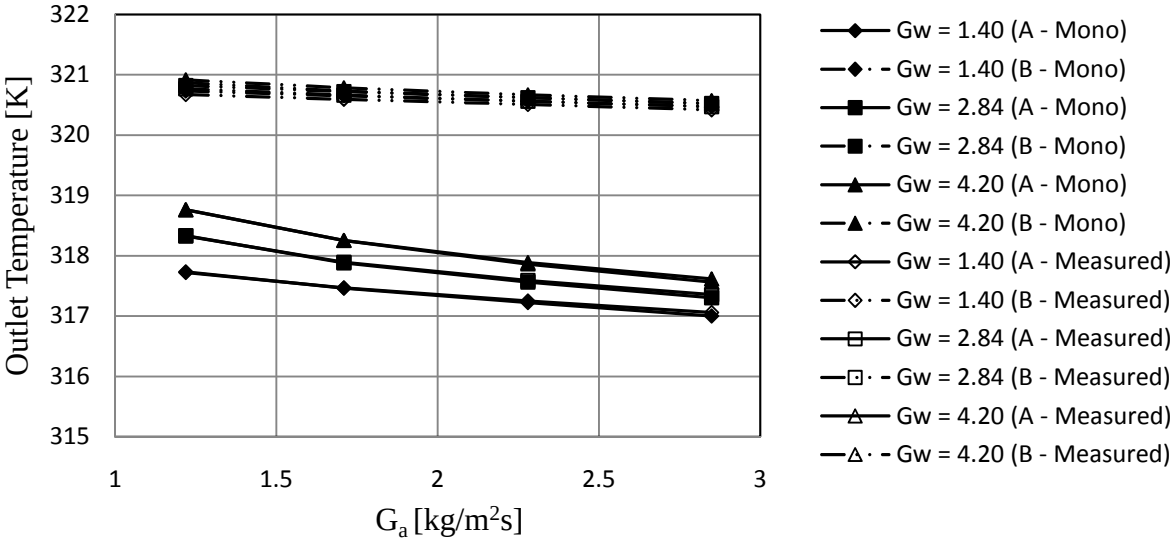

(b) Measured polydisperse and Sauter monodisperse

Figure 5.9 : Water outlet temperatures as predicted with CFD

By numerically integrating (Euler) the equations of motion and cooling of a single drop (chapter 3) and assuming a Lewis factor of unity, the Merkel number for a rain zone with constant air properties can be determined. The Merkel number for a monodisperse drop distribution of 2.73 mm and 5.19 mm respectively are modelled (chapter 3) in cross flow and the results are shown in figures 5.10.

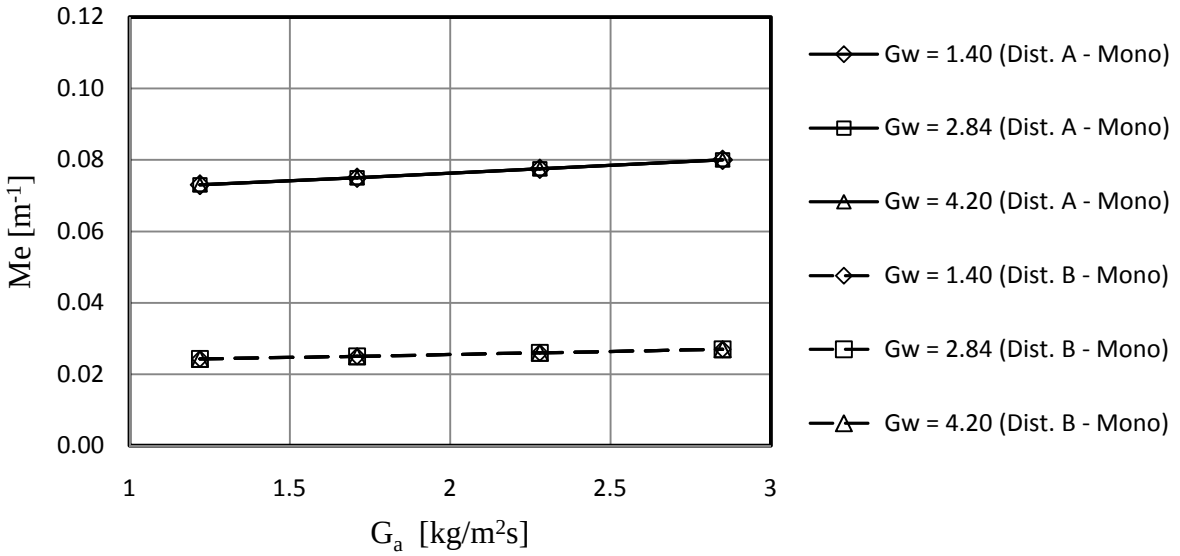

Figure 5.10 : Merkel numbers for distribution A and B (Lagrangian method)

The Merkel method incorporates the effects of changing air properties, but makes the simplifying assumption that the water evaporation mass is negligible in the calculations, but that the air that exits the rain zone is saturated. The Merkel method is the method that is generally applied in industry and is recommended in international standards. The results of the Merkel method are shown in figure 5.11 and based on the outlet temperatures predicted by the CFD analysis.

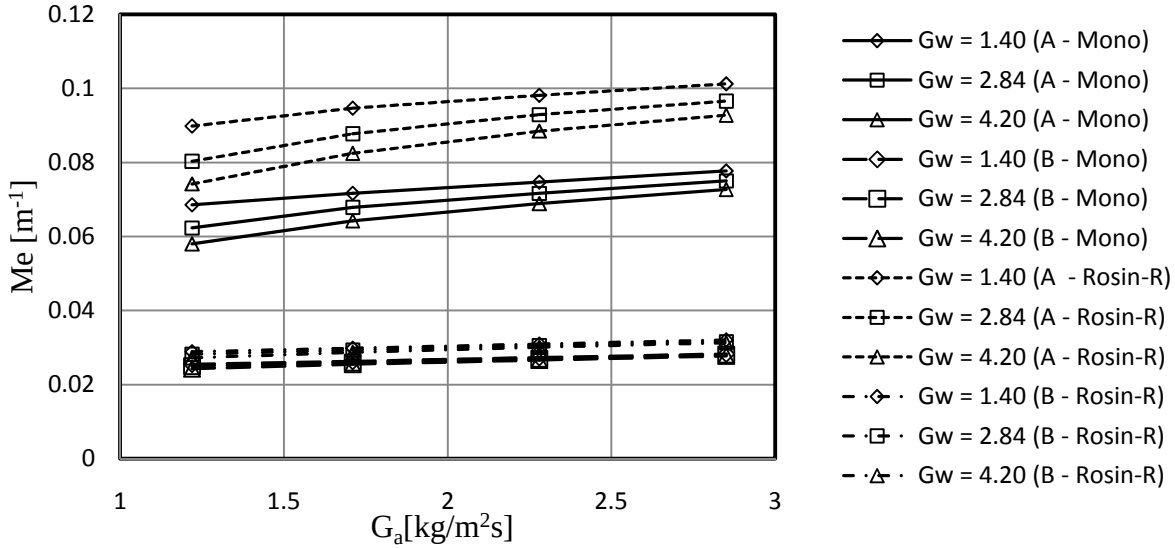

(a) Rosin-Rammler polydisperse and Sauter monodisperse

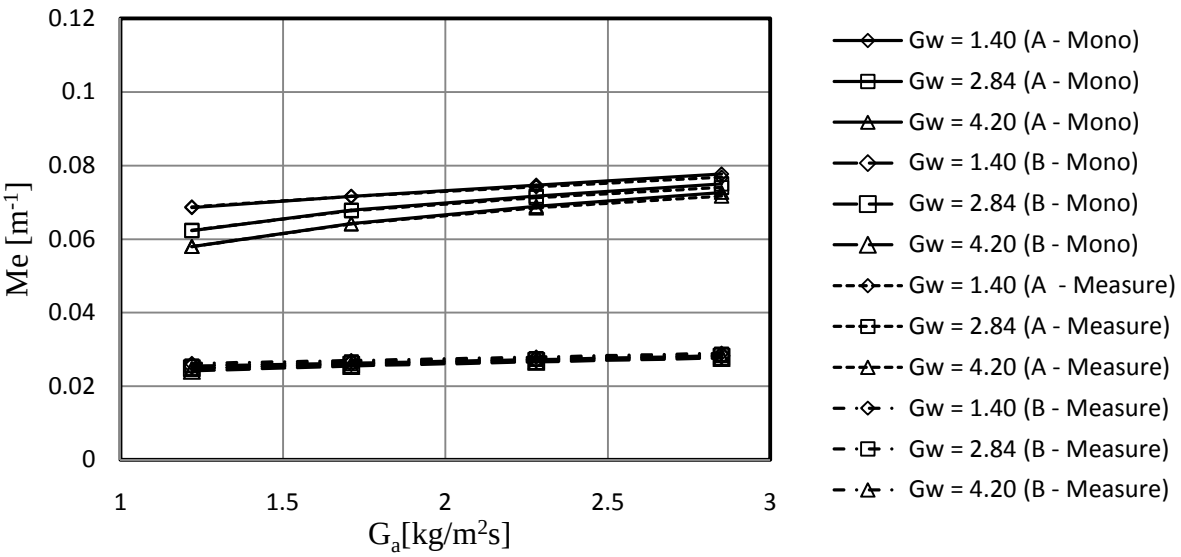

(b) Measured polydisperse and Sauter monodisperse

Figure 5.11 : Merkel numbers for distributions A and B (Merkel method)

The e-NTU method is based on the same simplifying assumptions than the Merkel method and the results are given in figure 5.12 for distributions A and B and are again based on the temperatures predicted by the CFD analysis.

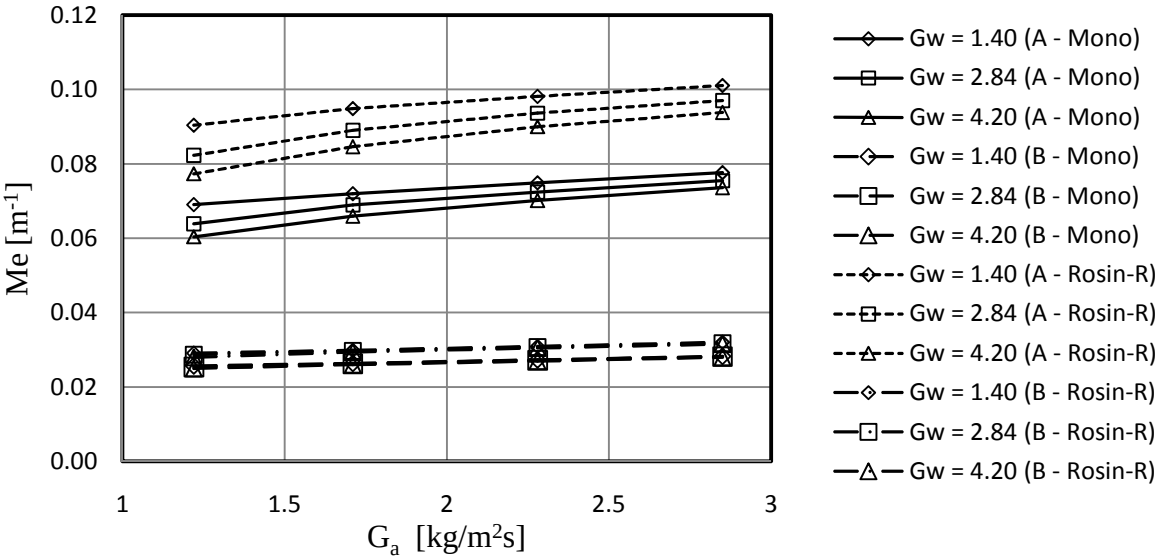

(a) Rosin-Rammler polydisperse and Sauter monodisperse

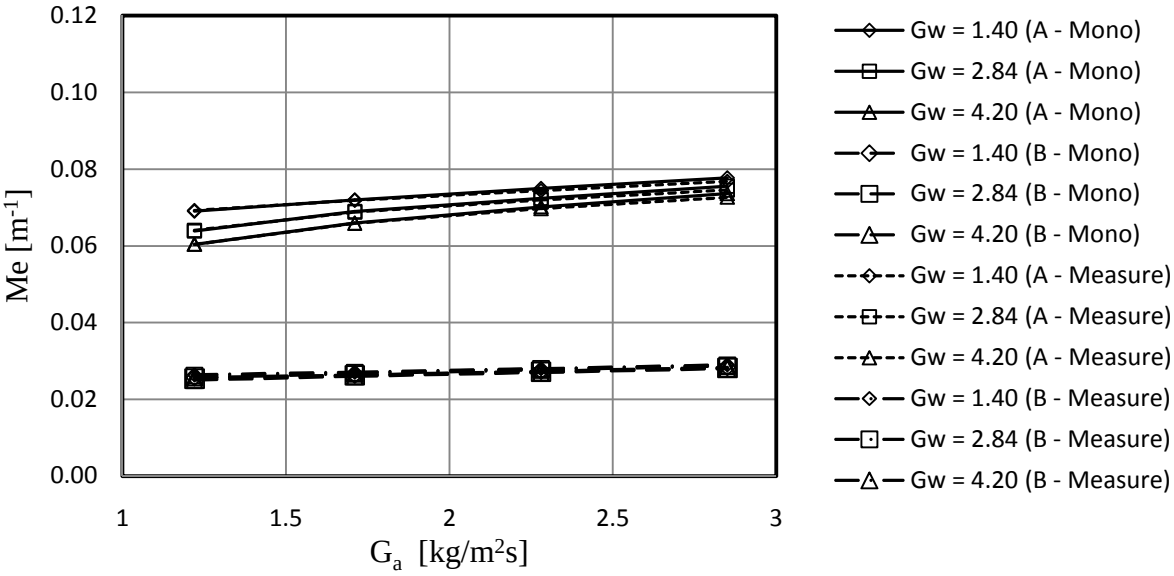

(b) Measured polydisperse and Sauter monodisperse

Figure 5.12 : Merkel numbers for distributions A and B (e-NTU method)

A more rigorous method for determining the Merkel number of the rain zone is the Poppe method. This method does not make the simplifying assumptions of the previous two methods and the Merkel numbers obtained with the Poppe method based on the CFD results are shown in figure 5.13. An Eulerian method of integration is chosen for the Poppe method in this case.

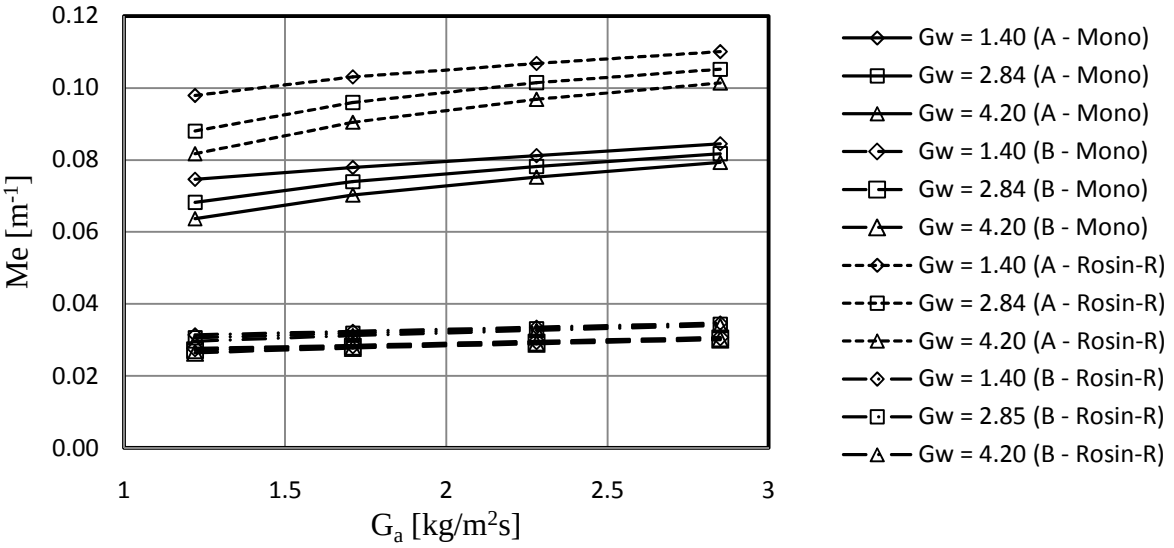

(a) Rosin-Rammler polydisperse and Sauter monodisperse

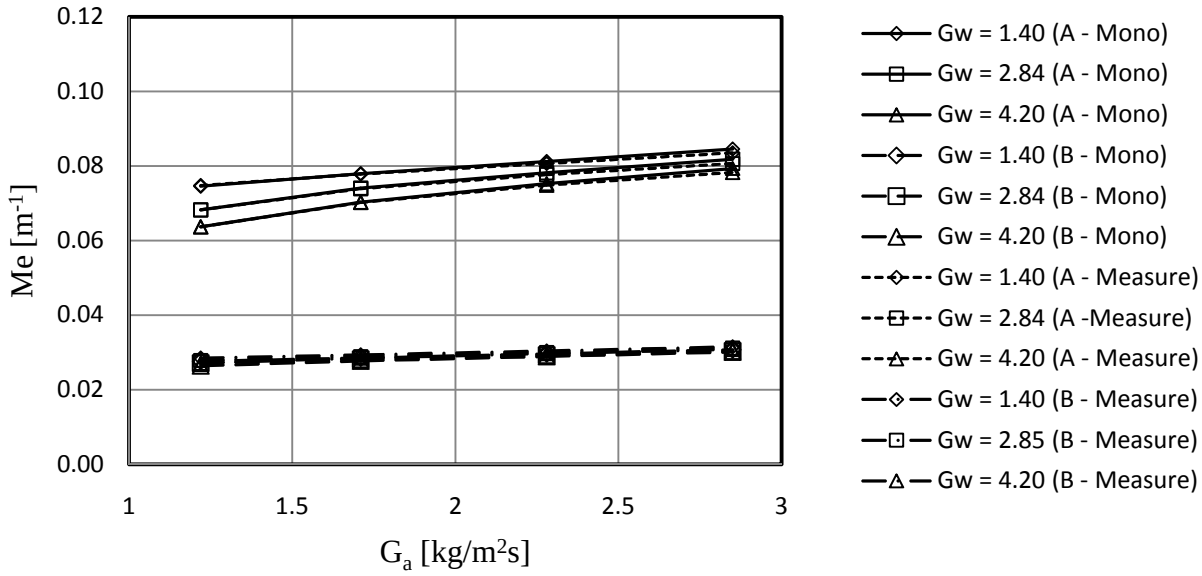

(b) Measured polydisperse and Sauter monodisperse

Figure 5.13 : Merkel numbers for distributions A and B (Poppe method)

The pressure drop of a rain zone consisting of 2.73 (Distribution A – monodisperse) and 5.19 mm (Distribution B – monodisperse) monodisperse drop distributions respectively can be seen in figures 5.14 and 5.15, as determined with equation (5.23) from the Lagrangian model (chapter 3) and with CFD.

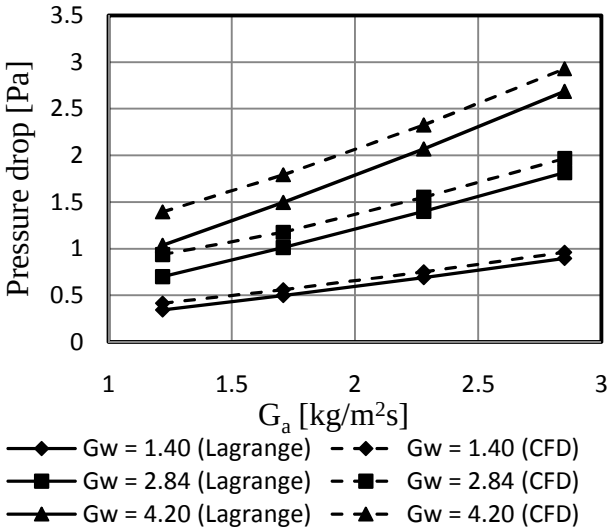

Figure 5.14 : Pressure drop (Dist. A – mono)

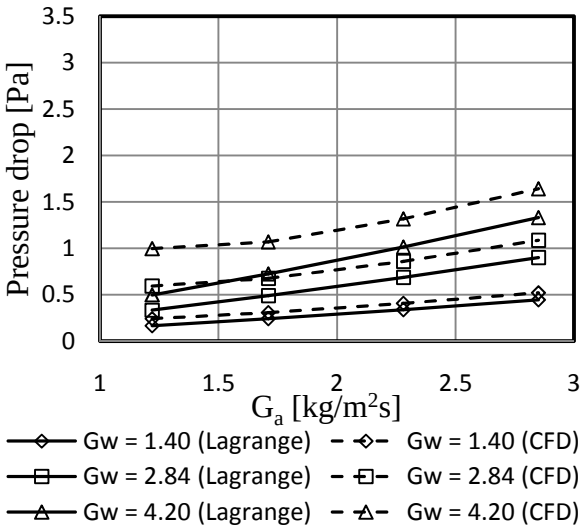

Figure 5.15 : Pressure drop (Dist. B – mono)

Figures 5.16 and 5.17 shows the pressure differences over a monodisperse and polydisperse (Rosin Rammler distribution) rain zone as modelled with CFD while figures 5.18 and 5.19

shows a pressure drop comparison between the monodisperse distribution and the exact measured polydisperse distribution.

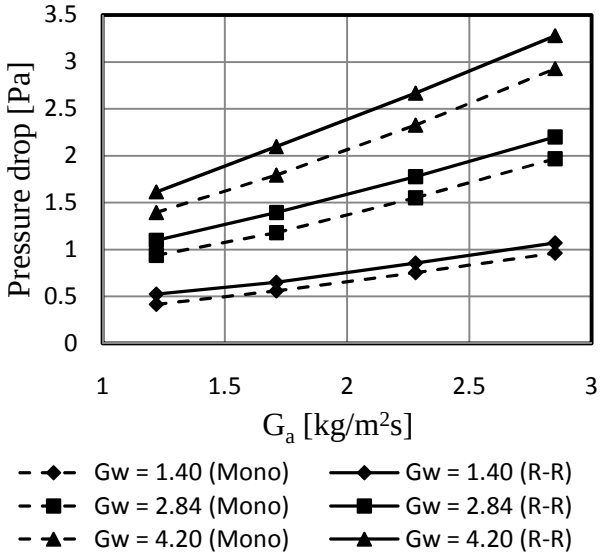

Figure 5.16 : Pressure drop (Distribution A)

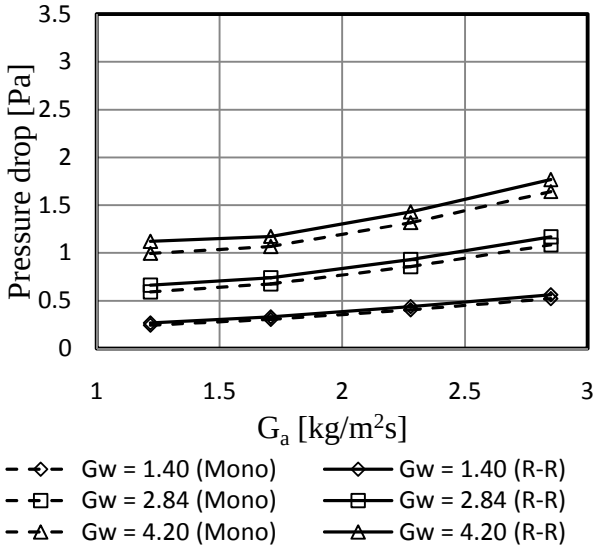

Figure 5.17 : Pressure drop (Distribution B)

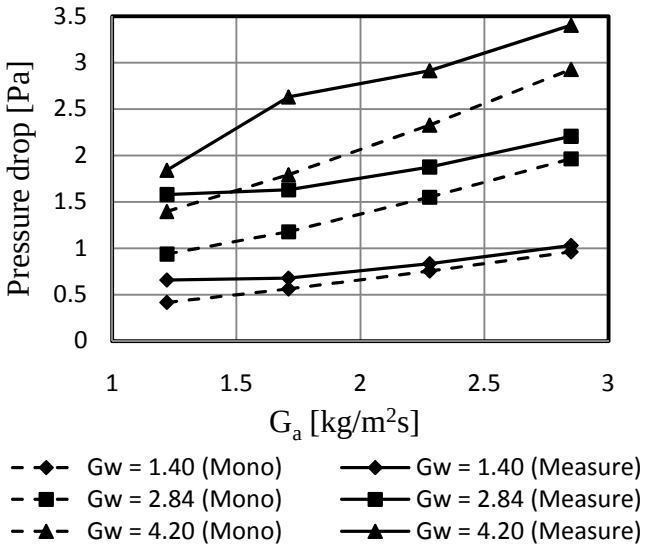

Figure 5.18 : Pressure drop (Distribution A)

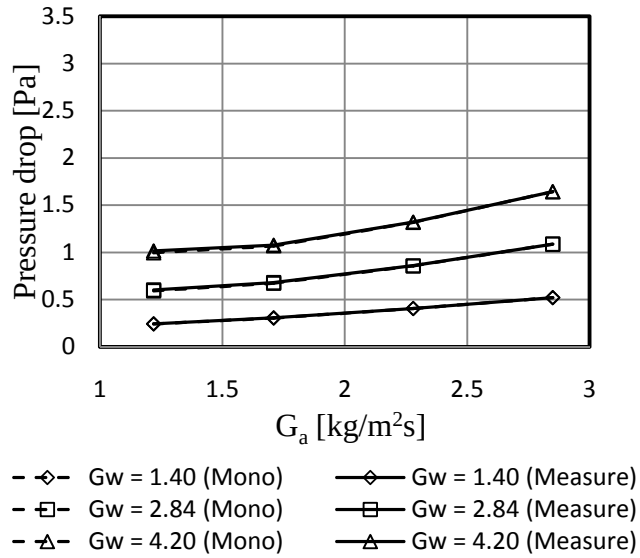

Figure 5.19 : Pressure drop (Distribution B)

The loss coefficients based on a uniform inlet velocity to the rain zone are shown in figures 5.20 and 5.21. In both figures the results for the Rosin-Rammler polydisperse distribution are compared to the results for the monodisperse distribution.

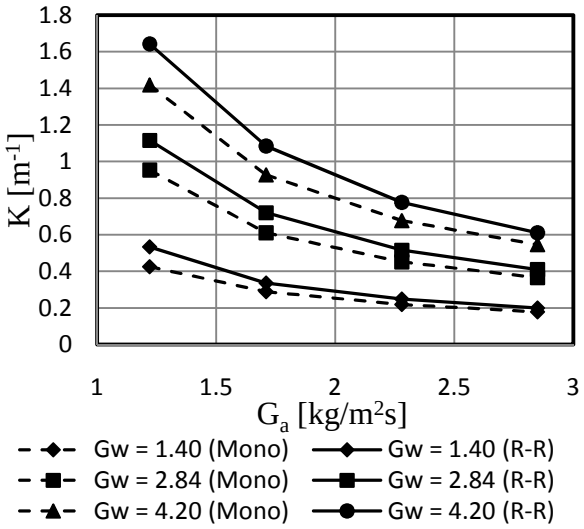

Figure 5.20 : Loss coefficients (Dist. A)

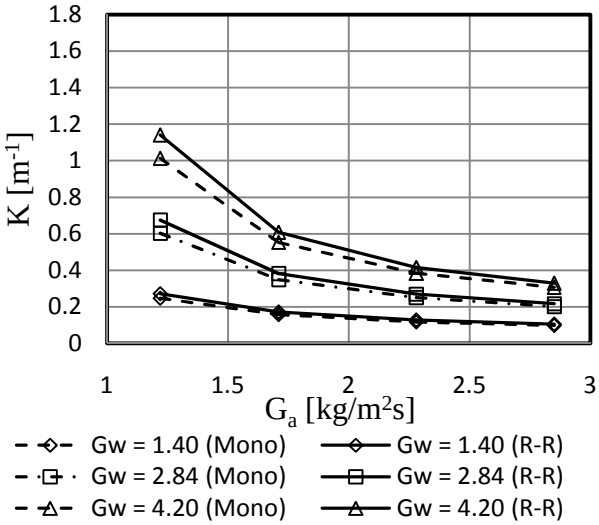

Figure 5.21 : Loss coefficients (Dist. B)

5.5 Discussion and recommendations

It can be seen from the previous section that the Merkel numbers obtained with each model compare relatively well for the different models except that the Poppe predict Merkel numbers that is about 9 % higher than that of the Merkel and e-NTU method.

Figure 5.22 shows the Merkel number ratio between polydisperse distributions A and B, as determined with the Rosin Rammler function and also between monodisperse distributions A and B.

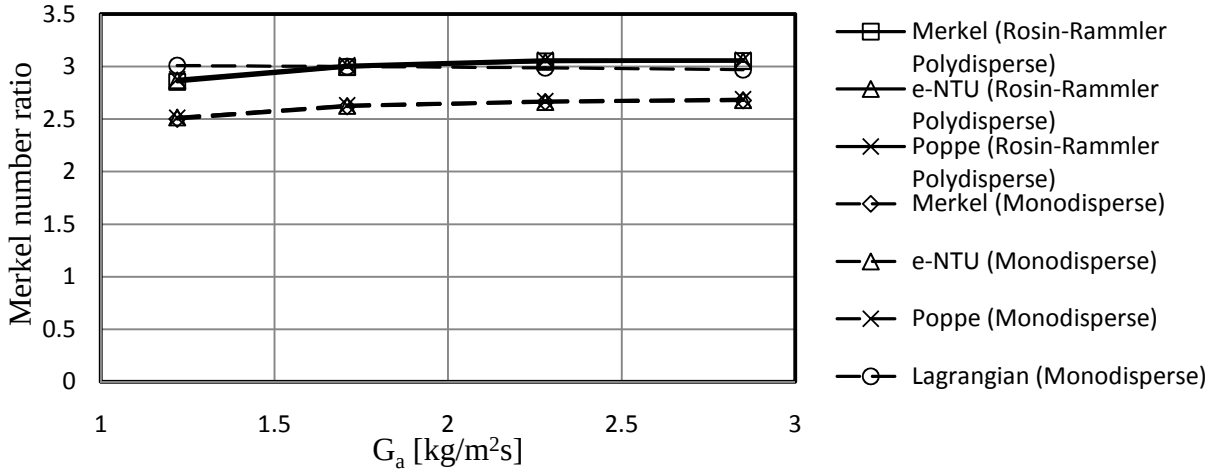

Figure 5.22: Rain zone Merkel ratio between monodisperse and polydisperse distributions A and B (G_w = 2.84 kg/m^{2}s)

The Merkel number ratio between Rosin Rammler polydisperse distributions A and B is around 3 and the Merkel ratio between monodisperse distributions A and B is around 2.6 with

the Lagrangian model also predicting ratios of around 3. The estimated increase in the total Merkel number of a cooling tower estimated with different methods based on monodisperse and Rosin Rammler polydisperse distributions A and B can be seen in figure 5.23.

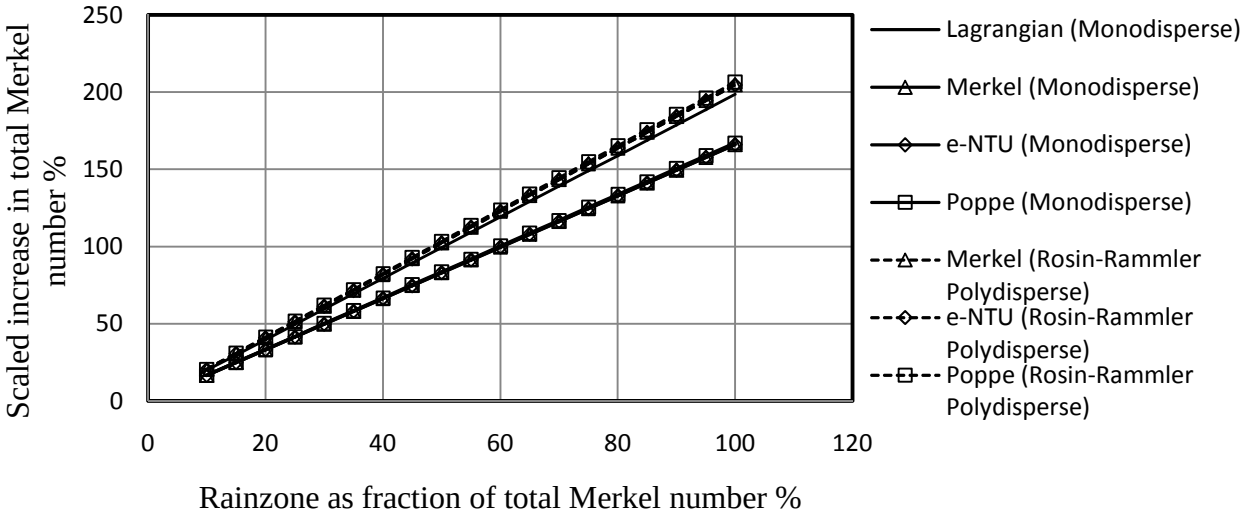

Figure 5.23 : Scaled increase in total Merkel number between distributions A and B in the rain zone, G_w = 2.84kg/m^{2}s, G_a 2.28 kg/m^{2}s

If it is assumed that the rain zone contributes 20 % to the total tower Merkel number, the scaled increase in total tower Merkel number can be defined by

$$Scaled\ Tower\ Merkel\ increase\ (\%) = 20\% \left[\frac{Me_{rzn}}{Me_{rzo}} - 1\right] \qquad (5.24)$$

Figure 5.24 shows the ratio between the rain zone pressure drops of distribution A and B based on monodisperse and polydisperse distributions.

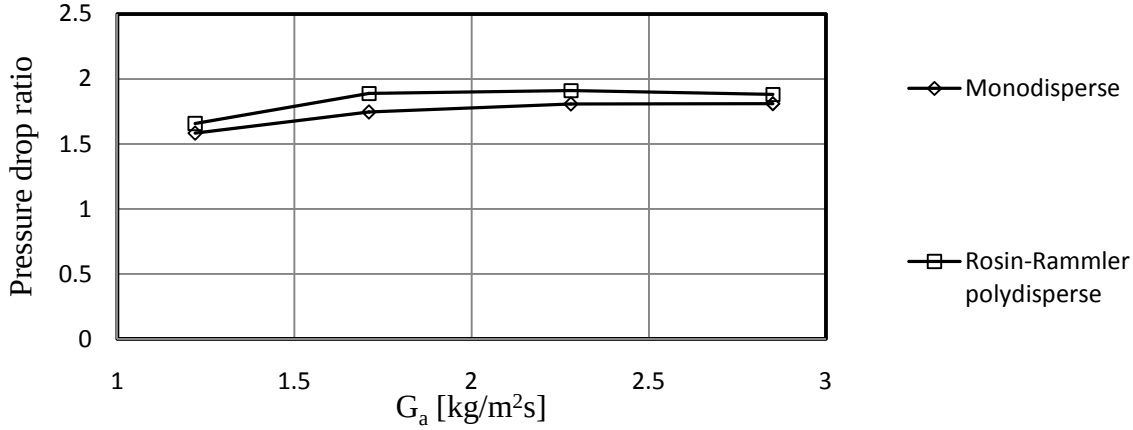

Figure 5.24 : Rain zone pressure drop ratio between distributions A and B (G_w = 2.84 kg/m^{2}s)

By assuming that the rain zone contributes a certain percentage of the total pressure drop of the cooling tower, the increase in total pressure drop can be determined in a similar manner to the total Merkel number increase of figure 5.23. The result for this can be seen in figure 5.25.

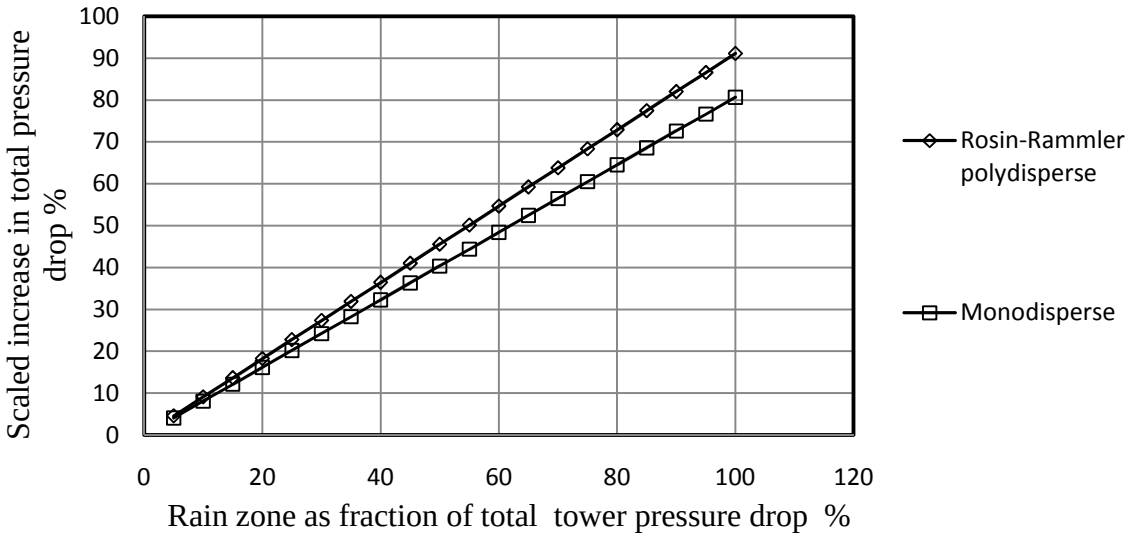

Figure 5.25 : Scaled increase in total tower pressure drop between distributions A and B, G_w = 2.84kg/m^{2}s, G_a = 2.28 kg/m^{2}s

6

CONCLUSION

6.1 Conclusions

Kröger [2004KR1] reports that the rain zone of a counter flow wet cooling tower is responsible for 10-20 % of the total heat rejected by the tower. This means that an improvement in this region could lead to a considerable improvement in the overall performance. The performance of the rain zone can be improved by decreasing the average drop size in this region, because smaller drops fall slower and result in a larger interfacial area between the hot water and cooling air (chapter 3). The average drop size can be reduced by installing splash grids in the rain zone which, according Kröger [2004KR1], can reduce the Sauter mean diameter to between 3 and 4 mm.

The initial drop distribution in the rain zone depends on the type of fill that is used in the cooling tower above the rain zone. The drop distributions immediately below three types of cooling tower fill are measured in a counter flow test facility (film fill, trickle fill and fibre cement fill (chapter 2)). The Sauter mean diameters under the trickle and film fill for different air and water flow combinations vary between 5 and 6 mm with the trickle fill generally giving the smallest drops, which is also stated by Kröger [2004KR1]. The fibre cement fill produced the largest Sauter mean diameter with a maximum measured Sauter mean of 5.977 mm. For all three fills tested it can be said that an increased water flow rate leads to slightly larger Sauter mean diameters.

The average drop size in the rain zone produced by film and trickle fills can be decreased by inserting grids below these fills to break the larger drops up into a larger number of smaller drops. The drop sizes below a designed slat grid and an expanded metal grid are measured, with the designed grid producing the best drop break-up. Sauter mean diameters of 2.84 mm for a single layer and 2.73 mm for a double layer inserted at 0.6 m and 0.8 m respectively below a trickle fill (chapter 2). A Sauter mean diameter of 2.47 mm is measured when a grid is spaced 0.8 m below the fill and the spacing between the two grids is also 0.8 m. A Sauter

mean diameter of 3.15 mm and 3.1 mm are measured below one and two layers of expanded metal grid placed 0.6 m and 0.4 m below the trickle fill.

From the modelling of the slat grid (chapter 4) it can be seen that the drop break-up through the grid is a function of slat width, slat spacing and distance between the grid and the fill, with the latter together with slat width having the biggest influence on the results. From the modelling and the measured results it can be concluded that the optimum spacing between the grid and the fill is between 0.6 m and 0.8 m. If the spacing is increased further the Sauter mean below the grid either stays constant or starts to increase again. This phenomenon was also observed by Oosthuizen [1995OO1] for a double layer of coarse expanded metal grid, where the smallest Sauter mean (4.05 mm) below the grids were measured at a fill-grid spacing of 0.67 m. From the modelling results (chapter 4) it is also concluded that the best slat width is 3 mm. For the chosen slat spacing of 10 mm the porosity of the grid is 77 % and Dreyer [1994DR1] concludes that the optimal porosity of a grid must be around 80 %.

It is interesting to see that when three layers of the designed slat grid are inserted into the rain zone the Sauter mean diameter is larger than with one layer. A reason for this could be the fact that the dripping from below the slats becomes more dominant because of the increased number of slats. The size of the primary drops dripping from below 3 mm slats is measured to be 6.88 mm in diameter while it is predicted to be 6.35 mm (chapter 4). Dreyer measured a primary drop size below a 3 mm slat of 6 mm in diameter. By changing the profile of the bottom of the slat the size of the primary drop is reduced to 4.01 mm (table 4.2).

A considerable improvement in rain zone heat and mass transfer is obtained by decreasing the Sauter mean drop size from 5.19 (distribution B) mm to 2.73 mm (distribution A) as is possible with two layers of the designed slat grid for a water mass velocity of 2.84 kg/m^{2}s and no counter flowing air. Smaller drops also cause the pressure drop in the rain zone to increase. From the CFD results it can be seen that the Merkel number improves by around 162 %, but that the pressure drop increased by 73 %. Assuming that the rain zone Merkel number is 10 – 20 % of the total Merkel number, a 162% increase in rain zone Merkel number results in a 33-66% increase in total Merkel number.

REFERENCES

1925ME1 Merkel, F., Verdunstungskühlung, VDI-Zeittschrift, Vol. 70, No70, pp. 123 – 128, January 1925

1934GI1 Gilliland, E.R. , *Diffusion Coefficients in Gaseous Systems,* Ind. Eng. Chem. , Vol. 26, pp. 681, 1934

1938FR1 Frössling, N. , *Über die Verdunstung Fallender Tropfen,* Gerlands Beitrage Zur Geophysik, Vol. 52, pp. 170 – 216, 1938

1939RO1 Rosin, P.P. , Rammler, E. , *Laws Governing the Fineness of Powdered Coal,* Journal of the Institute of Fuel, Vol. 7, pp. S-14 – S-15, 1939

1951BA1 Baines, W. D. , Peterson, E. G. , *An Investigation of Flow through Screens,* Transactions of the ASME, Vol. 73, No. 1, pp. 467 – 480, 1951

1951SN1 Snyder, R.W. , *The Cooling of a Free Falling Water-Drop,* IMechE, ASME Proceedings of the General Discussion on Heat Transfer, pp. 160 – 166, September 1951

1952RA1 Ranz, W.E., Marshall, W.R., *Evaporation from Drops,* Chemical Engineering Progress, Vol. 48, No.3, pp. 141-146, 1952

1965BO1 Bosnjakovic, F. , *Technische Thermodinamik*, Theodor Steinkopf, Dresden

1971LE1 Levin, Z., Hobbs, P.V., *Splashing of water drops on solid and wetted surfaces: hydrodynamics and charge separation,* Philosophical Transactions of the Royal Society of London, Series A, Vol. 269, pp. 555 – 585, 1971

1972LE1 LeClair, B.P. , Hamielec, A.E. , Pruppacher, H.R. , Wall, W.D. , *A Theoretical Study of the Internal Circulation in Water Drops Falling at Terminal Velocity in Air*, Journal of Atmospheric Sciences, Vol. 29, pp.728 – 740, 1972

1974HO1 Hollands, K.G.T. , *An Analysis of a Counter Flow Spray Cooling Tower,* International Journal of Heat and Mass Transfer, Vol. 17, pp. 1227 – 1239, 1974

1976YA1 Yao, S.C. , Schrock, V.E. , *Heat Transfer from Free Falling Drops,* Journal of Heat Transfer, Vol 98, No.1, pp. 102 – 126, 1976

1977BE1 Beard, K.V. , *On the Acceleration of Large Water Drops to Terminal Velocity,* Journal of Applied Meteorology, Vol. 16, pp. 1068 – 1071, October 1977

1977MI1 Miura, K. , Miura, T. , Ohanti, S. ,*Heat and Mass Transfer to and from Droplets,* AIChE Symposium Series, Vol. 73, No. 163, pp. 95 – 102, 1977

1977ST1 Stow, C.D., Stainer, R.D., *The physical products of a splashing water drop,* Journal of the Meteorological Society of Japan, Vol. 55, No.5, pp. 518 – 531, October 1977

1978PR1 Pruppacher, H.R. , Klett, J.D. , *Microphysics of Clouds and Precipitation*, D. Reidel Publishing Company, Dordrecht, Holland, 1978

1979AZ1 Azzopardi, B.J. , *Measurement of Drop Sizes,* International Journal of Heat and Mass Transfer, Vol 22, pp. 1245 – 1279, 1979

1978CL1 Clift, R. , Grace, J. R. , Weber, M. E. , *Bubbles Drops and Particles,* Academic Press, New York, 1978

1980YU1 Yung, D. , Lorenz, J.J. , Ganic, E.N. , *Vapour/Liquid Interaction in and Entrainment in Falling Film Evaporators*, ASME Journal of Heat Transfer, Vol. 102, pp. 20 – 25, February 1980

1981AL1 Alkidas, A. C., *The Influence of Size-Distribution Parameters on the Evaporation of Polydisperse Dilute Sprays,* International Journal of heat and Mass Transfer, Vol. 24, No. 12, pp. 1913 – 1923, 1981

1984PE1 Perry, Robert. H., *Perry's Chemical Engineering Handbook, 6th Edition,* McGraw-Hill Book Company, 1984

1987BE1 Beard, K.V. , Chuang, C. , *A New Model for the Equilibrium Shape of Raindrops,* Journal of the Atmospheric Sciences, Vol. 44, pp. 1509 – 1524, 1987

1986TU1 Turton, R. , Levenspiel, O. , *A Short Note on the Drag Correlation for Spheres*, Powder Technology, Vol 47, pp.83 – 86, 1986

1988YA2 Yao, S.C. , Hochreiter, L.E. , Cai, K.Y. , *Dynamics of Droplets Impacting on Thin Strips*, ASME Journal of Heat Transfer, Vol. 110, pp. 214-220, February 1988

1989JA1 Jaber, H. , Webb, R.L. , *Design of Cooling Towers by the Effectiveness-NTU Method*, Journal of Heat Transfer, Vol. 111, pp. 837-843, 1989

1990MA1 Marseilles, T.J. , Schliesing, J.S. , Bell, D.M. , Johnson, B.M. , *Extended Cooling Tower Thermal Performance Prediction using a Liquid-side Film Resistance Model*, Pacific Northwest Laboratory, Richland, Washington, April 1990

1990MI1 Miller, D. S. , *Internal Flow Systems*, 2nd Edition, BHRA (Information Services), Cranfield, 1990

1991PO1 Poppe, M. , Rögener, H. , 1991, *Berechnung von Rückkühlwerken*, VDI-Wärmeatlas, pp. Mi 1 – Mi 15.

1994DR1 Dreyer, A.A. , *Modelling of a Cooling Tower Splash Pack*, Ph.D. Dissertation, University of Stellenbosch, Stellenbosch, South Africa, 1994

1994GR1 Grange, J. L. ,1994, *Calculating the Evaporated Water Flow in Wet Cooling Towers*, paper presented at the 9th IAHR Cooling Tower and Spraying Pond Symposium, von Karman Institute, Brussels, Belgium

1995OO1 Oosthuizen, H. R. , *Enhancement of Cooling Tower Performance by Manipulating of Rain Zone Drop Size*, MSc.Eng Dissertation, University of Stellenbosch, Stellenbosch, South Africa, 1995

1996DR2 Dreyer, A. A. , Erens, P. J. , *Modelling of Cooling Tower Splash Pack*, International Journal of Heat and Mass Transfer, Vol. 39, No. 1, pp. 109 – 123, 1996

1996IN1 Incropera, Frank. P., DeWitt, Divid. P., *Fundamentals of Heat and Mass Transfer*, 4th Edition, John Wiley and Sons, Inc. 1996

1997FE1 Ferreira, J.M. , Chabra, R.P. , *Accelerating Motion of a Vertically Falling Sphere in Incompressible Newtonian Media: An Analytical Solution*, Powder Technology, Vol. 97, pp. 6 – 15, 1998

1997LI1 Liu, Z. , Reitz, R.D. , *An Analysis of the Distortion and Breakup Mechanisms of High Speed Liquid Drops*, International Journal of Multiphase Flow, Vol. 23, No. 4, pp. 631 – 650, 1997

1999WH1 White, F. M., *Fluid Mechanics*, Fourth Edition, McGraw and Hill, 1999

1999DE1 De Villiers, E., Kröger, D. G., *Analysis of Heat, Mass and Momentum Transfer in the Rain Zone of Counter Flow Cooling Towers*, Journal of Engineering for Gas Turbines and Power, Vol. 121, pp. 1 – 5, October 1999

2002GO1 Gonzalez, R. C., Woods, R. E., *Digital Image Processing*, Second Edition, Prentice Hall, 2002

2002RO1 Rogers, W.J. , Kihm, K.D. , Mannan, M.S. , Krishna, K. , Sukmarg, P. , *Non-Intrusive Characterisation of Heat Transfer Aerosol Sprays Released from an Orifice*, Journal of Loss Prevention in the Process Industries, Vol 15, pp. 19 – 27, 2002

2003KL1 Kloppers, J. C. , *A Critical Evaluation and Refinement of the Performance Prediction of Wet Cooling Towers*, Ph.D. Dissertation, University of Stellenbosch, Stellenbosch, South Africa, 2003

2003KH1 Jameel-Ur-Rehman Khan, Yaqub, M. , Zubair Syed M. , *Performance Characteristics of Counter Flow Wet-Cooling Towers*, Energy Conversion and Management, Vol 44, pp. 2073 – 2091, 2003

2004KR1 Kröger, D. G. , *Air-cooled Heat Exchangers and Cooling Towers*, Pennwell, 2004

2005KL2 Kloppers, J.C. , Kröger, D.G. , *Cooling Tower Performance Evaluation: Merkel Poppe and e-NTU Methods of Analysis*, Journal of Engineering for Gas Turbines and Power, Vol. 127, pp. 1 – 7 , January 2005

2005MA1 Martin, H. , *How to Predict Heat and Mass Transfer from Fluid Friction*, 4th International Conference on Heat Transfer, Fluid Mechanics and Thermodynamics, Paper K2, Cairo, Egypt, 2005

2006VI1 Viljoen, D. J. , *Evaluation and Performance Prediction of Cooling Tower Spray Zones*, MSc.Eng Thesis, University of Stellenbosch, Stellenbosch, South Africa, 2006

2007PI1 Pierce, D. J. *Evaluation and Prediction of Cooling Tower Rain Zones*, MSc.Eng Thesis, University of Stellenbosch, Stellenbosch, South Africa, 2007

A

THERMOPHYSICAL PROPERTIES

The properties listed in this appendix are as they appear in D.G Kröger's book, "Air Cooled Heat Exchangers and Cooling Towers".

A.1 Thermophysical properties of dry air from 220K to 380K at Standard Atmospheric Pressure (101325 Pa)

Density:

$$\rho_a = p_a/(287.08T), \text{ kg/m}^3 \tag{A.1}$$

Specific Heat:

$$c_{pa} = 1.045356 \cdot 10^3 - 3.161783 \cdot 10^{-1}T + 7.083814 \cdot 10^{-4}T^2 - 2.705209 \cdot 10^{-7}T^3, \text{ J/kgK} \tag{A.2}$$

Dynamic Viscosity:

$$\mu_a = 2.287973 \cdot 10^{-6} + 6.259793 \cdot 10^{-8}T - 3.131956 \cdot 10^{-11}T^2 + 8.15038 \cdot 10^{-15}T^3, \text{ kg/ms} \tag{A.3}$$

Thermal Conductivity:

$$k_a = -4.937787 \cdot 10^{-4} + 1.018087 \cdot 10^{-4}T - 4.627937 \cdot 10^{-8}T^2 + 1.250603 \cdot 10^{-11}T^3, \text{ W/mK} \tag{A.4}$$

A.2 Thermophysical properties of saturated water vapour from 273.15K to 380K

Vapour Pressure:

$$p_v = 10^z, \text{ Pa} \tag{A.5}$$

$$z = 10.79586\left(1 - \frac{273.16}{T}\right) + 5.02808 log_{10}\left(\frac{273.16}{T}\right)$$

$$+1.50474 \cdot 10^{-4}\left[1 - 10^{-8.29692\left\{\left(\frac{T}{273.16}\right)-1\right\}}\right]$$
$$+ 4.2873 \cdot 10^{-4}\left[10^{4.76955(1-273.16/T)} - 1\right] + 2.786118312$$

Specific Heat:

$$c_{pv} = 1.3605 \cdot 10^{3} + 2.31334T - 2.46784 \cdot 10^{-10}T^{5} + 5.91332 \cdot 10^{-13}T^{6}, \text{ J/kgK} \quad (A.6)$$

Dynamic Viscosity:

$$\mu_v = 2.562435 \cdot 10^{-6} + 1.816683 \cdot 10^{-8}T\ 2.579066 \cdot 10^{-11}T^{2} - 1.067299 \cdot 10^{-14}T^{3}, \text{ kg/ms} \quad (A.7)$$

Thermal Conductivity:

$$k_v = 1.3046 \cdot 10^{-2} - 3.756191 \cdot 10^{-5}T + 2.217964 \cdot 10^{-7}T^{2} - 1.111562 \cdot 10^{-10}T^{3}\ , \text{W/mK} \quad (A.8)$$

Vapour Density:

$$\rho_v = -4.062326056 + 0.10277044T - 9.76300388 \cdot 10^{-4}T^{2} + 4.475240795 \cdot 10^{-6}T^{3} - 1.004596894 \cdot 10^{-8}T^{4} + 8.9154895 \cdot 10^{-12}T^{5}\ , \text{kg/m}^3 \quad (A.9)$$

A.3 Thermophysical Properties of Mixtures of Air and Vapour

Density:

$$\rho_{av} = (1 + w)[1 - w/(w + 0.62198)]P_{abs}/(287.08T)\ , \text{ kg air-vapour/m}^3 \quad (A.10)$$

Specific Heat:

$$c_{pav} = \left(c_{pa} + wc_{pv}\right)/(1 + w)\ , \text{ J/K kg air-vapour} \quad (A.11)$$

Dynamic Viscosity:

$$\mu_{av} = \left(X_a\mu_a{M_a}^{0.5} + X_v\mu_v{M_v}^{0.5}\right)/\left(X_a{M_a}^{0.5} + X_v{M_v}^{0.5}\right)\text{, kg/ms} \quad (A.12)$$

where

M_a = 28.97 kg/mole, M_v = 18.016 kg/mole, X_a = 1/(1 + 1.608w) and

X_v = w/(w + 0.622)

Thermal Conductivity:

$$k_{av} = \left(X_a k_a {M_a}^{0.33} + X_v k_v {M_v}^{0.33}\right)/\left(X_a {M_a}^{0.33} + X_a {M_a}^{0.33}\right), \text{ W/mK} \quad \text{(A.13)}$$

Humidity Ratio:

$$w = \left(\frac{2501.6 - 2.3263(T_{wb} - 273.15)}{2501.6 + 1.8577(T - 273.15) - 4.184(T_{wb} - 273.15)}\right) \times \left(\frac{0.62509 p_{vwb}}{P_{abs} - 1.005 p_{vwb}}\right) - \left(\frac{1.00416(T - T_{wb})}{2501.6 + 1.8577(T - 273.15) - 4.184(T_{wb} - 273.15)}\right), \text{kg/ kg dry air} \quad \text{(A.14)}$$

Enthalpy:

$$i_{av} = \left[c_{pa}(T - 273.15) + w\{i_{fgwo} + c_{pv}(T - 273.15)\}\right]/(1 + w), \quad \text{J/kg air-vapour} \quad \text{(A.15a)}$$

Or the enthalpy of the air-vapour mixture per unit mass of dry air

$$i_{ma} = c_{pa}(T - 273.15) + w\left[i_{fgwo} + c_{pv}(T - 273.15)\right], \text{ J/kg dry air} \quad \text{(A.15b)}$$

where the specific heats are evaluated at (T + 273.15)/2 and the latent heat i_{fgwo}, is evaluated at 273.15 K according to equation (A.20) i.e. $i_{fgwo} = 2.5016 \times 10^6$ J/kg

A.4 Thermophysical Properties of Saturated Water Liquid from 273.15K to 380K

Density:

$$\rho_w = (1.49343 \cdot 10^{-3} - 3.7164 \cdot 10^{-6} T + 7.09782 \cdot 10^{-9} T^2 - 1.90321 \cdot 10{-}20{-}76{-}1, \text{ kg/m}^3 \quad \text{(A.16)}$$

Specific Heat:

$$c_{pw} = 8.15599 \cdot 10^3 - 2.80627 \cdot 10T + 5.11283 \cdot 10^{-2} T^2 - 2.17582 \cdot 10^{-13} T^6 \text{ , J/kgK} \quad \text{(A.17)}$$

Dynamic Viscosity:

$$\mu_w = 2.414 \cdot 10^{-5} \cdot 10^{247.8/(T-140)}, \text{kg/ms} \quad \text{(A.18)}$$

Thermal Conductivity:

$$k_w = -6.14255 \cdot 10^{-1} + 6.9962 \cdot 10^{-3}T - 1.01075 \cdot 10^{-5}T^2 + 4.74737 \cdot 10^{-12}T^4 \text{ , W/mK} \quad \text{(A.19)}$$

Latent heat of vapourization:

$$i_{fgw} = 3.4831814 \cdot 10^{6} - 5.8627703 \cdot 10^{3}T + 12.139568T^2 - 1.40290431 \cdot 10^{-2}T^3 \text{ , J/kg} \quad \text{(A.20)}$$

Critical Pressure:

$$p_{wc} = 22.09 \cdot 10^{6} \text{ , Pa} \quad \text{(A.21)}$$

Surface Tension:

$$\sigma_w = 5.148103 \cdot 10^{-2} + 3.998714 \cdot 10^{-4}T - 1.4721869 \cdot 10^{-6}T^2 + 1.21405335 \cdot 10^{-9}T^3 \text{ , N/m} \quad \text{(A.22)}$$

B

DEVELOPMENT OF DROP SIZE MEASUREMENT EQUIPMENT AND SOFTWARE

B.1 Introduction

In order to do the drop size measurements required for this project a measurement technique is developed to meet specific requirements. A digital camera (Nikon D70S) is placed inside a specially designed housing that is inserted through the rain zone wall of the indoor counter flow test facility described in chapter 2. Images are taken of the drops in the rain zone and a specially developed software program is used to determine the diameter of each drop and also the drop distribution.

In this appendix the requirements and the design of the different components of the measurement system are discussed.

B.2 Equipment design criteria

B.2.1 Camera housing

- The housing must not cause air flow disturbance in the region that is photographed.
- The housing must not cause any water flow interference in the region that is photographed.
- There must be no surfaces on the housing from where drops can splash or drip into the photo region.
- The housing must have a photographic background so that only a certain control volume is photographed.
- Backlighting must be possible for the camera.
- No drops must form on the background.
- The housing must contain a bracket on which the camera can be fastened.
- The camera housing must keep the camera dry.

- There must be no windows between the camera and the image zone that is photographed on which drops can accumulate.

B.2.2 Drop images

- Drop images must have the highest resolution capable with the camera (6 megapixels).
- The images must have low noise levels that show up as speckles because they can make image processing difficult.
- The drop edges must be well defined in the image.
- Drops must be captured in such a way that there is no blurring due to the motion of the drops.

B.2.3 Software program

- The software program must be able to isolate the drops in an image.
- It must be possible to set parameters in the program to analyse different types of images.
- The drops must be numbered and their sizes determined.
- The software program must be able to export the output data to Excel.
- The time to process an image must be as short as possible (2-3 minutes).
- The program must display results in a visual manner so that it can be checked by the user.

B.3 Description of photographic equipment

B.3.1 Camera housing

The camera housing protrudes through the side wall of the test facility rain zone extending into the middle of the rain zone (500 mm from the wall). Figure B.1 shows a detailed layout of the camera housing and a photograph of the housing can be seen in figure 2.8. This setup in the test section can be seen in figure 2.7. It was decided that it must be possible to measure drop sizes in the middle of the rain zone but that the camera itself must not be in the rain zone. The length from the camera to the middle of the control volume that is photographed is therefore 500 mm.

The camera housing consists out of a 250 mm round PVC pipe, a sandblasted glass background, flow distortion shield and a drip guard. A pipe diameter of 250 mm is necessary

since at 450 mm, the camera takes a 124 x 186 mm photo, which must not be impeded by the pipe. The flow distortion shield minimizes flow disturbances, because of the pipe housing, in the photographic region. A dripping guard keeps the water, running down the flow distortion shield, from entering the region that is photographed. A 300 mm x 300 mm glass plate, sandblasted on both sides, serves as a photographic background. It is placed at a distance of 550 mm from the camera, which leaves a 100 mm gap between the background and housing for the drops to be photographed to pass through. The sandblasted glass plate is attached to a sheet metal frame, held in place by four rods attached to the flow distortion shield. The sandblasted surface provides better wetting properties causing water to form a film as opposed to drops. Drop formation on the background is undesirable because these drops show up in the photographic images which are then included in the drop distribution measurement, leading to inaccuracies.

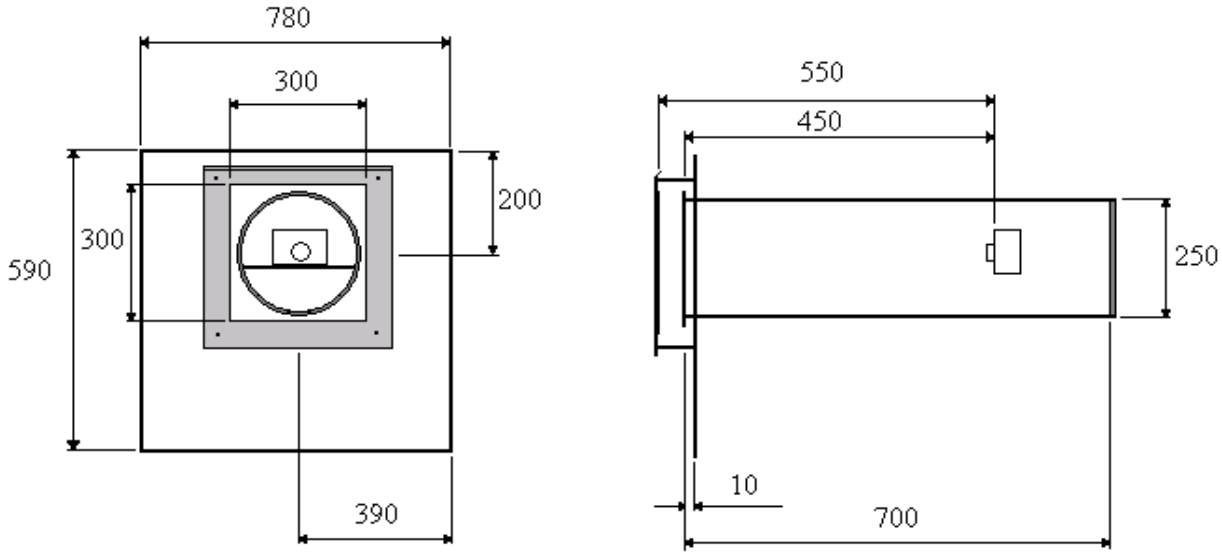

Figure B.1 : Schematic of the layout of the camera housing

Inside the pipe is a bracket onto which the camera can be fastened. The placement of the camera is done in such a way that the camera lens is on the centreline of the pipe.

B.3.2 Camera

Images with no blurring against strong backlighting are achieved with a Nikon D70S digital SLR camera with a shutter speed of 1/8000s.

B.3.3 Software program

An algorithm is developed, based on existing image processing techniques and implemented to extract drop data from photographic images. All the image processing operations implemented in this algorithm are done in the spatial domain.

After the image is read into the program, a high pass filter is applied to the image according to a matrix size that is provided by the user. This filter removes low frequency areas and retains the high frequency areas. A high frequency area is a region where the rate of colour change from one pixel to the next is high. The sharp edges around each drop on an image are high frequency regions and the high pass filter helps with isolating the edge regions so that they are more easily detectable. The larger the matrix size provided by the user the sharper the resultant image will be but the longer the processing time will be.

After the image sharpening operation an averaging filter is applied to the image. This operation makes the image more blurry, but makes individual noise pixels less prominent. The matrix size for this operation must therefore preferably be smaller than that of the sharpening operation so that the result at this point is still a sharper image.

The image is now ready for edge detection which is done by applying the Sobel operator to the image. A Sobel [2002GO1] operator determines the colour gradient at each pixel in a specific direction. This means that this operation must be done in the horizontal and vertical directions. When the results for both directions are obtained the absolute values of each pixel in both results are obtained. A threshold operation is then applied to both the absolute matrices in order to get rid of all the small gradients and is done according to a threshold value that is given relative to the largest gradient in both matrices. In other words if the user provides a threshold value of 0.01 it means that all gradients smaller than 1 % of the largest gradient in the matrix will be filtered out. The two matrices are combined by adding them together and a threshold operation is applied for the last time where all the pixels with a value larger than zero are given a value of 1. This is done to create a binary image where all the white pixels represent drop edges. At this point a closing operation is applied to the images. This operation basically does four things: (1) It smoothes the detected edges; (2) It fuses long thin gulfs and narrow breaks in the detected bodies; (3) Eliminates small holes in the edges; (4) Fills gaps in edges [2002GO1]. After this all the bodies that touch the side of the image are discarded.

An optional closing operation can be applied for the second time to the image to make sure the drop edges are connected.

Another option is a dilation/erosion operation. First a certain amount of the bodies are eroded after which they are dilated by the same amount. This approach may be used to disconnect bodies that must not be connected for example two drops that are close to each other.

Now that the drop edges are detected the areas between the edges are filled in order to represent a drop as a single white blob.

An optional erosion operation can be applied if the user sees that the drops in the blob images are larger than the original drops. An erosion value of 3 normally gives excellent results.

After the image processing operations the drops are counted and their sizes in pixels determined. Figure B.2 shows a flow chart of the image processing algorithm.

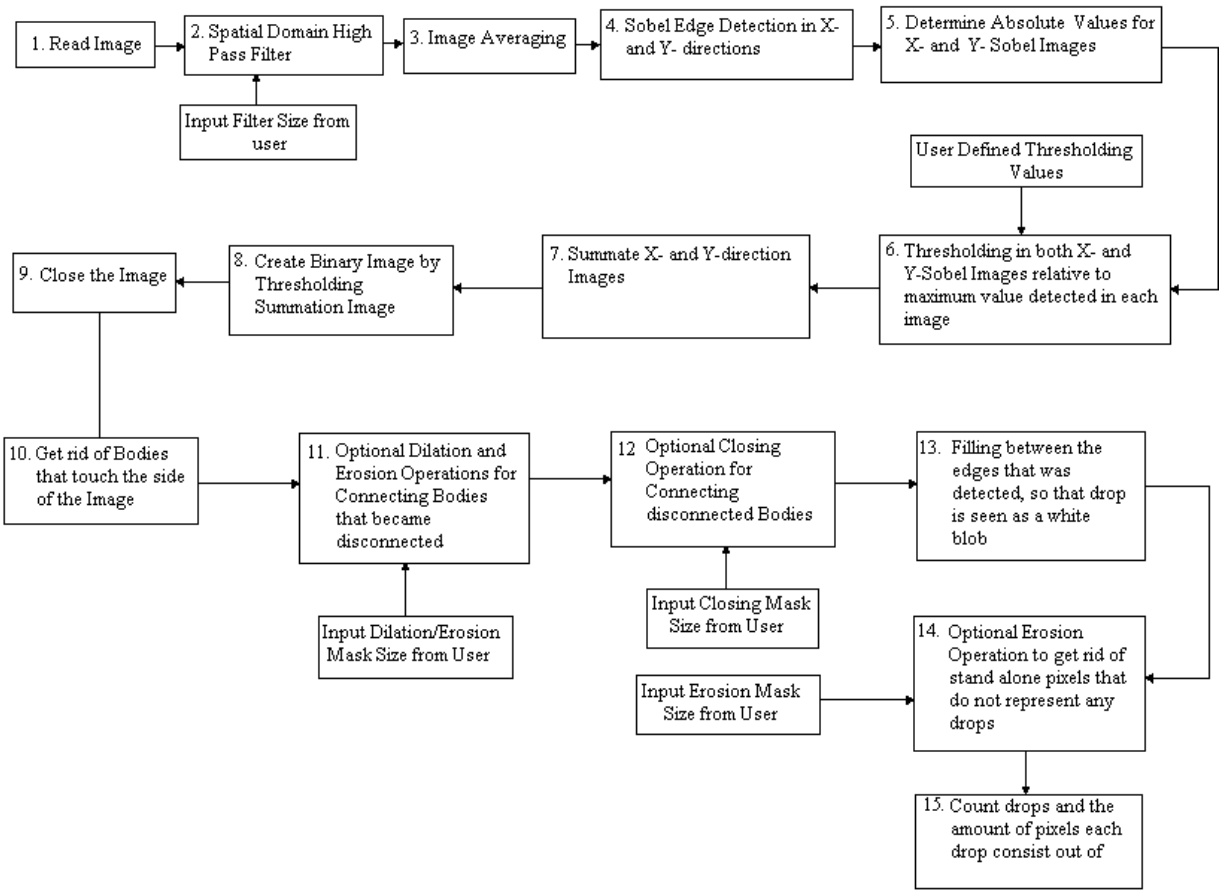

Figure B.2 : Image processing algorithm

C

DROP SIZE REDUCTION GRID DESIGN

This chapter refers to the drop size reduction grid used in chapter 2 and can be seen in figures 2.3 and 2.4

C.1 Design criteria

- Pressure drop must be kept at a minimum.
- Narrow, horizontally placed slats must be used for the grid.
- The slats must be supported so that they do not vibrate when subjected to water and air flow.
- It must be possible to connect more multiple grids together.
- The grid must have a porosity of around 80 % as recommended by Dreyer [1994DR1].

C.2 Description of the reduction grid design

The grid is designed for a distribution of which the largest drops are not more than 10 mm in diameter.

The spacing between the slats is chosen to be 10 mm because the effective break area of a slat that is impacted by a 10 mm drop is the sum of the slat width and the drop diameter times the slat length of the slat as shown by equation (4.23).

The width of the slat is found by modelling the change in Sauter mean diameter with changing slat width as shown in figure 4.12. From this figure it can be seen that the change in Sauter mean diameter between 3 mm to 5 mm decreases with 0.28 mm compared to the 1.27 mm reduction in Sauter mean between 0.5 and 3 mm. The loss coefficient on the other hand doubles from 3 mm to 5 mm. With this information in mind a slat width of 3 mm is chosen. The loss coefficient for sharp edged grids was correlated by Dreyer [1994DR1] from the data of Baines and Peterson [1951BA1] and Miller [1990MI1] and is given by

$$K_{\Delta p,grid} = 0.78\left(\left(\frac{1}{\beta}\right)^2 - 1\right)^{1.25} \quad \text{(C.1)}$$

Figure C.1 shows the loss coefficient for different slat widths with constant spacing of 10 mm between the slats.

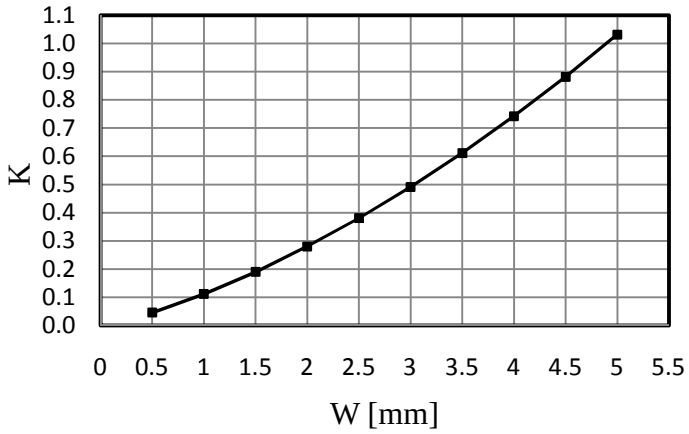

Figure C.1 : Loss coefficients for different slat widths with S = 10 mm

The porosity of the designed grid with 3 mm slats and 10 mm spacing between the slats is 77 %.

The slat height is chosen to be 1.2 times the maximum drop diameter to ensure no re-coalescing of drops below the slat.

In order to keep the slats from vibrating under different air and water flow conditions the slats are supported at four equally spaced locations along their lengths.

D

EXPERIMENTAL APPARATUS FOR DRIPPING EXPERIMENTS

The experimental apparatus used to investigate the dripping below different slats can be seen in figure D.1. In order to test the slat effectively, it is decided to make use of a V-shaped reservoir that overflows onto the slat that is being tested.

Water is fed to the V-shaped reservoir from a wall tap that is calibrated to give the desired water flow rate. The calibration is done by measuring the time it takes for the water to fill a 500 ml bottle. The setting is then marked out on the tap.

As the water overflows the edges of the reservoir it starts dripping below the slat and the images are captured with a Nikon D70S Digital SLR camera.

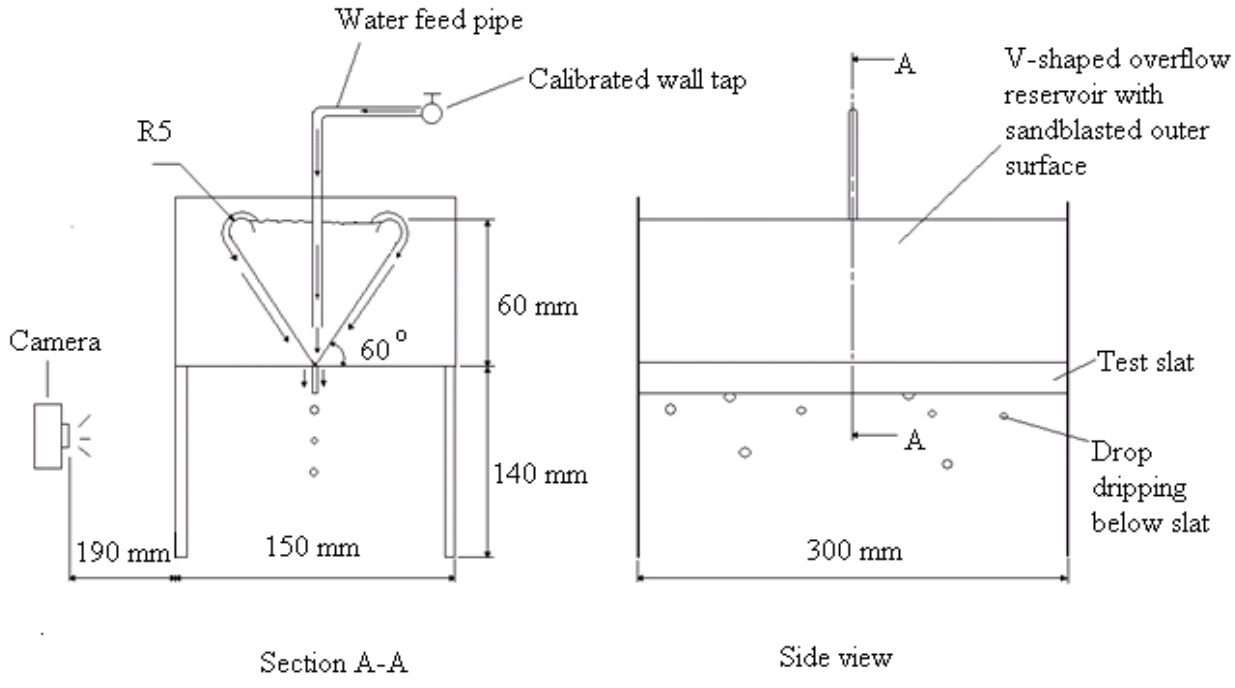

Figure D.1 : Apparatus for dripping experiments on slats

An even distribution of water onto the slat is achieved by a rounded reservoir edge and a sandblasted outer surface.

E

CALIBRATION DATA

E.1 Water flow pressure transducer calibration

A FOXBORO pressure transducer, model number: 843 DP-H2I and reference number: 536 3210 EW, is used to measure the pressure difference over the venturi flow meter used to measure the water flow rate. The pressure range of the transducer is 0 – 75 kPa. The pressure transducer was calibrated by Viljoen [2006VI1] using a mercury manometer and the calibration curve is given by

$$p_w = 15.996 V_{wp} - 16.006\,, kPa \qquad \text{(E.1)}$$

The calibration curve for the pressure transducer is given in figure E.1

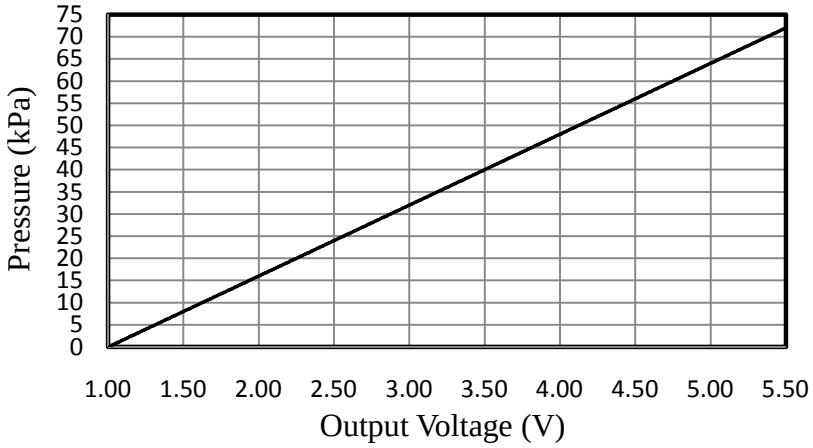

Figure E.1 : Calibration curve for FOXBORO pressure transducer

E.2 Water flow venturi calibration

The venturi flow meter used for the water flow measurement in the cooling tower test facility is also calibrated. This is done by measuring the volume of water that passes through the venturi for a specific pressure drop. The water is collected in a 500 litre tank and for each point the time is taken in which the water risen between two level markers. Three time measurements are taken for every flow rate and the average of the three measurements is used

to calculate the flow rate for each pressure difference. The pressure difference over the venturi is measured with the FOXBORO pressure transducer described in the previous section.

The theoretical flow rates for the venturi flow meter at each differential pressure measurement are also calculated. The Bernoulli equation is applied to determine the theoretical flow rate for a specific pressure difference which does not take the vena contracta and boundary layer effects into account. For a vertically placed venturi meter the flow rate from the energy equation is given by

$$\dot{V} = \left\{ \frac{2g\left[\frac{p_1 - p_2}{\gamma} + z_1 - z_2\right]}{A_2^{-2} - A_1^{-2}} \right\}^{\frac{1}{2}} \tag{E.2}$$

In equation (E.2) position 1 is located in the pipe section of the venturi and position 2 is located in the throat section.

The pressure drop between the two points in the venturi can be calculated by

$$p_1 - p_2 = \Delta p_{measured} - \rho_w g(z_1 - z_2) \tag{E.3}$$

By substituting equation (E.3) into equation (E.2), a formula for volumetric flow rate in terms of the measured pressure drop over the venturi can be obtained.

$$\dot{V} = \left\{ \frac{2g\left(\frac{\Delta p_{measured}}{\gamma}\right)}{A_2^{-2} - A_1^{-2}} \right\}^{\frac{1}{2}} \tag{E.4}$$

The above relation is not completely correct, because the boundary layer and vena contracta effects cause higher velocities in the throat therefore leading larger differential pressure measurements for a given flow rate. White [1999WH1] introduces a discharge coefficient to the Bernoulli equation and expresses the flow rate in terms of pressure drop through the venturi as given by equation (E.5). In this equation $\Delta p_{measured}$ is equal to the measured pressure difference over the venturi.

$$\dot{V} = C_d A_t \left[\frac{2\left(\frac{\Delta p_{measured}}{\rho_w}\right)}{1-\beta^4} \right]^{\frac{1}{2}} \tag{E.5}$$

In equation (E.5), C_d is the discharge coefficient of the venturi and A_t is the cross sectional area of the throat of the venturi. The discharge coefficient can be calculated according to a correlation by White that is given by

$$C_d = 0.9858 - 0.196\beta^{4.5} \tag{E.6}$$

where $\beta = D_2/D_1$

The previous two flow models together with the measured flow rates for the venturi can be seen in figure E.2.

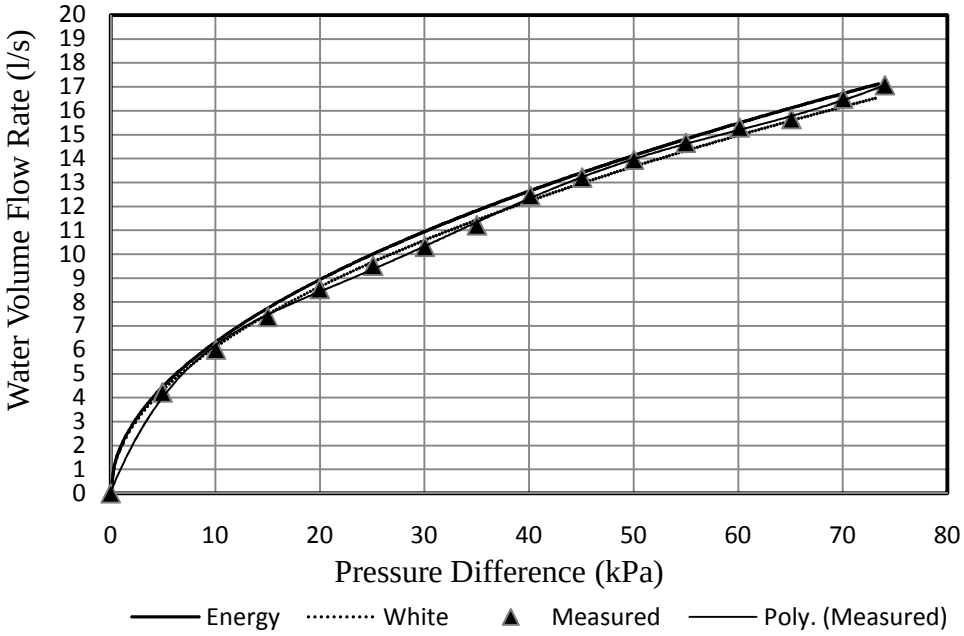

Figure E.2 : Venturi calibration curve

Equation (E.7) correlates the measurement data for the volumetric flow rate through the venturi as a function of differential pressure.

$$\dot{V} = -1.340645542230 \cdot 10^{-27}(\Delta p_w)^6 + 3.829686684565 \cdot 10^{-22}(\Delta p_w)^5 - 4.236562254726 \cdot 10^{-17}(\Delta p_w)^4 + 2.291537386143 \cdot 10^{-12}(\Delta p_w)^3 - 6.377928992492 \cdot 10^{-8}(\Delta p_w)^2 + 1.059557389791 \cdot 10^{-3}(\Delta p_w) + 5.985310316555 \cdot 10^{-2}\ , l/s \quad \text{(E.7)}$$

Figure E.3 shows the accuracy of the different methods for predicting the volumetric flow rate through the venturi flow meter.

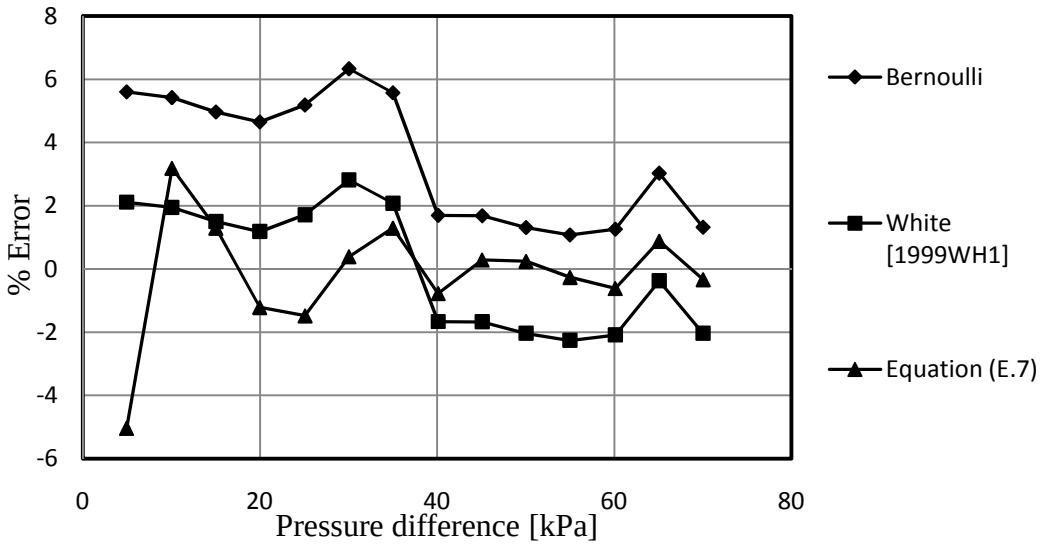

Figure E.3: Errors in flow rate prediction relative to measured flow rate

E.3 Air flow venturi calibration

The air flow measurement in the indoor cooling tower test facility is done by measuring the pressure drop over the flow nozzle that is situated below the fan as shown in figure 2.1. Viljoen [2006VI1] calibrated the venturi air flow meter and obtained an expression which gives the air velocity at the throat of the venturi in terms of the differential pressure measured over the venturi when air passes through. This is given by equation (E.8).

$$v_{vt} = c_n \left[\frac{2 \cdot \Delta p}{\rho_a \kappa}\right]^{0.5} \quad \text{(E.8)}$$

In equation (E.8), κ is the area ratio of the venturi throat to the plenum chamber and can be expressed as shown in equation (E.9). The venturi has a throat diameter of 0.455 m. The constant c_n is a calibration correction factor and is equal to 0.96.

$$\kappa = 1 - \left[\frac{A_{vt}}{A_{pl}}\right]^2 \tag{E.9}$$

Equations (E.8) and (E.9) can now be used to calculate the volumetric air flow rate through the tower as well as the mass flow rate. This is illustrated in equations (E.10) and (E.11) which give the volumetric flow rate and mass flow rate of the air through the venturi.

$$\dot{Q} = A_{vt} \cdot v_{vt} \tag{E.10}$$

$$m_a = \rho_a A_{vt} v_{vt} \tag{E.11}$$

If air density is taken to be 1.23 kg/m^3, the mass flow through the venturi against pressure drop over the venturi is shown in figure E.4. The pressure drop over the venturi is measured with a Betz water manometer during testing.

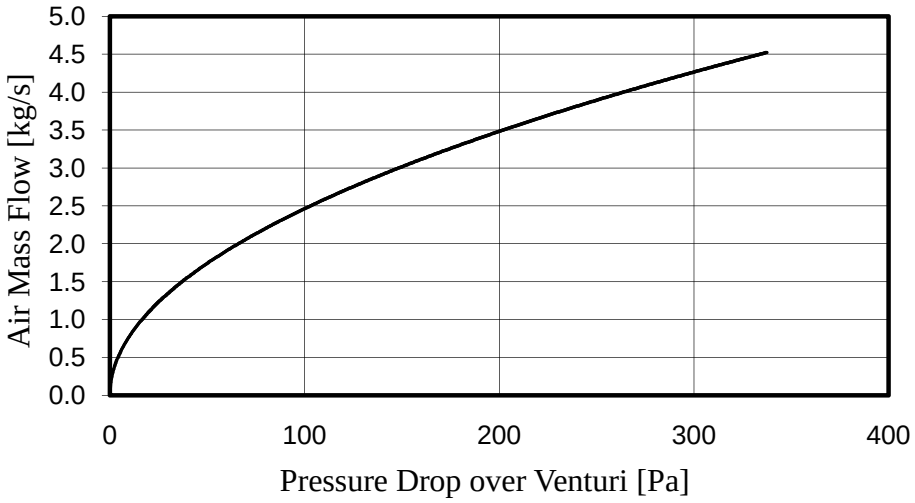

Figure E.4 : Mass flow through air flow venturi for an air density of 1.23 kg/m^3

E.4 Calibration of drop size measurement system

Figure E.5 shows the setup for the camera calibration.

The camera lens is 450 mm away from the closest drops that pass in front of the lens and 550 mm from the furthest drops.

Since drops of a given diameter appear larger on an image when they are closer to the camera lens than further away, this needs to be calibrated. The calibration is done by photographing a grid of 10 mm x 10 mm blocks, with a ruler placed on one of the horizontal lines of the grid to determine the length of the horizontal distance photographed. The distortion of the camera can be checked in this way and the horizontal distances photographed at 450 mm and 550 mm can be read from the photograph and corresponds to186 mm and 224 mm respectively. The photograph consist out of 3008 x 2000 pixels and the length calibration value of a single pixel at 450 mm and 550 mm is calculated and are 0.0618 mm/pixel and 0.0745 mm/pixel respectively. The average value between these two values are used as the calibration value in the drop size measurements being, 0.0682 mm/pixel and when this value is squared it gives the area represented by each pixel being, 0.0046 mm/pixel.

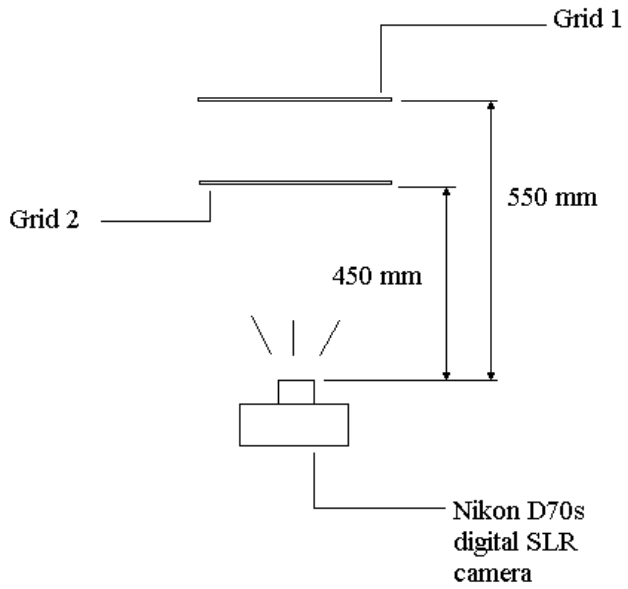

Figure E.5 : Setup for the calibration of the Nikon D70S camera

In order to gain a better understanding of the possible error when using the average calibration a photograph is analysed with all three of the above calibration values to evaluate the variation in the results. Figure E.6 shows the cumulative mass distribution directly under a trickle fill for a water flow of 2.84 kg/m^{2}s with no air flow and the three different calibration values.

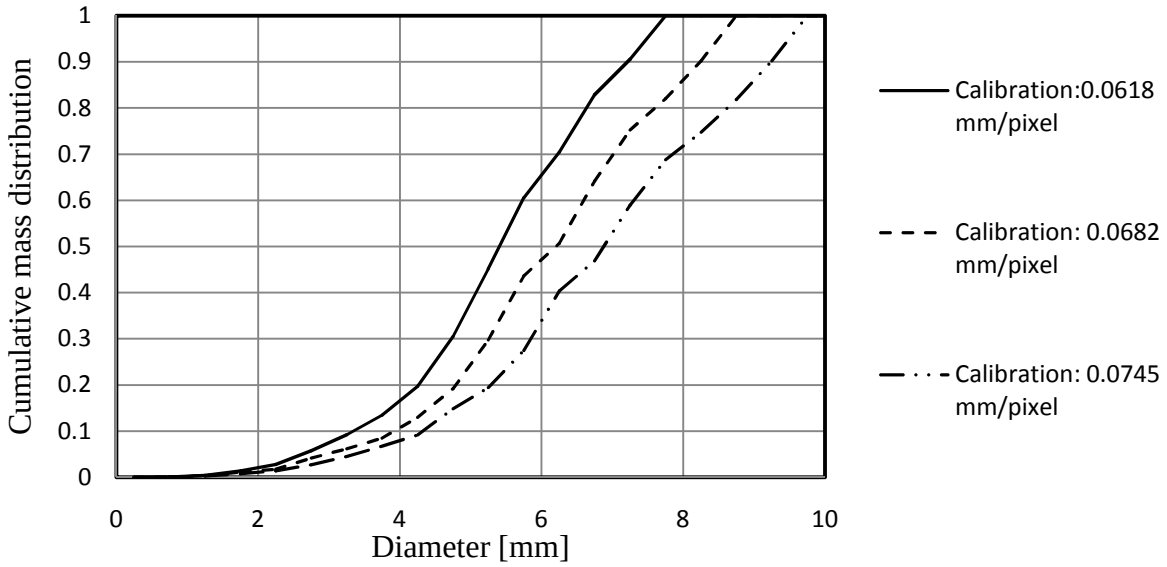

Figure E.6 : Cumulative mass distribution results for different calibration values, G_w = 2.84 kg/m^{2}s

The Sauter mean diameters for the three cases of figure E.6 are 4.73 mm, 5.19 mm and 5.71 mm respectively.

F

USER MANUAL AND INSTRUCTIONS

In this appendix the usage of the software program that is developed to analyse the drop images captured in the cooling tower test section is illustrated.

F.1 Opening screen of the software program

When the program is opened the main window appears from which all the operations can be launched. The image files are loaded from the "File Exchange" group and the image processing parameters set in the "Filter Parameters" group. The results of the image processing and drop counting operations can be viewed from the "Visualization" group. The main window is shown in figure F.1.

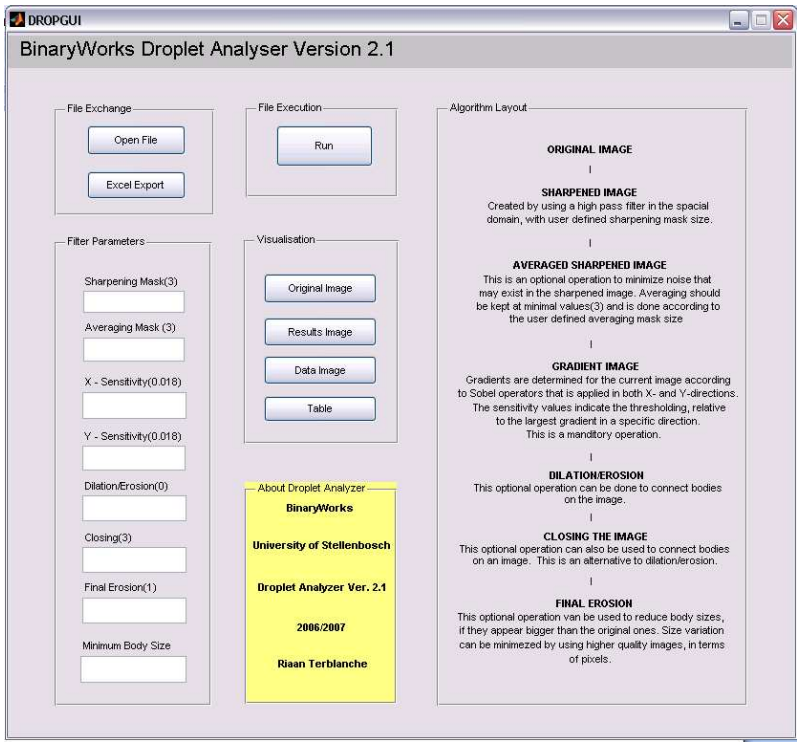

Figure F.1 : Opening screen

F.2 Load an image into the program

An image can be loaded into the program by clicking on the “Open File” button in the “File Exchange” group. A menu will appear from where the file selection can be done. This can be seen in figure F.2.

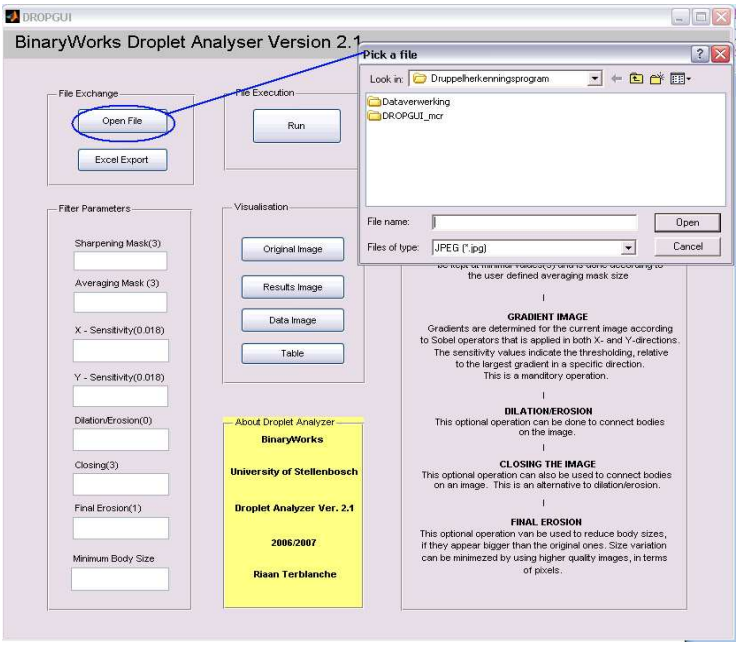

Figure F.2 : Load an image into the program

F.3 Setting the image processing parameters

The image processing parameters can be adjusted in the “Filter Parameters” group. The first image processing step is the implementation of a high pass filter in the spatial domain. The size of the spatial domain filter can be adjusted in the “Sharpening Mask” tab. A mask size of 5 is suggested here, which means that a spatial domain mask size of 5 x 5 pixels will be used to filter out low frequency components in an image. High frequency areas are associated with fast changing colour and correspond to the drop edges. An increasing mask size means that an increasing amount of slow colours is filtered out until only the sharp edges are left in the image, but it also means that computation time increases.

When the high pass filtering is done an averaging operation is performed on the image to even out undesired spots that might be present and could be picked up as an edge. A mask size of 3 is suggested for this operation and is set in the “Averaging Mask Size” tab. This means that a spatial domain filter size of 3 x 3 pixels will be applied to the image. The effect of making the

mask size larger is that the image becomes more blurred. The averaging mask size must always be smaller than the sharpening mask size to ensure that result is sharper than the original image.

After the preparation operations the drop edges must be detected and this is done by applying a Sobel edge detection filter to the image. The Sobel edge detection filter is applied in the vertical and horizontal direction after which the absolute values at each pixel are determined for both results. The maximum value in each of these images is determined and binary images are created according to the X- and Y-sensitivity values for both images. A value of 0.011 is suggested for both the sensitivity parameters, which means that all the gradients larger than 1.1% of the largest gradient found, will be kept and all the others filtered out. This means that the smaller the sensitivity values are chosen the more sensitive the results are to colour changes.

After the edges in the vertical and horizontal directions are detected, the two results are combined to give a single image where only the edges of the drops are present.

It can sometimes happen that a drop edge is disconnected at some places. If this is detected in the result image after the image processing is completed, the problem may be overcome by making use of dilation and erosion operations. By putting values in the “Dilation/Erosion” tab the user can make use of this type of operation to connect the discontinuities in drop edges. According to the user values a number of pixels are added around the edges of every body in the binary image which causes the bodies that lay close to each other to become connected. The edges of these connected bodies are then eroded by the same amount and the places of discontinuity are filled. The larger the dilation/erosion values are chosen the more connected the bodies in the results will become. A starting value of 1 is suggested for this operation and can be increased until the user is satisfied with the results.

Another way of connecting disconnected bodies is by using a closing operation. This operation fuses narrow breaks and eliminates small holes in the drop edges. This can be used as an alternative to dilation and erosion. Larger values will give smooth drop edges but can cause too many connected bodies in the result. A starting value of 1 is suggested for this operation and the number can again be increased until the user is satisfied with the results.

When the image processing operations are completed the drops in the image may look bigger than in the original image. This problem can be overcome by eroding the edges of the drops until they are the right sizes. It is up to the user to inspect the results to see if the drop detection is accurate and by increasing the number in the “Final Erosion” tab the desired accuracy can be achieved. A value of 3 gives excellent results.

The user can also specify a minimum body size in pixels that must be present in the end results. This is handy when noise pixels are present in the results and must be ignored.

The “Dilation”, “Closing” and “Final Erosion” operations are ignored when a value of zero are provided in these tabs.

The location where the image processing parameters are set can be seen in figure F.3.

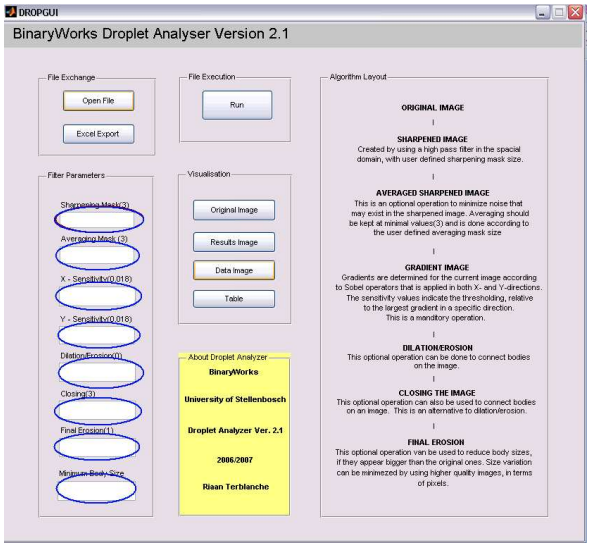

Figure F.3 : Setting the filter parameter values

F.4 Run the program

When an image is loaded into the program and all the necessary filter parameters are provided the program will allow the user to run the program. This can be done by clicking on the “Run” button in the “File Execution” group and is illustrated in figure F.4.

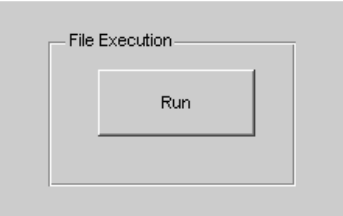

Figure F. 4 : Run the program

F.5 View the results

When the image processing operations are completed and the drops are counted, the results can be viewed by clicking on the different buttons in the “Visualization” program group. The original image can be viewed here and also the results image that show the detected drops as white blobs on a black background. In the data image, the drops of the results image are numbered and their locations as well as their sizes in pixels can be compared with the values in the table.

The visualization of the results is illustrated in figure F.5.

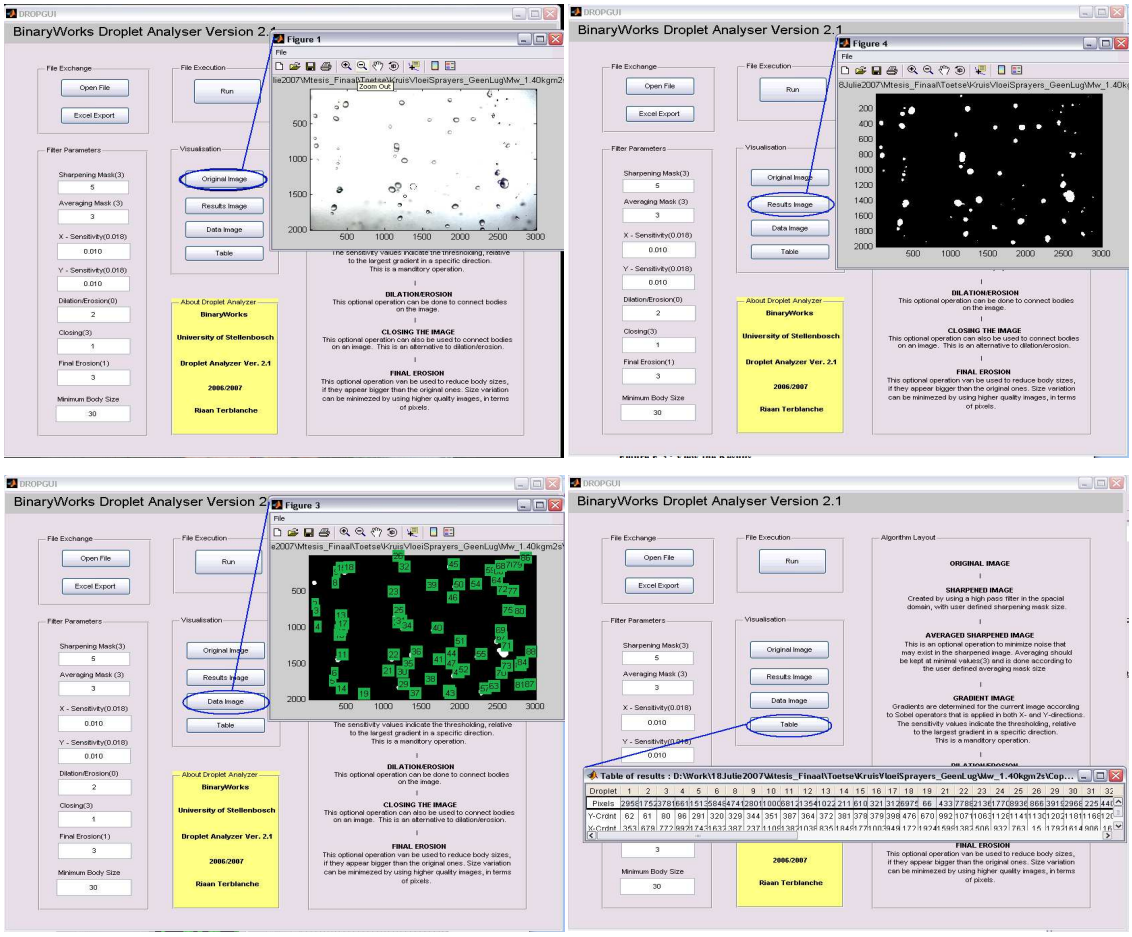

Figure F.5 : Visualization of results

F.6 Export data to Excel

When the user is satisfied with the results, the data can be exported to Microsoft Excel. This can be done by clicking on the “Excel Export” button in the File Exchange program group.

By doing this the data will be put into a spreadsheet from where the program can open Excel and do the necessary copying if the Excel button is clicked. This is illustrated in figure F.6.

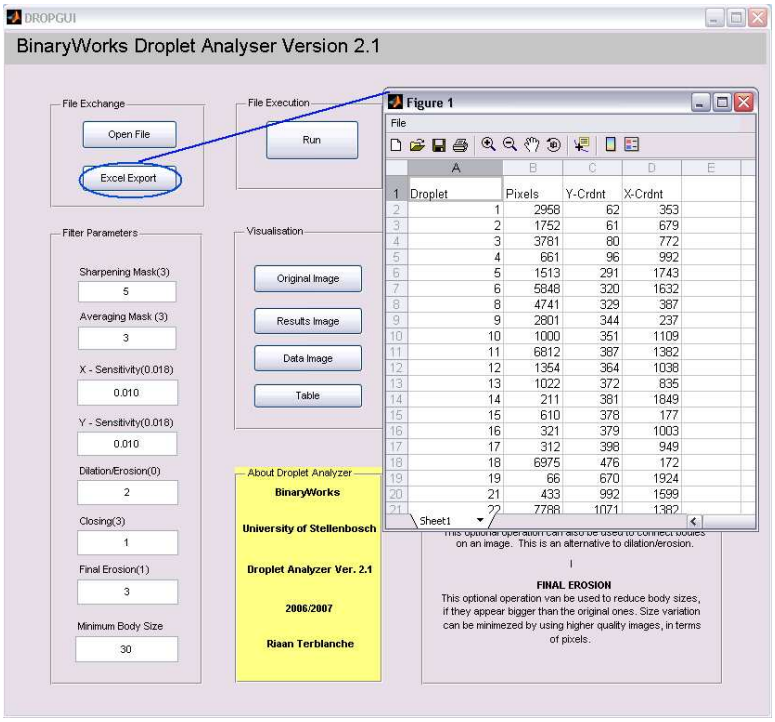

Figure F.6 : Export to Excel

G

MEASURED DATA

Table G.1 : Cumulative mass distributions right below film fill.

G_a [kg/m^{2}s]	1.22			1.71			2.28			2.85		
G_w [kg/m^{2}s]	1.4	2.84	4.2	1.4	2.84	4.2	1.4	2.84	4.2	1.4	2.84	4.2
d (mm)	R(d)	R(d)	R(d)	R(d)	R(d)	R(d)	R(d)	R(d)	R(d)	R(d)	R(d)	R(d)
0.25	0.0000124	0.0000000	0.0000025	0.0000427	0.0000007	0.0000005	0.0000031	0.0000052	0.0000012	0.0000015	0.0000027	0.0000012
0.75	0.0025311	0.0011376	0.0009522	0.0012472	0.0013459	0.0011371	0.0015680	0.0012865	0.0011863	0.0016959	0.0014208	0.0008393
1.25	0.0081670	0.0058001	0.0044069	0.0068236	0.0063281	0.0054424	0.0058757	0.0049537	0.0046093	0.0072991	0.0066507	0.0065419
1.75	0.0209656	0.0121969	0.0104393	0.0274477	0.0134077	0.0133180	0.0230690	0.0176800	0.0112393	0.0257493	0.0161163	0.0160449
2.25	0.0379666	0.0273033	0.0188647	0.0486576	0.0279357	0.0228830	0.0470496	0.0308895	0.0206334	0.0497130	0.0342872	0.0309272
2.75	0.0834923	0.0502874	0.0349164	0.0744741	0.0449875	0.0396190	0.0616441	0.0664920	0.0361770	0.0835218	0.0508753	0.0519993
3.25	0.1483916	0.0897434	0.0581000	0.1213491	0.0934618	0.0732495	0.0822930	0.1006146	0.0680271	0.1426108	0.1095487	0.0849511
3.75	0.1903694	0.1433615	0.1174572	0.1868117	0.1439061	0.1101515	0.1721675	0.1617698	0.1074410	0.2232967	0.1876642	0.1285406
4.25	0.2591150	0.2485621	0.1841137	0.2725763	0.2068479	0.1880430	0.2260389	0.2847075	0.1648159	0.3113878	0.2795094	0.1797127
4.75	0.3230985	0.3101526	0.2599392	0.3390960	0.2751932	0.2742880	0.3442253	0.3912378	0.2393925	0.3831280	0.3649923	0.2497248
5.25	0.4382856	0.4252963	0.3902402	0.3750218	0.4333867	0.3755470	0.4457730	0.4631563	0.3475442	0.4246409	0.5051436	0.3423258
5.75	0.5328678	0.5177418	0.5308590	0.4694198	0.5113241	0.5418381	0.5220085	0.6206325	0.4651348	0.5337192	0.6567794	0.4335694
6.25	0.6543314	0.6472541	0.6250768	0.6512602	0.6336539	0.6187171	0.5954354	0.7015256	0.5783931	0.5570658	0.7819646	0.5051770
6.75	0.7461369	0.7152325	0.7536548	0.7276157	0.7317178	0.6832807	0.6879321	0.7864440	0.6814346	0.6747059	0.8170084	0.5748808
7.25	0.8978105	0.8331564	0.8149315	0.9168383	0.7490763	0.6966141	0.8407478	0.8495768	0.7796482	0.7840308	0.8387197	0.6510890
7.75	0.9441275	0.9154668	0.8598410	0.9168383	0.8338898	0.8106203	0.8874136	0.9009877	0.8276351	0.8285440	0.8652398	0.7565885
8.25	1.0000000	0.9154668	0.9140155	0.9168383	0.8850452	0.8695601	1.0000000	0.9630049	0.8565785	0.9359369	0.9292224	0.8389361
8.75	1.0000000	0.9450820	0.9355600	1.0000000	0.9155609	0.9398788	1.0000000	1.0000000	0.9429065	1.0000000	0.9292224	0.8567990
9.25	1.0000000	0.9450820	0.9355600	1.0000000	0.9155609	0.9675706	1.0000000	1.0000000	0.9633043	1.0000000	0.9292224	0.8779023
9.75	1.0000000	0.9450820	0.9653675	1.0000000	1.0000000	1.0000000	1.0000000	1.0000000	0.9633043	1.0000000	0.9292224	0.9026162
10.25	1.0000000	0.9450820	1.0000000	1.0000000	1.0000000	1.0000000	1.0000000	1.0000000	0.9633043	1.0000000	0.9292224	0.9313304
10.75	1.0000000	1.0000000	1.0000000	1.0000000	1.0000000	1.0000000	1.0000000	1.0000000	0.9633043	1.0000000	1.0000000	0.9810175
11.25	1.0000000	1.0000000	1.0000000	1.0000000	1.0000000	1.0000000	1.0000000	1.0000000	1.0000000	1.0000000	1.0000000	1.0000000
11.75	1.0000000	1.0000000	1.0000000	1.0000000	1.0000000	1.0000000	1.0000000	1.0000000	1.0000000	1.0000000	1.0000000	1.0000000
12.25	1.0000000	1.0000000	1.0000000	1.0000000	1.0000000	1.0000000	1.0000000	1.0000000	1.0000000	1.0000000	1.0000000	1.0000000
12.75	1.0000000	1.0000000	1.0000000	1.0000000	1.0000000	1.0000000	1.0000000	1.0000000	1.0000000	1.0000000	1.0000000	1.0000000
13.25	1.0000000	1.0000000	1.0000000	1.0000000	1.0000000	1.0000000	1.0000000	1.0000000	1.0000000	1.0000000	1.0000000	1.0000000

Table G.2 : Cumulative mass distributions right below trickle fill.

G_a [kg/m^{2}s]	1.22			1.71			2.28			2.85		
G_w [kg/m^{2}s]	1.4	2.84	4.2	1.4	2.84	4.2	1.4	2.84	4.2	1.4	2.84	4.2
d (mm)	R(d)	R(d)	R(d)	R(d)	R(d)	R(d)	R(d)	R(d)	R(d)	R(d)	R(d)	R(d)
0.25	0.0000144	0.0000210	0.0000056	0.0000092	0.0000046	0.0000083	0.0000051	0.0000145	0.0000093	0.0000151	0.0000211	0.0000098
0.75	0.0015315	0.0023124	0.0005943	0.0015474	0.0011944	0.0010820	0.0010636	0.0010875	0.0017192	0.0023039	0.0020170	0.0011791
1.25	0.0079528	0.0080336	0.0047259	0.0095877	0.0052109	0.0073994	0.0076684	0.0096686	0.0080521	0.0124293	0.0105973	0.0076142
1.75	0.0167628	0.0188268	0.0150984	0.0171520	0.0137131	0.0210399	0.0252074	0.0228876	0.0236920	0.0234137	0.0255389	0.0185452
2.25	0.0296359	0.0306441	0.0248393	0.0265302	0.0237522	0.0421791	0.0450883	0.0457150	0.0335410	0.0453864	0.0486343	0.0346292
2.75	0.0574129	0.0534892	0.0379440	0.0803440	0.0494130	0.0565147	0.0791180	0.0665540	0.0436560	0.0754744	0.0714751	0.0465931
3.25	0.0821012	0.0974830	0.0673004	0.1126448	0.0695829	0.0910990	0.1240547	0.1274114	0.0714829	0.1127228	0.1062767	0.0735223
3.75	0.1091911	0.1425381	0.0934091	0.1436574	0.1098631	0.1414306	0.2160960	0.1883820	0.1199299	0.1699432	0.1641936	0.1369537
4.25	0.2196087	0.2128098	0.1625120	0.2158894	0.2045826	0.2065576	0.2830884	0.2830542	0.1821575	0.2347290	0.2420180	0.2212616
4.75	0.3407291	0.3305366	0.2396912	0.2789161	0.3179288	0.3372599	0.3999980	0.4069646	0.3095747	0.3897808	0.4502641	0.3501729
5.25	0.4447976	0.4806602	0.3634371	0.3980538	0.4454619	0.4676970	0.5262786	0.5185001	0.4034137	0.4944560	0.6091880	0.4636874
5.75	0.5424577	0.5618728	0.4832299	0.4874948	0.6241835	0.5483403	0.6092317	0.6796878	0.5164247	0.5632166	0.6894929	0.6227639
6.25	0.6929571	0.6363687	0.6041037	0.7172172	0.7819760	0.6907394	0.6891287	0.7737782	0.6087802	0.6220853	0.7101185	0.6866038
6.75	0.8825430	0.6926747	0.7425275	0.7895633	0.8542571	0.8211989	0.8568740	0.8685997	0.7749820	0.6962429	0.7620833	0.8152757
7.25	1.0000000	0.8322110	0.8111352	0.8792064	0.8990385	0.8616117	0.8984443	0.9567190	0.8779515	0.6962429	0.8264724	0.8949936
7.75	1.0000000	0.9174324	0.8530372	0.9339557	0.8990385	0.8862936	1.0000000	0.9567190	0.9031068	0.8646038	0.9051232	0.9436811
8.25	1.0000000	0.9517000	0.8783104	1.0000000	0.8990385	0.9160676	1.0000000	1.0000000	0.9637967	1.0000000	1.0000000	0.9436811
8.75	1.0000000	0.9517000	0.9084630	1.0000000	0.8990385	0.9160676	1.0000000	1.0000000	1.0000000	1.0000000	1.0000000	0.9436811
9.25	1.0000000	1.0000000	0.9440855	1.0000000	0.9455413	1.0000000	1.0000000	1.0000000	1.0000000	1.0000000	1.0000000	0.9436811
9.75	1.0000000	1.0000000	0.9440855	1.0000000	1.0000000	1.0000000	1.0000000	1.0000000	1.0000000	1.0000000	1.0000000	0.9436811
10.25	1.0000000	1.0000000	0.9440855	1.0000000	1.0000000	1.0000000	1.0000000	1.0000000	1.0000000	1.0000000	1.0000000	1.0000000
10.75	1.0000000	1.0000000	1.0000000	1.0000000	1.0000000	1.0000000	1.0000000	1.0000000	1.0000000	1.0000000	1.0000000	1.0000000
11.25	1.0000000	1.0000000	1.0000000	1.0000000	1.0000000	1.0000000	1.0000000	1.0000000	1.0000000	1.0000000	1.0000000	1.0000000
11.75	1.0000000	1.0000000	1.0000000	1.0000000	1.0000000	1.0000000	1.0000000	1.0000000	1.0000000	1.0000000	1.0000000	1.0000000
12.25	1.0000000	1.0000000	1.0000000	1.0000000	1.0000000	1.0000000	1.0000000	1.0000000	1.0000000	1.0000000	1.0000000	1.0000000
12.75	1.0000000	1.0000000	1.0000000	1.0000000	1.0000000	1.0000000	1.0000000	1.0000000	1.0000000	1.0000000	1.0000000	1.0000000
13.25	1.0000000	1.0000000	1.0000000	1.0000000	1.0000000	1.0000000	1.0000000	1.0000000	1.0000000	1.0000000	1.0000000	1.0000000

Table G.3 : Cumulative mass distributions right below fibre cement fill

G_a [kg/m^{2}s]	1.22			1.71			2.28			2.85		
G_w [kg/m^{2}s]	1.4	2.84	4.2	1.4	2.84	4.2	1.4	2.84	4.2	1.4	2.84	4.2
d (mm)	R(d)	R(d)	R(d)	R(d)	R(d)	R(d)	R(d)	R(d)	R(d)	R(d)	R(d)	R(d)
0.25	0.0000881	0.0000292	0.0000301	0.0000411	0.0000187	0.0000228	0.0000515	0.0000237	0.0000124	0.0000582	0.0000200	0.0000133
0.75	0.0066102	0.0026278	0.0028935	0.0043080	0.0026439	0.0020639	0.0043163	0.0035799	0.0014714	0.0037568	0.0021471	0.0016856
1.25	0.0174536	0.0117985	0.0099920	0.0141046	0.0100029	0.0069388	0.0107577	0.0132475	0.0053754	0.0117115	0.0080868	0.0057179
1.75	0.0330175	0.0250572	0.0196138	0.0277660	0.0194875	0.0180517	0.0222850	0.0279561	0.0125171	0.0250301	0.0188095	0.0130944
2.25	0.0466382	0.0446104	0.0310857	0.0446252	0.0344437	0.0281116	0.0402515	0.0452614	0.0298643	0.0423288	0.0343066	0.0237552
2.75	0.0892700	0.0582604	0.0520309	0.0736965	0.0486907	0.0448817	0.0596351	0.0687034	0.0509792	0.0681700	0.0509503	0.0495169
3.25	0.1068624	0.0981233	0.0881071	0.0991010	0.0702476	0.0646542	0.0916304	0.1006682	0.0760298	0.1108246	0.0784230	0.0778657
3.75	0.1383918	0.1140981	0.1250536	0.1381270	0.1063736	0.0889535	0.1143154	0.1575254	0.1228780	0.1472275	0.1185161	0.1010919
4.25	0.1711758	0.1683588	0.2057283	0.1949373	0.1852567	0.1302215	0.1583455	0.1989090	0.1691545	0.1896210	0.1615209	0.1391286
4.75	0.2535607	0.2170572	0.2995861	0.2478123	0.2892665	0.2001813	0.2044480	0.2724412	0.2201595	0.2414081	0.1958287	0.1804308
5.25	0.3029988	0.2828095	0.3819583	0.2954067	0.3883962	0.2835279	0.2459464	0.3149910	0.2752529	0.2713750	0.2653121	0.2481466
5.75	0.3517123	0.3499976	0.4901780	0.3892002	0.5403376	0.4295278	0.3958766	0.3988433	0.3898563	0.4551025	0.3261698	0.3004786
6.25	0.5393874	0.4486076	0.5757023	0.4494255	0.6657750	0.5607741	0.5534110	0.5663517	0.5060471	0.6404878	0.4434011	0.3811250
6.75	0.7495356	0.5883553	0.7238393	0.7528918	0.7711183	0.6552498	0.6416102	0.7020026	0.6426563	0.7041784	0.5910787	0.4827163
7.25	0.9122808	0.7230353	0.8239602	0.8468973	0.8798932	0.7576807	0.7782184	0.7580305	0.7635641	0.8357090	0.6825716	0.5666367
7.75	0.9520392	0.8640444	0.9054915	1.0000000	0.9064667	0.7934289	0.9117113	0.8949058	0.8078706	0.8678417	0.7570769	0.6691450
8.25	1.0000000	0.8923944	0.9300794	1.0000000	0.9385225	0.8365520	0.9519695	0.9224246	0.8435019	0.9453654	0.7795459	0.7464301
8.75	1.0000000	0.9600409	0.9594143	1.0000000	0.9385225	0.8622763	1.0000000	0.9224246	0.9497778	0.9453654	0.7795459	0.8201946
9.25	1.0000000	1.0000000	0.9594143	1.0000000	0.9385225	0.9230582	1.0000000	1.0000000	1.0000000	1.0000000	0.8428858	0.8855544
9.75	1.0000000	1.0000000	1.0000000	1.0000000	0.9385225	0.9586486	1.0000000	1.0000000	1.0000000	1.0000000	0.9170622	0.9110683
10.25	1.0000000	1.0000000	1.0000000	1.0000000	1.0000000	1.0000000	1.0000000	1.0000000	1.0000000	1.0000000	0.9170622	1.0000000
10.75	1.0000000	1.0000000	1.0000000	1.0000000	1.0000000	1.0000000	1.0000000	1.0000000	1.0000000	1.0000000	0.9170622	1.0000000
11.25	1.0000000	1.0000000	1.0000000	1.0000000	1.0000000	1.0000000	1.0000000	1.0000000	1.0000000	1.0000000	0.9170622	1.0000000
11.75	1.0000000	1.0000000	1.0000000	1.0000000	1.0000000	1.0000000	1.0000000	1.0000000	1.0000000	1.0000000	0.9170622	1.0000000
12.25	1.0000000	1.0000000	1.0000000	1.0000000	1.0000000	1.0000000	1.0000000	1.0000000	1.0000000	1.0000000	0.9170622	1.0000000
12.75	1.0000000	1.0000000	1.0000000	1.0000000	1.0000000	1.0000000	1.0000000	1.0000000	1.0000000	1.0000000	1.0000000	1.0000000
13.25	1.0000000	1.0000000	1.0000000	1.0000000	1.0000000	1.0000000	1.0000000	1.0000000	1.0000000	1.0000000	1.0000000	1.0000000

Table G.4 : Cumulative mass distribution immediately below designed slat grid

G_w = 2.84 kg/m^{2}s with no air																					
		Single Layer						Two Layers						Three Layers							
H_{fg} [m]		0.2	0.4	0.6	0.8	1.0		0.2	0.4	0.6	0.8	1.0		0.2	0.4	0.6	0.8	1.0			
d (mm)		R(d)	R(d)	R(d)	R(d)	R(d)		R(d)	R(d)	R(d)	R(d)	R(d)		R(d)	R(d)	R(d)	R(d)	R(d)			
0.25		0.0000000	0.0000000	0.0000000	0.0000000	0.0000000		0.0000000	0.0000000	0.0000000	0.0000000	0.0000000		0.0000000	0.0000000	0.0000000	0.0000000	0.0000000			
0.75		0.0082535	0.0145407	0.0234231	0.0167998	0.0287897		0.0140641	0.0189724	0.0229311	0.0221385	0.0202582		0.0104988	0.0173026	0.0160574	0.0192815	0.0219338			
1.25		0.0347924	0.0608886	0.0789618	0.0915851	0.1142292		0.0699297	0.0862747	0.0968815	0.0956637	0.0895629		0.0502484	0.0680503	0.0722828	0.0867711	0.0897880			
1.75		0.0855016	0.1275932	0.1798512	0.2095813	0.2330152		0.1539026	0.1876125	0.2069398	0.2128209	0.2001220		0.1225869	0.1456118	0.1608662	0.1857868	0.1762033			
2.25		0.1673460	0.2093846	0.2929454	0.3215259	0.3293500		0.2541512	0.2965498	0.3070842	0.3329117	0.3074925		0.2018620	0.2474476	0.2492494	0.2881226	0.2554400			
2.75		0.2487192	0.3146293	0.3920588	0.4131020	0.4112283		0.3539874	0.3937206	0.4085151	0.4567877	0.4049972		0.2742318	0.3311163	0.3313662	0.3695673	0.3231753			
3.25		0.3415205	0.3850567	0.4765856	0.4788233	0.4612845		0.4295177	0.4689052	0.4922279	0.5365327	0.4778460		0.3629191	0.3924971	0.3959866	0.4344127	0.3935721			
3.75		0.4015458	0.4607894	0.5477931	0.5494954	0.5035771		0.5314822	0.5574533	0.5565272	0.6119193	0.5220892		0.4268686	0.4691097	0.4516741	0.5024422	0.4571853			
4.25		0.4616188	0.5237862	0.6514501	0.5886869	0.5539488		0.6389660	0.5966837	0.6402751	0.6576445	0.5713401		0.5118651	0.5248722	0.5186403	0.5484208	0.4880526			
4.75		0.5836080	0.6190647	0.7621143	0.6639199	0.5930174		0.7104219	0.6827496	0.7021739	0.7023301	0.6348098		0.5853232	0.5488260	0.5580050	0.5829848	0.5225276			
5.25		0.6865513	0.7279178	0.8425703	0.7377958	0.6352177		0.7683096	0.7461347	0.7857494	0.7368069	0.6705166		0.6463588	0.6135105	0.5912237	0.6296531	0.5865310			
5.75		0.8082726	0.8449261	0.8727710	0.8348531	0.6490783		0.8316864	0.7738929	0.8223496	0.7934259	0.6986634		0.7365702	0.7409833	0.6610517	0.7435187	0.6323966			
6.25		0.9124831	0.8950139	0.9697311	0.8971742	0.7558777		0.9130757	0.8986587	0.8850194	0.8806789	0.8071027		0.8781652	0.9183271	0.7955624	0.8447531	0.7992831			
6.75		1.0000000	0.9160459	0.9697311	0.9756808	0.7783004		0.9745920	0.9660169	0.9639653	0.9722736	0.8829928		0.9754574	0.9526967	0.9650071	0.9297705	0.9353137			
7.25		1.0000000	0.9681671	1.0000000	1.0000000	0.9172194		1.0000000	0.9660169	0.9639653	0.9722736	0.9770275		0.9754574	0.9739902	1.0000000	1.0000000	0.9812829			
7.75		1.0000000	1.0000000	1.0000000	1.0000000	0.9511571		1.0000000	1.0000000	0.9639653	1.0000000	1.0000000		1.0000000	1.0000000	1.0000000	1.0000000	1.0000000			
8.25		1.0000000	1.0000000	1.0000000	1.0000000	0.9511571		1.0000000	1.0000000	1.0000000	1.0000000	1.0000000		1.0000000	1.0000000	1.0000000	1.0000000	1.0000000			
8.75		1.0000000	1.0000000	1.0000000	1.0000000	1.0000000		1.0000000	1.0000000	1.0000000	1.0000000	1.0000000		1.0000000	1.0000000	1.0000000	1.0000000	1.0000000			
9.25		1.0000000	1.0000000	1.0000000	1.0000000	1.0000000		1.0000000	1.0000000	1.0000000	1.0000000	1.0000000		1.0000000	1.0000000	1.0000000	1.0000000	1.0000000			
9.75		1.0000000	1.0000000	1.0000000	1.0000000	1.0000000		1.0000000	1.0000000	1.0000000	1.0000000	1.0000000		1.0000000	1.0000000	1.0000000	1.0000000	1.0000000			
10.25		1.0000000	1.0000000	1.0000000	1.0000000	1.0000000		1.0000000	1.0000000	1.0000000	1.0000000	1.0000000		1.0000000	1.0000000	1.0000000	1.0000000	1.0000000			
10.75		1.0000000	1.0000000	1.0000000	1.0000000	1.0000000		1.0000000	1.0000000	1.0000000	1.0000000	1.0000000		1.0000000	1.0000000	1.0000000	1.0000000	1.0000000			
11.25		1.0000000	1.0000000	1.0000000	1.0000000	1.0000000		1.0000000	1.0000000	1.0000000	1.0000000	1.0000000		1.0000000	1.0000000	1.0000000	1.0000000	1.0000000			
11.75		1.0000000	1.0000000	1.0000000	1.0000000	1.0000000		1.0000000	1.0000000	1.0000000	1.0000000	1.0000000		1.0000000	1.0000000	1.0000000	1.0000000	1.0000000			
12.25		1.0000000	1.0000000	1.0000000	1.0000000	1.0000000		1.0000000	1.0000000	1.0000000	1.0000000	1.0000000		1.0000000	1.0000000	1.0000000	1.0000000	1.0000000			
12.75		1.0000000	1.0000000	1.0000000	1.0000000	1.0000000		1.0000000	1.0000000	1.0000000	1.0000000	1.0000000		1.0000000	1.0000000	1.0000000	1.0000000	1.0000000			
13.25		1.0000000	1.0000000	1.0000000	1.0000000	1.0000000		1.0000000	1.0000000	1.0000000	1.0000000	1.0000000		1.0000000	1.0000000	1.0000000	1.0000000	1.0000000			

Table G.5 : Cumulative mass distribution immediately below expanded metal grid

G_w = 2.84 kg/m^{2}s with no air											
		Single Layer				Two Layers					
	H_{fg} [m]	0.2	0.4	0.6		0.2	0.4	0.6	
d (mm)		R(d)	R(d)	R(d)		R(d)	R(d)	R(d)	
0.25		0.0000000	0.0000000	0.0000000		0.0000000	0.0000000	0.0000000	
0.75		0.0050951	0.0099103	0.0214170		0.0099713	0.0198705	0.0217355	
1.25		0.0287784	0.0450424	0.0956366		0.0503401	0.0893850	0.0841783	
1.75		0.0559216	0.0891856	0.1771001		0.1118211	0.1744335	0.1645493	
2.25		0.0919773	0.1333612	0.2623172		0.1805354	0.2593268	0.2284749	
2.75		0.1193222	0.1878994	0.3277632		0.2535476	0.3310262	0.2858756	
3.25		0.1611152	0.2348128	0.3909491		0.3112599	0.3902011	0.3190373	
3.75		0.2176128	0.2893505	0.4316539		0.3608034	0.4650629	0.3699799	
4.25		0.2961182	0.3432228	0.4635600		0.4329241	0.5078751	0.4158867	
4.75		0.3796236	0.3986412	0.5017405		0.5018152	0.5839458	0.4750470	
5.25		0.4853255	0.4734670	0.5618834		0.5662114	0.6573104	0.5149859	
5.75		0.5501314	0.5366632	0.6634743		0.6790153	0.7055032	0.5674573	
6.25		0.6452453	0.6088030	0.6779703		0.7755913	0.7673929	0.6460723	
6.75		0.7500843	0.7905538	0.7875352		0.8972493	0.8765414	0.7733996	
7.25		0.8614313	0.8327799	0.8780423		0.9160924	0.8958621	0.8961095	
7.75		0.9067679	0.9187446	0.9333192		0.9391092	0.9430623	0.9175223	
8.25		0.9614576	0.9602244	1.0000000		0.9668744	1.0000000	0.9691829	
8.75		0.9614576	0.9602244	1.0000000		1.0000000	1.0000000	1.0000000	
9.25		1.0000000	0.9602244	1.0000000		1.0000000	1.0000000	1.0000000	
9.75		1.0000000	0.9602244	1.0000000		1.0000000	1.0000000	1.0000000	
10.25		1.0000000	1.0000000	1.0000000		1.0000000	1.0000000	1.0000000	
10.75		1.0000000	1.0000000	1.0000000		1.0000000	1.0000000	1.0000000	
11.25		1.0000000	1.0000000	1.0000000		1.0000000	1.0000000	1.0000000	
11.75		1.0000000	1.0000000	1.0000000		1.0000000	1.0000000	1.0000000	
12.25		1.0000000	1.0000000	1.0000000		1.0000000	1.0000000	1.0000000	
12.75		1.0000000	1.0000000	1.0000000		1.0000000	1.0000000	1.0000000	
13.25		1.0000000	1.0000000	1.0000000		1.0000000	1.0000000	1.0000000	

Table G.6 : Cumulative mass distribution immediately below trickle fill with no air

No air						
G_w [kg/m^{2}s]	1.4		2.84		4.2	
d (mm)	R(d)		R(d)		R(d)	
0.25	0.0000102		0.0000103		0.0000042	
0.75	0.0012975		0.0015270		0.0008491	
1.25	0.0059802		0.0042496		0.0033701	
1.75	0.0205815		0.0125068		0.0112418	
2.25	0.0429254		0.0250422		0.0294930	
2.75	0.0746551		0.0525067		0.0461544	
3.25	0.1232883		0.0776923		0.0767122	
3.75	0.1692634		0.1086440		0.1072247	
4.25	0.3198473		0.1931250		0.1755589	
4.75	0.4366412		0.2481653		0.2566496	
5.25	0.5785664		0.4286448		0.3661381	
5.75	0.6200019		0.5681225		0.5184442	
6.25	0.6998198		0.7293294		0.6597060	
6.75	0.8338833		0.8195847		0.7555248	
7.25	1.0000000		0.8755018		0.8233694	
7.75	1.0000000		0.9096530		0.8648052	
8.25	1.0000000		0.9508498		0.9647737	
8.75	1.0000000		1.0000000		0.9647737	
9.25	1.0000000		1.0000000		1.0000000	
9.75	1.0000000		1.0000000		1.0000000	
10.25	1.0000000		1.0000000		1.0000000	
10.75	1.0000000		1.0000000		1.0000000	
11.25	1.0000000		1.0000000		1.0000000	
11.75	1.0000000		1.0000000		1.0000000	
12.25	1.0000000		1.0000000		1.0000000	
12.75	1.0000000		1.0000000		1.0000000	
13.25	1.0000000		1.0000000		1.0000000	

Table G.7 : Cumulative mass distribution for test facility sprayers, G_w = 2.84 kg/m^{2}s, No air

d(mm)	R(d)
0.25	0.0000000
0.75	0.0161096
1.25	0.0529006
1.75	0.0902098
2.25	0.1286915
2.75	0.1670148
3.25	0.2337872
3.75	0.3255646
4.25	0.4434475
4.75	0.6628815
5.25	0.7517652
5.75	0.8685396
6.25	0.9685150
6.75	1.0000000
7.25	1.0000000
7.75	1.0000000
8.25	1.0000000
8.75	1.0000000
9.25	1.0000000
9.75	1.0000000
10.25	1.0000000
10.75	1.0000000
11.25	1.0000000
11.75	1.0000000
12.25	1.0000000
12.75	1.0000000
13.25	1.0000000

Table G.8 : Cumulative mass distribution for 0.8m grid spacing test with and without air

G_w = 2.84 kg/m^{2}s									
		Single Layer 0.8m below Tricle Fill				Two Layers 0.8 m Spacing between Layers and Trickle Fill			
	G_a [kg/m^{2}s]	2.28		0		2.28		0	
d (mm)		R(d)		R(d)		R(d)		R(d)	
0.25		0.0000000		0.0000000		0.0000000		0.0000000	
0.75		0.0228553		0.0376660		0.0303931		0.0371737	
1.25		0.1082571		0.1424508		0.1327676		0.1452953	
1.75		0.2174845		0.2493584		0.2698223		0.2742892	
2.25		0.3069670		0.3702968		0.4092213		0.4033445	
2.75		0.3871139		0.4321899		0.5076650		0.4961306	
3.25		0.4456283		0.5315919		0.6047657		0.5827847	
3.75		0.5003433		0.5867336		0.6534725		0.6385081	
4.25		0.5913707		0.6484797		0.7110810		0.6520276	
4.75		0.6469692		0.7002016		0.7358277		0.6834849	
5.25		0.6898658		0.7700364		0.7775938		0.7344532	
5.75		0.7462229		0.8770759		0.8434400		0.8237353	
6.25		0.8005037		0.9752626		0.8716268		0.9097282	
6.75		0.9372601		1.0000000		0.9071341		1.0000000	
7.25		0.9655023		1.0000000		0.9731292		1.0000000	
7.75		1.0000000		1.0000000		1.0000000		1.0000000	
8.25		1.0000000		1.0000000		1.0000000		1.0000000	
8.75		1.0000000		1.0000000		1.0000000		1.0000000	
9.25		1.0000000		1.0000000		1.0000000		1.0000000	
9.75		1.0000000		1.0000000		1.0000000		1.0000000	
10.25		1.0000000		1.0000000		1.0000000		1.0000000	
10.75		1.0000000		1.0000000		1.0000000		1.0000000	
11.25		1.0000000		1.0000000		1.0000000		1.0000000	
11.75		1.0000000		1.0000000		1.0000000		1.0000000	
12.25		1.0000000		1.0000000		1.0000000		1.0000000	
12.75		1.0000000		1.0000000		1.0000000		1.0000000	
13.25		1.0000000		1.0000000		1.0000000		1.0000000	

H

SINGLE DROP SAMPLE CALCULATION

This Appendix provides the first iteration for the thermal and dynamic solution of a single drop falling in still air.

The initial conditions are given in table H.1. Although it is normally assumed that the initial drop velocity of a drop entering the rain zone is zero, it is chosen to be 0.5 m/s for the purpose this calculation in order to prevent division by zero errors in the drag coefficient calculation.

Table H.1 : Initial conditions for single drop sample calculation

Variable	Initial value
T_a [K]	298
T_{awb} [K]	295
p_{atm} [Pa]	101325
v_{dy0} [m/s]	0.5
Δt	0.0001
d_0 [mm]	6
T_{w0} [K]	323

H.1 Physical properties of the air at film temperature

H.1.1 Humidity ratio calculation at ambient condition

$w = 0.01645$ kg/kg dry air (A.14)

H.1.2 Air-vapour density calculation at $T_f = (T_a + T_{w0})/2$

$\rho_{av,T_f} = 1.12565$kg air-vapour/m^3 (A.10)

H.1.3 Viscosity calculation for air-vapour mixture at $T_f = (T_a + T_{w0})/2$

$\mu_{av,T_f} = 1.82051 \times 10^{-5}$ kg/ms (A.12)

H.1.4 Thermal conductivity for air-vapour mixture at $T_f = (T_a + T_{w0})/2$

$k_{av,T_f} = 0.02593$ W/mK (A.13)

H.1.5 Specific heat for air-vapour mixture at $T_f = (T_a + T_{w0})/2$

$c_{pav,T_f} =$ 1021.76541 J/K kg air-vapour (A.11)

H.1.6 Prandtl number for air-vapour mixture at $T_f = (T_a + T_{w0})/2$

$$Pr_{av} = \mu_{av}\frac{c_{pav}}{k_{av}} = 0.71735 \quad \text{(H.1)}$$

H.2 Physical properties of water at T_{w0}

H.2.1 Density of the water drop

$\rho_w(T_{w0}) =$ 988.21170 kg/m^3 (A.16)

H.2.2 Specific heat of the water drop

$c_{pw}(T_{w0}) = 4178.82202$ J/kgK (A.17)

H.2.3 Latent heat of vaporization

$i_{fgw} = 2383\,261.14283$ J/kg (A.20)

H.3 Heat transfer calculations

H.3.1 Reynolds number

$$Re_d = \frac{\rho_{av} v_{dy0}\left(\frac{d_0}{1000}\right)}{\mu_{av}} = 185.49399 \quad \text{(H.2)}$$

H.3.2 Nusselt number

$$Nu_d = 2 + 0.6 Re_d^{\frac{1}{2}} Pr_{av}^{\frac{1}{3}} = 9.31519 \quad \text{(3.19)}$$

H.3.3 Convection heat transfer coefficient

From equation (3.22)

$$h_c = k_{av}\, Nu_d / \left(\frac{d_0}{1000}\right) = 40.25843 \text{ W/m}^2\text{K} \quad \text{(H.3)}$$

$$A_s = 4\pi(d_0/2000)^2 = 1.13100 \times 10^{-4} \text{ m}^2 \quad \text{(H.4)}$$

$$\mathrm{Q}_{conv} = h_c A_s (T_{w0} - T_a) = 0.11383 \text{ W} \quad \text{(3.18)}$$

H.4 Mass and enthalpy transfer calculations

H.4.1 Diffusion coefficient

$$D_{AB}(\mathrm{T_a}, \mathrm{P_{atm}}) = 2.12559 \times 10^{-5} \text{ m}^2/\text{s} \quad (3.29)$$

H.4.2 Sherwood number

$$Sc = \mu_{av}/(\rho_{av} D_{AB}) \quad (H.5)$$

$$= 0.76087$$

$$Sh_d = 2 + 0.6 Re_d^{\frac{1}{2}} Sc^{\frac{1}{3}} = 9.46025 \quad (3.26)$$

H.4.3 Mass transfer coefficient

From equation (3.28)

$$h_d = Sh_d D_{AB} / \left(\frac{d_0}{1000}\right) = 0.03351 \text{ kg/m}^2\text{sK} \quad (H.6)$$

H.4.4 Saturated vapour density at drop surface

$$\rho_{vs}(T_{w0}) = 0.08243 \text{ kg/m}^3 \quad (A.9)$$

H.4.5 Vapour density of the cooling air

$$P_v = \frac{w P_{atm}}{0.622 + w} \quad (H.7)$$

$$= 2610.14728 \text{ Pa}$$

$$\rho_v = P_v/(R_v T_a) = 0.01898 \text{ kg/m}^3$$

R_v = 461.52 J/kgK

H.4.6 Mass transfer rate

$$m_e = -h_D A_S(\rho_{vs} - \rho_{v\infty}) = -2.40507 \times 10^{-7} \text{ kg/s} \quad (3.25)$$

H.5 Forces acting on moving drops

H.5.1 Drag force

$$C_{D.sphere} = 24 \frac{\left(1 + 0.173 {Re_D}^{0.657}\right)}{Re_D} + \frac{0.413}{\left(1 + 16300 {Re_D}^{-1.09}\right)} \quad (3.7)$$

$$= 0.82895$$

$$A_f = \pi \left(\frac{d_0}{2000}\right)^2 = 2.82743 \times 10^{-5} \text{ m}^2 \quad (H.8)$$

$$F_D = 0.5 C_{D,sphere} \rho_{av} {v_{dy0}}^2 A_f = 3.29787 \times 10^{-6} \text{ N} \quad (H.9)$$

H.5.2 Buoyancy force

$$V_d = \frac{4}{3}\pi \left(\frac{d_0}{2000}\right)^3 = 1.13097 \times 10^{-7} \text{ m}^3 \quad (H.10)$$

$$F_B = \rho_{av} V_d g = 1.24851 \times 10^{-6} \text{ N} \quad (H.11)$$

H.5.3 Weight

$$F_w = \rho_w V_d g \tag{H.12}$$
$$= 0.00110 \text{ N}$$

H.6 Calculation of variables at next time step

H.6.1 Temperature

$$m_e i_{fgw} = 0.57216 \text{ W}$$

$$\frac{dT}{dt} = \frac{-m_e i_{fg} - Q_{conv}}{M c_{pw}} \tag{3.17}$$
$$= -1.47100 \text{ K/s}$$

$$T_{w,i+1} = T_{w,i} + \frac{dT_w}{dt}\Delta t \tag{H.13}$$
$$= 322.99985 \text{ K}$$

H.6.2 Velocity

Equation (3.6) reduce to the following

$$\frac{\partial v_{dy}}{\partial t} = M^{-1}\left[(\rho_w V_d g - F_D - \rho_{av} V_d g) - v_{dy}\frac{\partial M}{\partial t}\right] \tag{3.6}$$
$$= 9.76740 \text{ m/s}^2$$

$$v_{dy,i+1} = v_{dy,i} + \frac{\partial v_{dy}}{\partial t}\Delta t \tag{H.14}$$
$$= 0.50098 \text{ m/s}$$

H.6.3 Trajectory

$$s_{dy,i+1} = s_{dy,i} + v_{dy,i}\Delta t + 0.5\frac{\partial v_{dy}}{\partial t}\Delta t^2 \tag{H.15}$$
$$= 5.00488 \times 10^{-5} \text{ m}$$

I

SAMPLE CALCULATION FOR PREDICTING THE DROP DISTRIBUTION BELOW A GRID OF HORIZONTAL SLATS

This appendix provides a sample calculation for the model used to predict the drop distribution obtained below a grid of slats for a given polydisperse drop distribution above the grid. Some of the input variables to the reduction model are provided in table I.1.

Table I.1 : Input values to drop size reduction model

Variable	Value
T_w [K]	298.15
T_a [K]	298.15
T_{awb} [K]	298.15
p_{atm} [Pa]	101325
G_a [kg/m^{2}s]	0
G_w [kg/m^{2}s]	2.84
A_f [m^2]	1.5
W [mm]	3
S [mm]	10
H_{fg} [m]	0.6
L [m]	1.5
σ [N/m]	0.072
ρ_d [kg/m^3]	997.04282
N_s [-]	77
d_i [mm]	5

I.1 Determine the number of *5 mm* drops that break

It can be determined from the distribution provided (figure 4.10) as an input to the model that the total mass flow of the 5 mm drops is 0.155822kg/s which equals 2388 drops/s. The number of drops that break through the grid can now be determined.

$$N_{bi} = N_i\left(\frac{N_s L(W + d_i)}{A_f}\right) \quad (4.24)$$

$$= 1471 \text{ drops/s}$$

This means that *917 drops/s* go unhindered through the grid.

I.2 Average water film thickness on the slats

$$\bar{\delta} = 0.33559 \text{ mm} \quad (4.10)$$

I.3 Average splash fraction

The velocity at which the drop impacts the slat can be determined from the model in chapter 3 and equals 3.34 m/s.

$$We = \frac{\rho_d v^2 d_i}{\sigma} = \frac{(997.73631 \cdot 3.34^2 \cdot 0.005)}{0.072} = 771.91097 \quad (4.3)$$

$$d_m = \sqrt{\frac{16\sigma}{g(\rho_d - \rho_{av})}} = 10.89240 \text{ mm} \quad (4.4)$$

The reference Weber number for the largest stable drop at STD

$$We_{ref} = \frac{\rho_w {v_T}^2 d_m}{\sigma} = \frac{1000 \cdot 9.18^2 \cdot 0.01089240}{0.072} = 12746.20050 \quad (4.3)$$

The average splash fraction can now be determined. The constants in equation (4.2) for a 3 mm slat can be determined by linear interpolation between the values for a 2 mm and 5 mm slat.

$$f_{s,2\,mm} = 0.34341 \quad (4.2)$$

$$f_{s,5\,mm} = 0.50969 \quad (4.2)$$

$$f_{s,3\,mm} = \left(\frac{3-2}{5-2}\right)(0.38604 - 0.25900) + 0.25900 = 0.39883$$

The cumulative mass distribution of the drops contained in the fraction of the drops that splash from the slats can be described by the Rosin Rammler equation.

The reference kinetic energy for the largest stable drop at STD is determined from

$$KE_{ref} = 0.5\left(\frac{\rho_w \pi {d_m}^3}{6}\right){v_T}^2 = 0.5 \cdot \left(\frac{1000 \cdot \pi \cdot 0.01089240^3}{6}\right) \cdot 9.18^2 \quad (4.8)$$

$$= \quad 0.02849 \text{ J}$$

and the kinetic energy at which the drop impact the slat is determined from

$$KE = 0.5\left(\frac{\rho_d \pi d^3}{6}\right){v_d}^2 = \ 0.5 \cdot \left(\frac{997.04282 \cdot \pi \cdot 0.005^3}{6}\right) 3.34^2 \quad (I.1)$$

$$= \quad 0.00036 \text{ J}$$

$$R(d) = 1 - exp\left(-\left(\frac{d}{d_{RR}}\right)^{n_{RR}}\right) \quad (4.5)$$

Equations (4.6) to (4.10) are solved to determine the variables needed for the resultant Rosin Rammler equation and the splash distribution for a 5 mm incoming drop is shown in figure I.1.

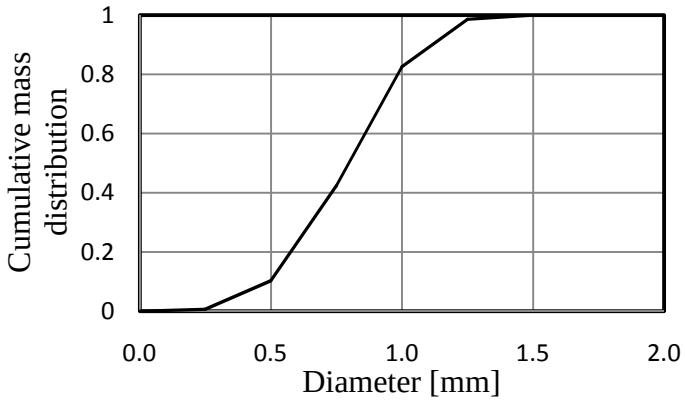

Figure I.1 : Splash distribution for a *5 mm* incoming drop

The data of figure I.1 is presented in table I.2.

Table I.2: Splash distribution for *5 mm* incoming drop

d [mm]	0	0.25	0.5	0.75	1.00	1.25	1.50	1.75
R(d)	0	0.00672	0.10284	0.42371	0.825501	0.98602	0.99986	1

I.4 Average cutting fraction and distribution

$$\bar{f_c} = \frac{d_i}{W + d_i} = 0.625 \tag{4.12}$$

The cumulative mass distribution of the drops contained in the cutting mass is given by Equation (4.17) and shown in figure I.2.

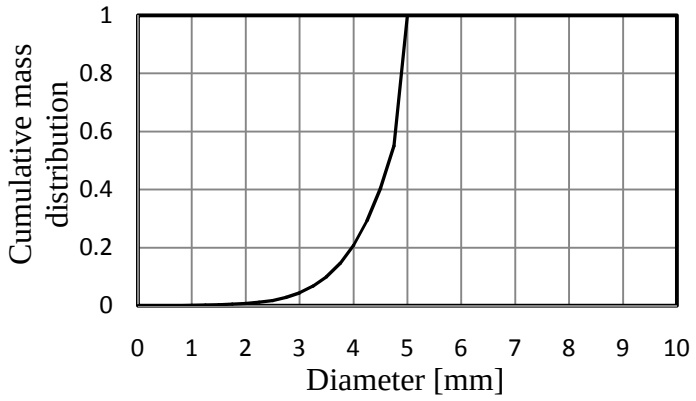

Figure I.2 : Cutting distribution for *5 mm* incoming drop

The data from figure I.2 is presented in table I.3

Table I.3 : Cutting distribution for 5 mm incoming drop

d[mm]	0	0.5	1	1.5	2	2.5	3	3.5	4	4.5	5
R(d)	0	0	0.0013	0.0036	0.0078	0.0184	0.0441	0.0998	0.2088	0.4053	1

I.5 Dripping fraction and distribution

The fraction of the mass that drip below the slats of the 5 mm drops that is subjected to breaking by the slats, can be obtained by doing a mass balance over the grid as given by equation (4.23). From this, the fraction of the total mass that drip below the slats can be determined.

The size of the primary drop dripping from below a *3 mm* slat is given by

$$d_p = C\sqrt{\frac{\sigma}{g(\rho_d - \rho_{av})}} \tag{4.21}$$

$$= 6.35701 \text{ mm}$$

where

$$C = 2.206 + \left(\frac{0.0597}{1.1 - S}\right) = 2.33484 \tag{4.22}$$

and S = 2/π

The satellite drops are linearly distributed between $0.24d_p$ and $0.46d_p$ and they have the following sizes

$d_{s,1}$ = 1.5256847 mm

$d_{s,2}$ = 1.8753207 mm

$d_{s,3}$ = 2.2249568 mm

$d_{s,4}$ = 2.5745929 mm

$d_{s,4}$ = 2.9242289 mm

J

SAMPLE CALCULATION FOR *e*-NTU METHOD IN DETERMINING THE MERKEL NUMBER FOR A CROSS FLOW RAIN ZONE

This Appendix provides a sample calculation for the determination of the Merkel number of a cross flow rain zone test section according to the *e*-NTU method.

J.1 Input values

Table J.1 provides the input variables for the problem.

Table J. 1 : Input variables for *e*-NTU method

Variable	Value
Atmospheric pressure (p_{atm})	101325 Pa
Inlet water temperature (T_{wi})	323 K
Outlet water temperature (T_{wo})	316.0275 K
Air temperature (T_{ai})	298 K
Wet bulb air temperature (T_{awb})	295.76 K
Section height (H)	2 m
Section width (B)	2 m
Section Length (L)	1.55 m
Air mass flux (G_a)	1.22 kg/m^{2}s
Water mass flux (G_w)	1.40 kg/m^{2}s

J.2 Heat transfer rate

J.2.1 Water mass flow rate

$$m_w = G_w BL \quad \text{(J.1)}$$

$$= 4.34 \text{ kg/s}$$

J.2.2 Specific heat of the water at $T_{wm} = (T_{wi} + T_{wo})/2$

$$c_{pwm} = 4177.7 \text{ J/kgK} \quad \text{(A.17)}$$

J.2.3 Heat transfer rate

$Q = m_w c_{pwm}(T_{wi} - T_{wo}) = 1.2642 \times 10^5$ W (5.10)

J.3 Enthalpy of saturated air at water outlet temperature

$i_{maswo} = 1.9269 \times 10^5$ J/kg dry air (A.15b)

J.4 Enthalpy of saturated air at water inlet temperature

$i_{maswi} = 2.7341 \times 10^5$ J/ kg dry air (A.15b)

J.5 Enthalpy of saturated air at water mean temperature

$T_{wm} = (T_{wi} + T_{wo})/2$ (J.5)

$i_{maswm} = 2.2946 \times 10^5$ J/kg dry air (A.15b)

J.6 Enthalpy of the inlet air

$i_{mai} = 6.6921 \times 10^4$ J/kg dry air (J.8)

J.7 Approximate the gradient of saturated air enthalpy

$$\frac{di_{masw}}{dT_w} = (i_{maswi} - i_{maswo})/(T_{wi} - T_{wo}) \quad \text{(J.9)}$$

$$= 1.1578 \times 10^4 \text{ J/K kg dry air}$$

J.8 Determine the case of the problem

$m_a = G_a HB = 4.88$ kg/s (J.10)

$m_w c_{pm}/(d_{imasw}/dT_w) = 1.5661 < m_a$

Therefore it is a case 1 problem

J.9 Determine the effectiveness for the case 1 problem

$C_{emin} = m_w c_{pw}/(di_{masw}/dT_w) = 1.5661$ (5.12)

$C_{emax} = m_a$ (5.13)

$C_e = C_{emin}/C_{emax} = m_w c_{pw}/[(di_{masw}/dT_w)m_a] = 0.3209$ (5.14)

J.9.1 Determine the correction factor for the Q_{max} approximation

$\lambda = (i_{maswo} + i_{maswi} - 2i_{masw})/4 = 1.7958 \times 10^3$ J/ kg dry air (5.15)

J.9.2 Effectiveness of the system

$$Q_{max} = C_{emin}(i_{maswi} - \lambda - i_{mai}) = 3.2057 \times 10^5 \text{ J/s} \quad (5.16)$$

$$e_e = \frac{\mathrm{Q}}{\mathrm{Q_{max}}} = 0.3944 \quad (5.9)$$

J.10 Determine the number of thermal transfer units (NTU_e)

The effectiveness of an evaporative cooler in cross flow configuration with unmixed streams can be expressed in terms of the number of transfer units as shown by

$$e_e = 1 - exp\left[NTU_e{}^{0.22}\{exp(-C_e NTU_e) - 1\}/C\right] \quad (5.17)$$

From equations (5.10) and (5.18) NTU_e can be determined iteratively

$$NTU_e = 0.5539$$

J.11 Merkel number

$$\frac{h_d a_{rz} H_{rz}}{m_w} = \frac{NTU_e c_{pwm}}{(di_{masw}/dT_w)} = 0.1999 \quad (5.18)$$

K

SAMPLE CALCULATION FOR THE PREDICTION OF CROSS FLOW PERFORMANCE

In this Appendix the heat and mass transfer for a rain zone is determined by making use of the Poppe method. The input variables for the model are provided in table K.1 followed by the calculation of the next grid point values for the first iteration.

Table K.1: Input variables to Poppe cross flow model

Variable	Value
Atmospheric pressure (p_{atm})	101325 Pa
Inlet water temperature (T_{wi})	323 K
Outlet water temperature (T_{wo})	316.0275 K
Air temperature (T_{ai})	298 K
Wet bulb air temperature (T_{awb})	295.77 K
Section height (H)	2 m
Section Length (L)	1.55 m
Air mass flux (G_a)	1.22 kg/m^{2}s
Water mass flux (G_w)	1.40 kg/m^{2}s
Step size (Δs)	0.01 m

K.1 Initial air conditions

$w = 0.0165$ kg/kg dry air (A.14)

$i_{mai} = 6.6959 \times 10^4$ J/kg dry air (A.15b)

K.2 Enthalpy of saturated air at water temperature (T_{wi})

$w_{sw} = 0.0860$ kg/kg dry air (A.14)

$i_{masw} = 2.7341 \times 10^5$ J/kg dry air (A.15b)

K.3 Specific heat of the water (T_{wi})

$c_{pw} = 4.1788 \times 10^3$ J/kg (A.17)

K.4 Lewis factor

$$Le_f = 0.865^{\frac{2}{3}} \left[\frac{\left(\frac{w_{sw} + 0.622}{w + 0.622} \right) - 1}{ln\left(\frac{w_{sw} + 0.622}{w + 0.622} \right)} \right] \quad (5.5)$$

$= 0.9564$

K.5 Temperature integration to next vertical grid point

$i_v = 2.5481 \times 10^6$ J/kg

Guess: $h_d a_{fi}/G_w = 0.1078$

$$\frac{\partial T_w}{\partial z} = \frac{1}{c_{pw}} \frac{G_a}{G_w} \frac{h_d a_{fi}}{G_a} \left[\begin{matrix} (w_{sw} - w) c_{pw} T_w - (i_{masw} - i_{ma}) - \\ (Le_f - 1)[i_{masw} - i_{ma} - (w_{sw} - w) i_v] \end{matrix} \right] \quad (5.1)$$

$= -4.9193$ K/m

$$T_{w,1} = T_{w,0} + \frac{\partial T_w}{\partial z} \Delta s = 322.9508 \text{ K} \quad (K.1)$$

K.6 Evaporation loss to next vertical grid point

$$\frac{\partial G_w}{\partial z} = -G_a \frac{h_d a_{fi}}{G_a} (w_{sw} - w) \quad (5.2)$$

$= -0.0105 \text{kg/m}^3\text{s}$

$$G_{w,1} = G_{w,0} + \frac{\partial G_w}{\partial z} \Delta s = 1.3999 \text{ kg/m}^2\text{s} \quad (K.2)$$

K.7 Humidity at next horizontal grid point

$$\frac{\partial w}{\partial x} = \frac{h_d a_{fi}}{G_a} (w_{sw} - w) \quad (5.4)$$

$= 0.0086$kg /m(kg dry air)

$$w_1 = w_0 + \frac{\partial w}{\partial x} \Delta s = 0.0165 \text{ kg/kg dry air} \quad (K.3)$$

K.8 Enthalpy of air at next horizontal grid point

$$\frac{\partial i_{ma}}{\partial x} = \frac{h_d a_{fi}}{G_a} \left[i_{masw} - i_{ma} + (Le_f - 1)\{i_{masw} - i_{ma} - i_v (w_{sw} - w)\} \right] \quad (5.3)$$

$$= 5.2059 \times 10^4 \text{ J/m(kg dry air)}$$

$$i_{ma,1} = i_{ma,0} + \frac{\partial i_{ma}}{\partial x}\Delta s = 6.7213 \times 10^4 \text{ J/ kg dry air} \quad \text{(K.4)}$$

After the solution converged, the Merkel number at every grid point is determined from the following relation:

$$Me(i,j) = G_a \frac{h_d a_{rz} H_{rz}}{G_{w(i,j)}} \quad (5.6)$$

The Merkel number for the system is simply the average of all the grid Merkel numbers, which is 0.2169.

L

CFD SOLVER MODELS AND INFORMATION

FLUENT
Version: 2d, dp, segregated, spe, ske (2d, double precision, segregated, species, standard k-epsilon)

Release: 6.2.16

Models

Model	Settings
Space	2D
Time	Steady
Viscous	Standard k-epsilon turbulence model
Wall Treatment	Standard Wall Functions
Heat Transfer	Enabled
Solidification and Melting	Disabled
Radiation	None
Species Transport	Non-Reacting (3 species)
Coupled Dispersed Phase	Enabled
Pollutants	Disabled
Soot	Disabled

Discretization Scheme

Variable	Scheme
Pressure	Standard
Momentum	Second Order Upwind
Turbulence Kinetic Energy	Second Order Upwind
Turbulence Dissipation Rate	Second Order Upwind
h2o	Second Order Upwind
o2	Second Order Upwind
Energy	Second Order Upwind

Material Properties

Material: water-liquid (droplet-particle)

Property	Units	Method	Value(s)
Density	kg/m^3	constant	998.20001
Cp (Specific Heat)	j/kg-k	constant	4178
Thermal Conductivity	w/m-k	constant	0.64486998
Latent Heat	j/kg	constant	2373000
Vaporization Temperature	k	polynomial	0 1
Boiling Point	k	constant	373
Volatile Component Fraction	%	constant	100
Binary Diffusivity	m^2/s	constant	2.1255941e-05
Saturation Vapor Pressure	pascal	polynomial	8132743 -110737.5 +568.4798 -1.305403 + 0.00113268
Heat of Pyrolysis	j/kg	constant	0

Material: mixture-template (mixture)

Property	Units	Method	Value(s)
Mixture Species	names	(h2o o2 n2)	
Density	kg/m3	incompressible-ideal-gas	#f
Cp (Specific Heat)	j/kg-k	mixing-law	#f
Thermal Conductivity	w/m-k	constant	0.02593
Viscosity	kg/m-s	constant	1.82e-05
Mass Diffusivity	m^2/s	constant-dilute-appx	(1.9985e-05)
Thermal Expansion Coefficient	1/k	constant	0

Material: air (fluid)

Property	Units	Method	Value(s)
Density	kg/m^3	constant	1.225
Cp (Specific Heat)	j/kg-k	constant	1006.43
Thermal Conductivity	w/m-k	constant	0.0242
Viscosity	kg/m-s	constant	1.7894001e-05
Molecular Weight	kg/kgmol	constant	28.966
L-J Characteristic Length	angstrom	constant	3.711
L-J Energy Parameter	k	constant	78.6
Thermal Expansion Coefficient	1/k	constant	0
Degrees of Freedom		constant	0
Speed of Sound	m/s	none	#f